


2012

Raman spectroscopy for characterizing and determining the pozzolanic reactivity of fly ashes

Nishant Garg
Iowa State University

Follow this and additional works at: <https://lib.dr.iastate.edu/etd>

 Part of the [Civil Engineering Commons](#), and the [Mechanics of Materials Commons](#)

Recommended Citation

Garg, Nishant, "Raman spectroscopy for characterizing and determining the pozzolanic reactivity of fly ashes" (2012). *Graduate Theses and Dissertations*. 12582.
<https://lib.dr.iastate.edu/etd/12582>

This Thesis is brought to you for free and open access by the Iowa State University Capstones, Theses and Dissertations at Iowa State University Digital Repository. It has been accepted for inclusion in Graduate Theses and Dissertations by an authorized administrator of Iowa State University Digital Repository. For more information, please contact digirep@iastate.edu.

**Raman spectroscopy for characterizing and determining the pozzolanic reactivity of fly
ashes**

by

Nishant Garg

A thesis submitted to the graduate faculty
in partial fulfillment of the requirement for the degree of
MASTER OF SCIENCE

Major: Civil Engineering (Civil Engineering Materials)

Program of Study Committee:
Kejin Wang, Major Advisor
Steve W. Martin
R. Christopher Williams

Iowa State University

Ames, Iowa

2012

Copyright © Nishant Garg, 2012. All rights reserved

Table of Contents

List of Tables	v
List of Figures	vi
Acknowledgements	x
Abstract	xii
CHAPTER 1: INTRODUCTION	1
1.1 Organization of Thesis	1
1.2 Problem Statement: “Why characterize fly ashes?”	2
1.2.1 Effective Utilization of a Waste Material	2
1.2.2 Need for Sustainable Cements	6
1.3 Characteristics of a Fly Ash	9
1.3.1 What is a fly ash?	9
1.3.2 Origin	10
1.3.3 Mineralogical Composition	11
1.3.4 Chemical Composition	12
1.3.5 Granulometry and Specific Surface	12
1.3.6 Pozzolanicity	13
1.3.7 Existing Methodology for Obtaining Pozzolanic Reactivity of a Fly Ash	13
1.4 Hydration Chemistry	15
1.4.1 Ordinary Portland Cement	15
1.4.2 Cements blended with fly ash	18
1.5 Introduction to Raman Spectroscopy	20
1.5.1 What is Raman Spectroscopy?	20
1.5.2 Principle	20
1.5.3 Theory – Classical Mathematical Treatment	23
1.5.4 Selection Rules for a Molecule	24
1.5.5 Vibrational Modes	26
1.5.6 Instrumentation	27
1.6 Scope of This Research	29

CHAPTER 2: LITERATURE REVIEW	31
2.1 Major Anhydrous Cementitious Minerals	31
2.1.1 Calcium Silicates (Alite & Belite)	32
2.1.2 Calcium Aluminates (Aluminate & Ferrite)	38
2.2 Major Hydrous Cementitious Materials.....	45
2.2.1 C-S-H	45
2.2.2 Portlandite	50
2.2.3 Calcium Aluminate Hydrates (C-A-H)	52
2.3 Others	52
2.3.1 Sulfates	53
2.3.2 Carbonates	61
2.3.3 Fly Ashes	67
2.4 Why use Raman spectroscopy?	70
2.4.1 Advantages	71
2.4.2 Limitations	72
CHAPTER 3: EXPERIMENTAL PROGRAM.....	74
3.1 Introduction to Materials (Cementitious Binders)	74
3.2 Supplementary Experiments on Fly Ashes	75
3.2.1 Chemical and Physical Properties.....	75
3.2.2 Calorimetry and Compressive Strength	76
3.3 Establishment of Raman Testing Configuration and Parameters	76
3.3.1 Possible Variations in Instrument Configuration.....	77
3.3.2. Possible Variations in Sample Preparation	77
3.3.3. Methodology of Data Collection	77
3.3.4. Analysis Techniques	78
3.5. Dry Analysis (1 OPC & 3 FA's).....	78
3.5.2. Bulk levels scans with 5x (200-1200 cm^{-1}) (25 locations)	78
3.6. Wet Analysis (5 pastes) (0-90 days)	78
3.6.1. Qualitative Evaluation of Developing Hydration Products (200-1200 cm^{-1}) (9 locations)	79

3.6.2. Evolution of Sulfates at Low Range Wavenumbers (950-1050 cm^{-1}) (49 locations)	79
3.6.3. Evolution of Portlandite at High Range Wavenumbers (3600-3700 cm^{-1}) (49 locations)	79
CHAPTER 4: RESULTS, ANALYSIS, AND DISCUSSION	80
4.1. Supplementary Experiments on Fly Ashes	80
4.2 Establishment of Raman Testing Configuration and Parameters	83
4.2.1 Possible Variations in Instrument Configuration.....	84
4.2.2. Possible Variations in Sample Preparation & Storage.....	89
4.2.3. Methodology of Data Collection	94
4.2.4. Analysis Techniques	99
4.2.5 Plotting Methods (Conversion of Data to Images)	106
4.3 Dry analysis	108
4.3.1 Ordinary Portland Cement	108
4.3.2 Fly Ashes	111
4.4 Wet Analysis	118
4.4.1 All Hydration Products	118
4.4.2 Evolution of sulfates	124
4.4.2 Evolution of hydroxides.....	132
CHAPTER 5: CONCLUSIONS, RECOMMENDATIONS AND FUTURE WORK	141
5.1 Conclusions.....	141
5.2 Recommendations.....	142
5.3 Future work.....	144
5.4 Final words.....	144
References.....	146

List of Tables

Table 1: Abbreviations used in cement science	15
Table 2: Composition of Ordinary Portland Cement	16
Table 3: Common hydration products in OPC paste	17
Table 4: Raman shifts for Alite	33
Table 5: Raman shifts for belite	36
Table 6: Raman shifts for C_3A	39
Table 7: Raman shifts for C_4AF	41
Table 8: Raman shifts for C-S-H gel	46
Table 9: Raman shifts for Portlandite	51
Table 10: Raman shifts for C-A-H phases	52
Table 11: Raman shifts for sulfates	56
Table 12: Raman shifts for carbonates	63
Table 13: Raman shifts for fly ashes	68
Table 14: Sources of binders	74
Table 15: Chemical Composition of Binders	74
Table 16: Mix proportions of mortars	76
Table 17: Pastes for Raman wet analysis	78

List of Figures

Figure 1: Statistical production and usage of coal combustion products. Adapted from [1]....	3
Figure 2: Latest available CCP production and use survey report from ACAA.	3
Figure 3: Coal Statistics from World Coal Institute [2].....	4
Figure 4: a) Coal Reserve Distribution in U.S. b) Comparison of Coal Consumption and Generation [3]	5
Figure 5: Cement production by various nations. [4]	7
Figure 6: Production and Price of Materials. Adapted from [5]	8
Figure 7: A typical fly ash as seen from SEM. Adapted from [9]	10
Figure 8: Typical Class C and Class F Ash [9].....	11
Figure 9: Heat of hydration curve for a normal cement. Adapted from [27].....	16
Figure 10: Pozzolanic reaction of fly ashes [29]	19
Figure 11: Principle of Raman spectroscopy. Courtesy: Rensselaer Polytechnic Institute	20
Figure 12: a) Energy level diagrams for Raman scattering b) Raman spectrum. Adapted from [30].....	22
Figure 13: Interaction of a Molecule with a Laser [31]	22
Figure 14: The volume of the polarizability ellipsoid is inversely proportional to α_i . [32]....	25
Figure 15: Polarizability ellipsoids for the carbon dioxide molecule [32]	27
Figure 16: Schematics of the Raman Spectrometer. Adapted from Renishaw User Manual.	28
Figure 17: A Picture of the Raman Instrument	29
Figure 18: Raman spectra for Pure Calcium Silicates (* indicates satellite bands) [44]	35
Figure 19: Typical Raman spectrum for C_3A [44].....	38
Figure 20: Typical Raman spectrum for C_4AF [44]	40
Figure 21: Raman spectra obtained from an OPC clinker nodule using 633 nm and 785 nm [43]	42
Figure 22: Raman spectra of the principal phases in anhydrous clinker [43]	44
Figure 23: Raman spectra of C3S pastes plus those of crystalline $11A^\circ$ and $14A^\circ$ tobermorite and jaffeite. [59].....	48
Figure 24: Raman spectra of C-S-H(I) synthesized with $Ca/Si = 1.50$ [50]	49
Figure 25: Evolution of Portlandite	50
Figure 26: Raman shifts for hydrated sulfates [64] (a) & (b) show the comparison of AFt and AFm at lower and higher wavenumber regions respectively, (c) shows the fingerprint spectrum for pure ettringite crystal, (d) shows comparison between the sulfate stretching modes of thenardite, gypsum, and ettringite.	54
Figure 27: Damaging effect of CO_2 on C_3A [63]	59
Figure 28: Disappearance of Gypsum and formation of Ettringite in C_3A paste [63].....	60
Figure 29: Raman chemical imaging distinguishing thaumasite (yellow) to ettringite (orange) [68]	61

Figure 30: Calcite (C), vaterite (V) and aragonite (Ar) [44].....	62
Figure 31: Effect of Carbonation on Ettringite and C-S-H (growth of peak ~1080) [36]	64
Figure 32: ν_1 carbonate bands of phases observed on aged cement samples [43]	66
Figure 33: Analysis of a Quartz grain a) Microscopic image of particle analyzed	
b) Raman Spectra	70
Figure 34: Based on Thomas Reuters Web of Knowledge database [79]	73
Figure 35: XRD of FA1	80
Figure 36: XRD of FA2	81
Figure 37: XRD of FA3	81
Figure 38: Variation in presence of Calcium in OPC and Fly Ashes	82
Figure 39: Calorimetric data of mortars.....	83
Figure 40: Compressive strength data of mortars	83
Figure 41: Typical setup of sample stored under the Raman microprobe	84
Figure 42: Effect of laser power on S/N	85
Figure 43: Effect of laser on sample surface as seen by the microscope on a 1 hour old OPC paste.	86
Figure 44: The non-destructive nature of the 488 nm laser on cementitious samples.....	86
Figure 45: Effect of Magnification on the microscopic images of hydrated OPC samples ...	87
Figure 46: Effect of magnification/laser spot on S/N (L means the location of the hydrated OPC paste)	88
Figure 47: Sample preparation.....	90
Figure 48: Sample storage in sealed sample cups.....	90
Figure 49: Upright sample storage results in condensation of water bubbles on sealing plastic film	91
Figure 50: Sample sealing involving pasting a thin film on the surface of the paste	91
Figure 51: Effect of imposing thin film on surface. The marked circle shows the additional unexpected peaks. The optical image on right shows the various locations measured on the sample.....	92
Figure 52: Raman spectra of the thin film alone.....	93
Figure 53: Effect of air exposure on fresh pastes	93
Figure 54: Raman spectra of hydration of 100% Raman spectra.	94
Figure 55: Carbonation attack on fly ash-cement pastes	96
Figure 56: Wire setup for 9 point mapping.....	97
Figure 57: Wire setup for 49 point mapping.....	98
Figure 58: A sample screenshot of Wire performing mapping analysis.....	99
Figure 59: Average reproducibility of selected hydrating pastes (exp = exposure)	100
Figure 60: Distribution of CH intensities at different locations (data set 1-49 = L1-L49)...	101
Figure 61: Application of the smoothening function.....	102
Figure 62: Normalization of 0.2h old hydrated OPC.....	103

Figure 63: After normalizing at each age, the change in average spectra of 49 spectra.....	104
Figure 64: Effect of Normalization followed by baseline subtraction.....	105
Figure 65: Presentation of evolution of sulfates data.....	106
Figure 66: Presentation of evolution of hydroxides data.....	107
Figure 67: Raman spectra of synthetic clinker phases.....	108
Figure 68: Raman spectrum for ordinary Portland Cement (Average of 25 spectra).....	110
Figure 69: Raman spectrum for FA1 (Average of 25 spectra).....	112
Figure 70: Raman spectrum for FA2 (Average of 25 spectra).....	113
Figure 71: Raman spectrum for FA3 (Average of 25 spectra).....	114
Figure 72: Comparison of three fly ashes based on their optical images and spectra.	115
Figure 73: Comparison of different magnification levels/spot size on Raman spectrum of FA1	117
Figure 74: Raman spectra following the hydration process of 50%SiO ₂ +50%OPC.....	120
Figure 75: Raman spectra following the hydration process of 100%OPC	121
Figure 76: Raman spectra following the hydration process of 50%FA1+50%OPC	122
Figure 77: Raman spectra following the hydration process of 50%FA2+50%OPC	123
Figure 78: Raman spectra following the hydration process of 50%FA3+50%OPC	124
Figure 79: Crystalline and pure sulfates	125
Figure 80: Evolution of sulfates in 100%OPC paste. AFt = Ettringite; G = Gypsum; A = Anhydrite	126
Figure 81: Evolution of sulfates in 50%FA+50%OPC pastes. AFt = Ettringite; G = Gypsum; A = Anhydrite; AFm = Monosulfoaluminate	129
Figure 82: Images representing the evolution of sulfates in 50%FA+50%OPC pastes.	131
Figure 83: Calibration of Intensity with CH concentration	133
Figure 84: Evolution of hydroxides in 100%OPC paste.....	134
Figure 85: Mapping the distribution of CH in 100% OPC paste.....	135
Figure 86: Evolution of hydroxides in 50%FA+50%OPC pastes.	137
Figure 87: Mapping the distribution of CH in 50%FA+50%OPC pastes.....	138

“Intellectual beauty is, indeed, the highest kind of beauty.”

– C.V. Raman (1888-1970)

Acknowledgements

This work would have been impossible without the financial support of my advisor, Kejin Wang, and I am very thankful to her for that. But more importantly, I cherish most of all her experienced advice and guidance which often helped me avoid stray paths and allowed me to stay focused on the task at hand. Our long, extended meetings packed with discussions, debates and at times, arguments, has fostered a better researcher in me and equipped me with the ability to solve research problems. This learning experience under her supervision is priceless.

I owe my heartfelt thanks to my minor advisor, Steve Martin, who introduced me to Raman spectroscopy through his life changing course in the materials science department. His encouragement and interest in my research helped me move forth with confidence in the methods I pursued. I regarded Gilson Lomboy as my unofficial advisor for the past two years of Masters, while not specifically helping on Raman spectroscopy, he advised me greatly on all things possible ranging from self-consolidating concretes to guidance on professional and personal goals of my life. Additional thanks for due to In-Seok Seo and Randi Christensen who helped me to both access and understand the Raman instrument. I'm also grateful towards Chris Williams for serving on my committee and giving insightful comments on my POS meetings. The professors I came across at Iowa State will have an everlasting inspirational effect on my life, David White and Aaron Sadow were one of those professors.

Scott Schlorholtz has been there to give answers to every kind of research problem that I faced, and without him, I may not have reached this far. His work ethic and expertise has inspired me many a times when I was lost alone in doubt.

I'm grateful to Linda Shenk and Dometa Brothers for helping me grow as a person more resolute and sane, by often brightening up my day when I was sick of research. Additional thanks to the following people who made my last two years wonderful: Bob Steffes, Alekhya, Hasitha, Jinxin and everyone else in Room 136 of Town Engineering.

One person who has been my flatmate for past two years, often given me free food, free advice, free lessons, free money cannot be thanked enough. Without her abundant love,

support, parenting and care I would not have come to US and be what I am today. I owe this gratitude to my biggest source of inspiration, Shivani Garg, my sister. My parents' strong desire to see their son understand the importance of knowledge has now finally come true. Without their push and encouragement, I would have totally missed these important lessons of life.

Finally, Tennessee Valley Authority (TVA), USA is acknowledged for providing the fly ashes and financial support. The support from David Dwight Eisenhower Fellowship funds is also appreciated.

Abstract

The efficacy and potential of Raman spectroscopy in characterization of a commercial Ordinary Portland Cement (OPC) and three fly ashes (FA's), and their evolving hydration products were studied in this Master's thesis work. While there have been several studies focusing on the application of Raman spectroscopy to synthetic, pure samples, work on commercial cementitious systems is scarce. This work covers this gap by evaluating mixtures containing cements and fly ashes.

The study first involved determination followed by establishment of instrumental configuration and testing parameters optimum for studying cementitious materials both in the dry and wet form. It was found that by tweaking several parameters, collection methodologies and analysis techniques, improved, representative and reproducible data could be obtained. Mapping a representative area to determine the spatial distribution and concentration of sulfates and hydroxides on sample surfaces was found to be the most effective way to study these complex and heterogeneous systems.

The Raman dry analysis of OPC and three different FA's of varying calcium contents and reactivity was able to identify the major mineralogical phases in these binders and the results were in correlation with the X-ray diffraction data. The observed calcium and sulfate phases and their relative concentration also agreed well with the supplementary compositional data obtained from X-ray fluorescence and Atomic absorption spectrometry.

The wet analysis of pastes prepared with 100% OPC and 50%OPC+50%FA(1,2,3) followed the hydration process of the systems for 56 days (0, 0.2, 2, 4, 8, 12, 16, 20, 24, 48, 72 hours, 7, 14, 21, 28, and 56 days). Consistency of trends in the hydration mechanism of such pastes was only obtained when studies were focused on narrow wavenumber ranges: 950-1050 cm^{-1} for evolution of sulfates and 3600-3700 cm^{-1} for evolution of hydroxides. Gradual disappearance of Gypsum with a parallel formation of Ettringite was clearly visible in most mixes, while transition of AFt to AFm was not very obvious and needs further research. Evolution of hydroxides showed the gradual spatial growth of portlandite in the studied areas of the samples. The growth rate and concentration of portlandite in different fly ash-cement-water mixes was correlated to the reactivity of the given fly ashes. While a clear connection

was not established, several observations were made based on the interpretation of the obtained data. This lack of agreement between expected and observed results may be attributed to the heterogeneity of the studied materials, potential problems in sample preparations as well as limitations of the technique.

Overall, Raman was effectively applied to the study of commercial, cementitious systems – this work being one of the early attempts if not the first attempt to study multi-phase fly ash blended cement pastes. While Raman may not be able to completely characterize and analyze such systems as a standalone tool, it definitely has a great potential in serving as a supplementary tool for deeper understanding of cement chemistry and hydration mechanisms.

CHAPTER 1: INTRODUCTION

1.1 Organization of Thesis

This thesis is organized into five chapters. Chapter 1 introduces the problem statement pertaining to the characterization of fly ashes, followed by an introduction to fly ash as a supplementary cementitious material in the light of its physical and chemical composition. Lastly, a brief introduction to Raman spectroscopy as a technique, and information on corresponding instrumentation and software packages employed in this study is given.

Chapter 2 covers a literature review of past studies involving the use of Raman spectroscopy on various cementitious materials and fly ashes. It is divided into three sections based on the materials studied e.g. anhydrous, hydrous, and other materials relevant to cementitious binders.

Chapter 3 includes the experimental program adopted for conducting this study. It is divided into two sections. The first section gives brief information about the materials employed while the second section focuses on the methods employed. Section two enlists the methodology of both data collection and analysis while detailing all testing configurations adopted.

Chapter 4 has all the results, analysis, and discussion that emerged from the testing conducted in the past two years of the research conducted in the Master's program of the author. The results are analyzed and discussed while weighing if the initial set of objectives have been met or not.

Chapter 5 is the final chapter of this thesis and includes the conclusions, recommendations and possibilities for future work, in case the reader may wish to pursue similar research.

1.2 Problem Statement: “Why characterize fly ashes?”

Accurate and effective characterization of fly ashes has remained a major unsolved issue since the past couple of decades as their production has continued to increase over the span of years. This problem statement can be tackled in the following twofold manner:

1.2.1 Effective Utilization of a Waste Material

The American Coal Ash Association (ACCA) includes fly ash with bottom ash, boiler slag and similar emission materials under the term “coal combustion products” or “CCPs”.

According to the recent statistics, the United States produced 131 million tons of CCPs in 2007 alone [1]. Out of these, only 43 percent were used beneficially while about 75 million tons were disposed of in landfills and other similar disposal methods. Figure 1 shows the CCP tonnage production, beneficial use, and percent beneficial use.

It is evident that production has significantly increased in the past five decades and most likely this upward trend will continue as long as coal reserves last in the US as well as around the world. This prediction is supported by the recently released CCP production and survey report for the year of 2010. Figure 2 shows the complete survey form for 2010, showing a total CCP production of 130 short tons (millions), with current beneficial usage at 42.5%.

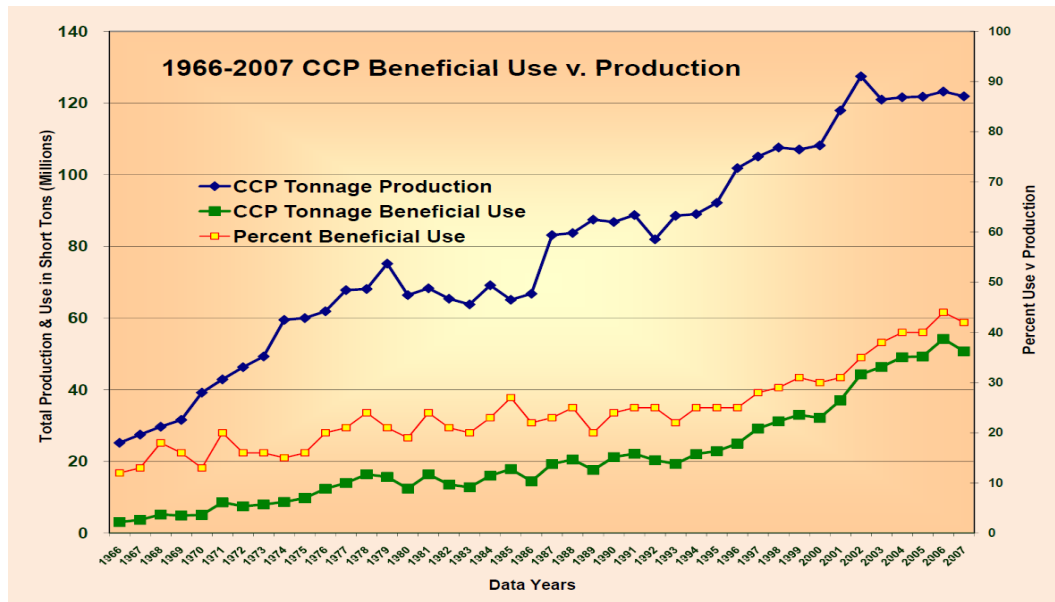


Figure 1: Statistical production and usage of coal combustion products. Adapted from [1]


<div>  <div> ACAA 15200 E. Girard Ave., Ste 3050 Aurora, CO 80014 </div> <div> Phone: 720-870-7897 Fax: 720-870-7889 Internet: www.ACAA-USA.org Email: info@aca-usa.org </div> </div>									
2010 Coal Combustion Product (CCP) Production & Use Survey Report									
Beneficial Utilization versus Production Totals (Short Tons)									
CCP Categories	Fly Ash**	Bottom Ash**	Boiler Slag*	FGD Gypsum**	FGD Material Wet Scrubbers*	FGD Material Dry Scrubbers*	FGD Other*	FBC Ash*	CCP Production / Utilization Totals
2010 Total CCPs Produced by Category	67,700,000	17,800,000	2,332,944	22,000,000	8,670,814	1,405,952	3,740	10,267,914	130,161,364
2010 Total CCPs Used by Category	25,723,217	7,541,732	1,418,996	10,713,138	624,223	584,112	0	8,732,008	55,337,426
1. Concrete/Concrete Products /Grout	11,016,097	615,332	0	21,045	0	16,847	0	0	11,669,321
2. Blended Cement/ Raw Feed for Clinker	2,045,797	949,183	3,000	1,135,211	0	0	0	0	4,133,191
3. Flowable Fill	135,321	52,414	0	0	0	13,998	0	0	201,733
4. Structural Fills/Embankments	4,675,992	3,124,549	78,647	454,430	424,581	358,019	0	0	9,116,218
5. Road Base/Sub-base	242,952	715,357	3,128	0	3,018	0	0	0	964,455
6. Soil Modification/Stabilization	785,552	162,065	0	0	0	19,189	0	0	966,806
7. Snow and Ice Control	0	549,520	41,194	0	0	0	0	0	590,714
8. Blasting Grit/Roofing Granules	86,484	19,914	1,257,571	0	0	0	0	0	1,363,969
9. Mining Applications	2,399,837	528,881	0	835,536	186,624	112,373	0	8,660,408	12,723,659
10. Gypsum Panel Products	109	0	0	7,661,527	0	0	0	0	7,661,636
11. Waste Stabilization/Solidification	3,258,825	41,233	0	0	0	39,283	0	71,600	3,410,941
12. Agriculture	22,220	4,674	0	481,827	0	0	0	0	508,721
13. Aggregate	6,726	555,031	27,155	0	0	0	0	0	588,912
14. Miscellaneous/Other	1,047,305	223,579	8,301	123,562	10,000	24,403	0	0	1,437,150
Summary Utilization to Production Rate									
CCP Categories	Fly Ash	Bottom Ash	Boiler Slag	FGD Gypsum	FGD Material Wet Scrubbers	FGD Material Dry Scrubbers	FGD Other	FBC Ash	CCP Utilization Total**
2010 Totals by CCP Type/Application	25,723,217	7,541,732	1,418,996	10,713,138	624,223	584,112	0	8,732,008	55,337,426
Category Use to Production Rate (%)***	37.90%	42.30%	60.80%	48.60%	7.10%	41.50%		85.00%	42.50%
2010 Cenospheres Sold (Pounds)	15,485,980								
<small> ACAA received survey data representing 231,379 MegaWatts Name Plate capacity of the total industry-wide approximate 327,983 capacity (i.e., 69.7%) or approximately 67% of the coal-fueled electric utility generation as reported by EIA. * These are actual tonnages reported by utilities responding and do not reflect estimates for utilities that did not respond this year. ** These numbers are derived from previous, current and applicable industry-wide available data, including Energy Information Administration (EIA) Reports 923 and 880 and other outside sources. *** Utilization estimates are based on actual tons reported and on extrapolated estimates for Fly ash, bottom ash, and FGD gypsum. </small>									
FINAL - 10/2011									

Figure 2: Latest available CCP production and use survey report from ACAA.

This clearly shows that the total beneficial usage has not changed a lot from the years 2007-2010 and serious efforts to push this usage percentage higher is the need of the hour.

According to the World Coal Institute, as of December 2011, 29.6% of primary energy needs and 42% of world's electricity is provided by combustion of mined coal [2]. Figure 3 shows the overall coal distribution among the various continents. It is interesting to note the recent upward surge in the coal production in Asia, led primarily by China, which is currently the largest producer of coal followed by the US and then India.

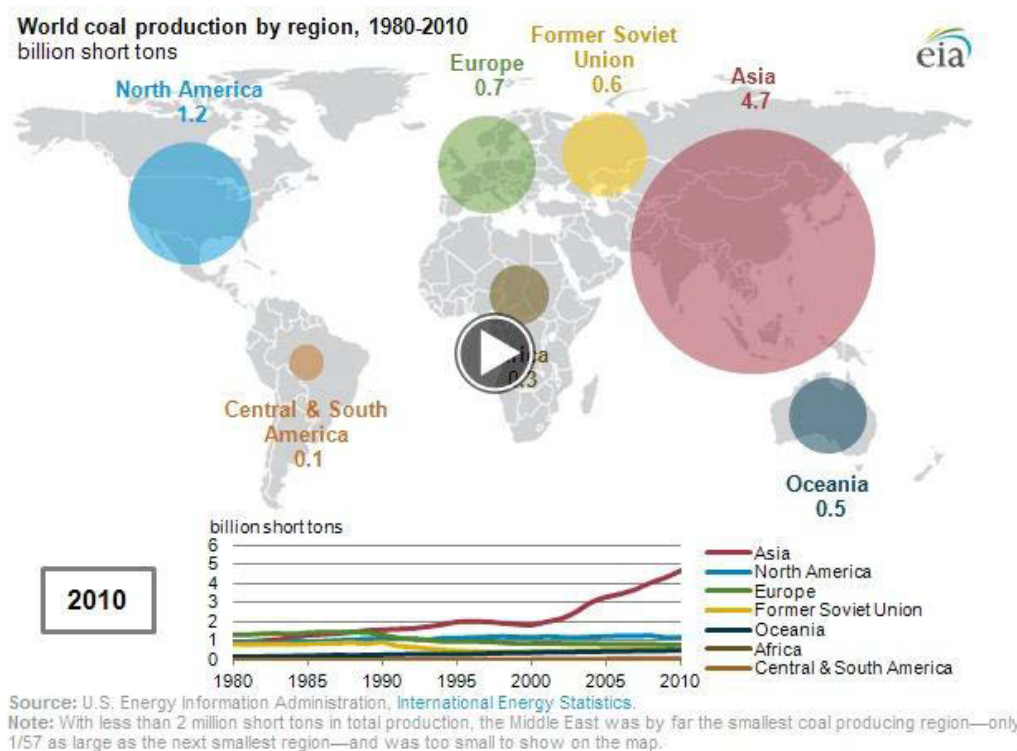


Figure 3: Coal Statistics from World Coal Institute [2]

In the US too, both coal consumption and production continues to increase steadily over past years. The electric power sector is the primary consumer which nearly consumes 93% of all coal produced in the US [3]. Figure 3 shows the distribution of coal reserves in North America, which is currently the nation with highest coal reserves in the world. Figure 4

shows the comparison of coal consumption to coal generation for the electric power sector which is indexed at 1.00 in 1990.

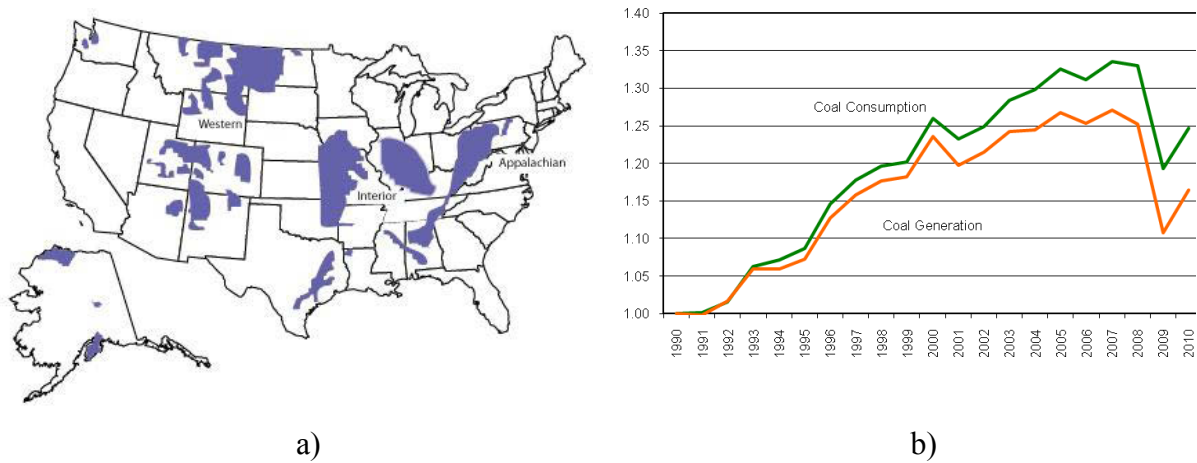


Figure 4: a) Coal Reserve Distribution in U.S. b) Comparison of Coal Consumption and Generation [3]

Shortly after the economic recession, coal production has returned to its upward trend in the U.S with its electric sector demand governed by fluctuating weather and temperature related factors.

Apart from the rising dependence on coal for energy needs, and increased production of CCPs as listed above, a recent man-made disaster has brought everyone's alarm towards fly ash. In December, 2008, the Tennessee Valley Authority (TVA) Kingston Fossil Plant coal fly ash slurry spill occurred in Roane County, Tennessee, USA. Approximately 1.1 billion US gallons of coal fly ash slurry was released in the Emory River which damaged nearby homes, the community and downstream waterways. It has been termed as the largest fly ash release in the history of United States.

Ninety percent of the ash was removed under the time critical phase and transported to a collection facility in Alabama and currently the non-time critical phase is conducting ecological evaluations of the surrounding sites. Several research projects were funded by the TVA regarding the reclamation of the site and this issue following the event. One of the research projects which focused on "Increasing use of fly ash in concrete" is the primary sponsor behind the research conducted in this thesis.

Hence, considering the above factors, all of which point towards increased production of fly ash in the coming future, it is imperative that better characterization of fly ash is required if it has to be effectively utilized for secondary purposes like soil stabilization, concrete production, etc.

1.2.2 Need for Sustainable Cements

The second reason which makes the characterization of fly ash an urgent problem is the growing need for sustainable cements. Production of Portland cement contributes to approximately 5% of man-made CO₂ emissions, and with cement being one of the most widely consumed materials in the world, sustainability in both production and application is crucial towards minimizing the harmful impact on the environment (see Figure 5 & Figure 6).

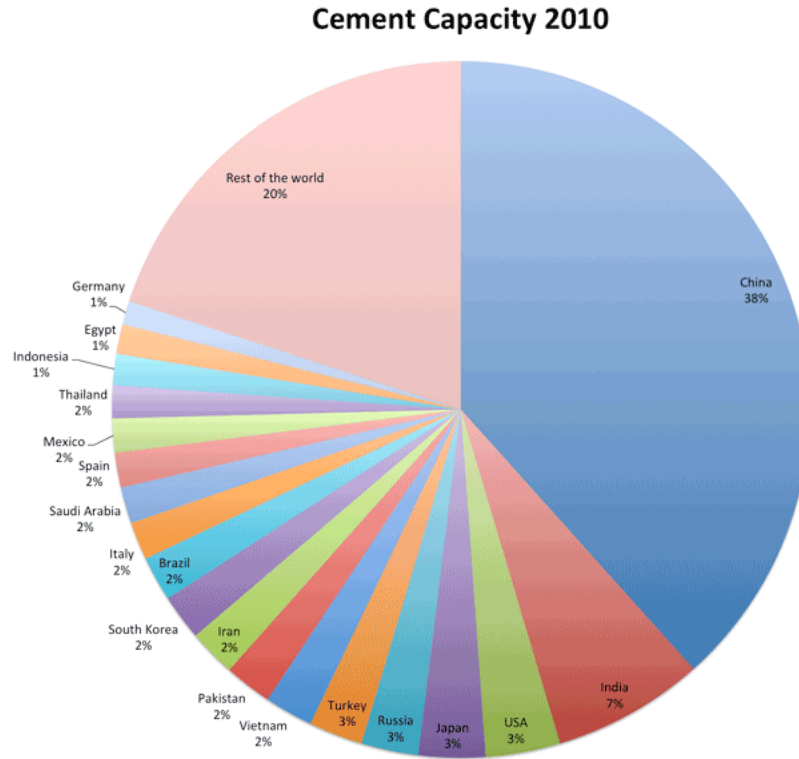


Figure 5: Cement production by various nations. [4]

In order to meet the growing energy and infrastructure needs of the global society, there is an increasing need for the employment of sustainable materials. Hence, the construction industry often relies on addition or replacement of ordinary Portland cement by supplementary cementitious materials (SCMs) to design a low-carbon concrete which is both economical and green. Such SCMs in the form of waste by-products from various industries (fly ash, blast furnace slag, silica fume) or naturally occurring fine materials (clays, limestone powder) offer a great potential in reduction of the overall clinker factor of the cement.

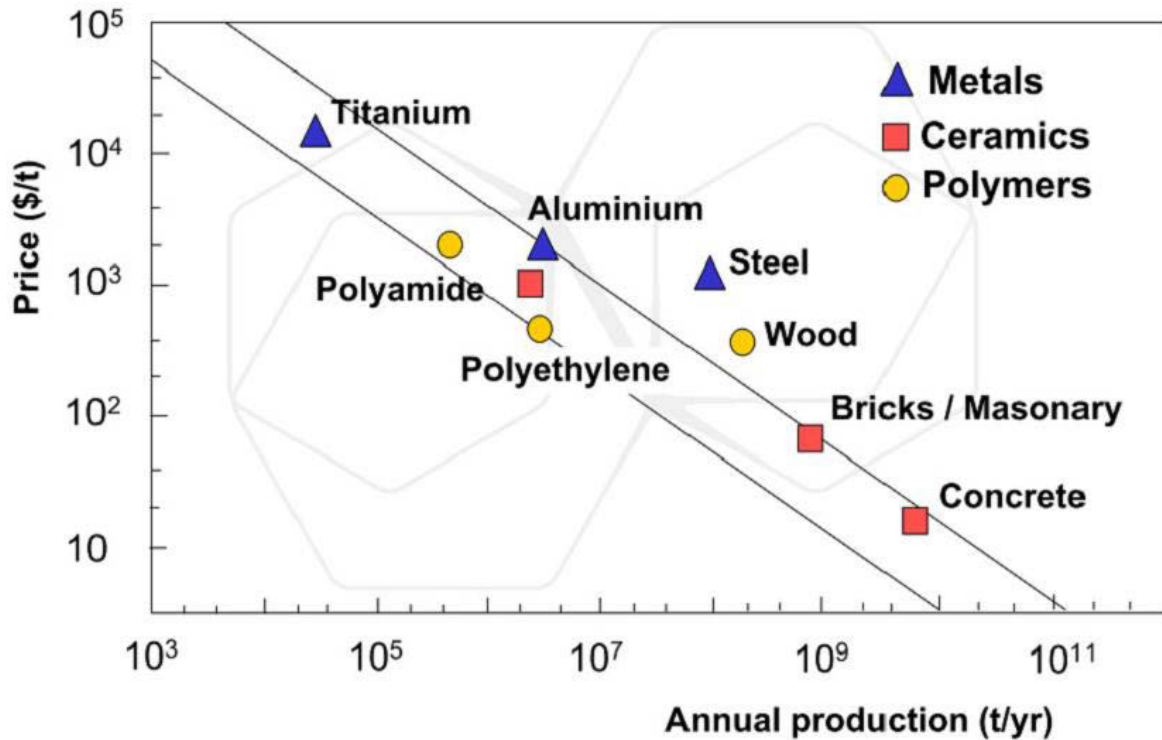


Figure 6: Production and Price of Materials. Adapted from [5]

Fly ashes has been used for cement replacement for many decades and their effectiveness to provide hydraulic as well as pozzolanic reaction in a cement system is well established [6]. However, most cement replacements by fly ash are limited to 20-25% based on the reactivity of the fly ash employed as well as the experience and intuition of the mix designer. Several efforts for high volume fly ash concretes have been made [7] but their field application is limited. Often ternary mixtures containing cement, fly ash, and another reactive SCM is blended to mitigate the effect of high volume fly ash [8] but the ternary system may get too complex to control for all desirable properties.

Hence, in order to obtain sustainable cements, it is crucial that they must be replaced by widely abundant SCMs like fly ash. And if the fly ash replacement level has to be increased in concrete, it is important that a given fly ash must be characterized for its reactivity accurately, so that its usage can be optimized in the cementitious system.

1.3 Characteristics of a Fly Ash

1.3.1 What is a fly ash?

Fly ash is fine, complex, residual material obtained from the combustion of pulverized coal. Its' heterogeneity varies at both macroscopic and microscopic scale.

A good understanding of the characteristics of a given fly ash is the key to optimize its' end usage for cement replacement in concrete

The role of fly ash as a SCM is explained in the following manner. The fly ash characteristics are sub-divided into origin, chemical composition, mineralogical composition, granulometry, pozzolanicity and others. The second section explains the changes that fly ash inclusion introduces in the hydration chemistry of cement.

The properties of a fly ash are explained on the basis of the following sub-divisions to give an overall picture of the fly ash both as an SCM and a fine, complex, glassy coal residue.

Figure 7 shows a typical fly ash micrograph, showing its spherical particle shape.

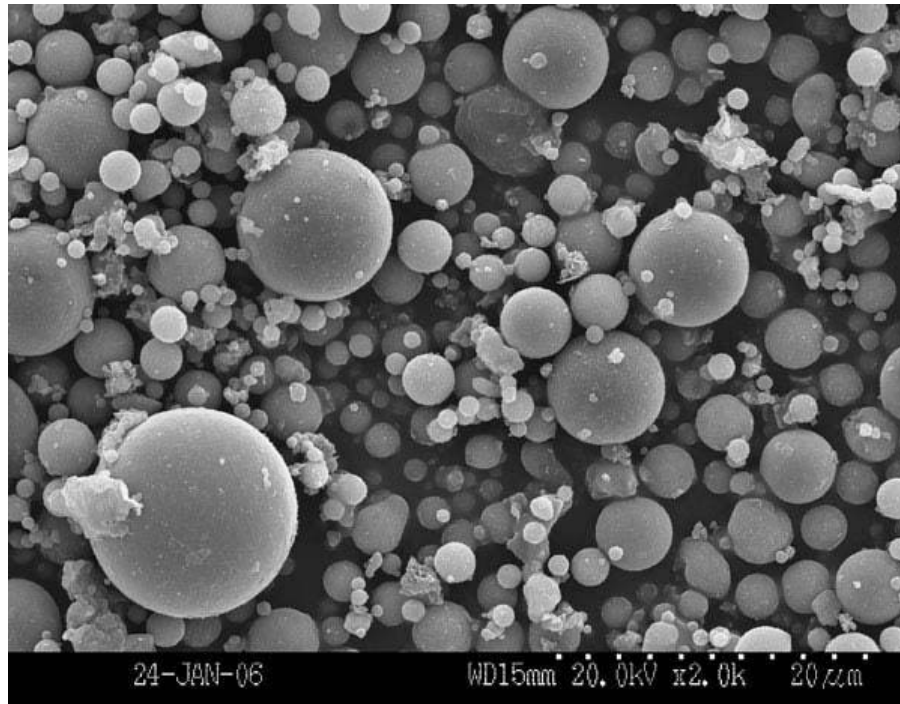


Figure 7: A typical fly ash as seen from SEM. Adapted from [9]

1.3.2 Origin

Since coal itself is an end product of a series of biological and physicochemical processes, the burnt residue is bound to contain a complex mixture of all possible parent minerals. Based on various factors like depth of burial, varying combinations of temperature and pressure, the coal's final state may contain a range of different compounds and thus can be sub-divided into various classes or groups like anthracite, peat, lignite, bituminous or sub-bituminous coals. Anthracite is known to have the highest calorific value while lignite has the lowest. Depending on the type of the coal burnt, a fly ash's calcium content may vary significantly. ASTM divides fly ashes on such a basis, and normally burning anthracite or bituminous coal results in a Class F fly ash while burning lignite or sub-bituminous coal results in Class C fly ash. The combustion process employed in the power station boilers is also a governing factor for the properties of the end product i.e. fly ash emitted. Figure 8 shows typical fly ashes based on this classification. Notice the color distinction (light vs. dark) that is usually present.



a) A Class C Fly Ash



b) A Class F Fly Ash

Figure 8: Typical Class C and Class F Ash [9]

1.3.3 Mineralogical Composition

Due to the rapid cooling of the waste CCPs fly ashes chiefly (50-90%) contain glassy phases with some crystalline phases. Unburnt coal is often present in the ashes depending upon the burning efficiency of the boiler at the power plant. A comprehensive review on the glasses in fly ash by Hemmings [10] was given long ago which is quite informative and applicable till date.

The crystalline phases have been mostly studied by X-ray diffraction, while other techniques like Infrared spectroscopy, gamma ray spectroscopy, electron microscopy have been employed as well. The major mineral phases found in fly ashes are Quartz, Mullite, Hematite, Magnetite, and free Calcium Oxide. Other than these, minerals like goethite, pyrite, calcite, anhydrite, and periclase can be found in trace quantities as well.

Quantification of fly ash glass phases has been done with QXRD, however due to the complexity and heterogeneity of fly ash particles at the micro-scopic scale the estimates are often not very accurate. Several supplementary techniques are required at a time to obtain an accurate picture of a given fly ash. Raman spectroscopy can serve as one of those complementary techniques to study fly ash.

1.3.4 Chemical Composition

SiO_2 , Al_2O_3 , and Fe_2O_3 are the primary oxides in most fly ashes with varying small amounts of CaO , MgO , MnO , TiO_2 , Na_2O , K_2O , SO_3 etc. ASTM C 618 classifies the fly ashes into Class F and Class C based on their total $\text{SiO}_2 + \text{Al}_2\text{O}_3 + \text{Fe}_2\text{O}_3$ content. Burning of fly ash at 1000°C results in a weight loss, which is primarily due to carbon and is termed as Loss on Ignition (LOI).

1.3.5 Granulometry and Specific Surface

ASTM C 311 recommends wet-sieving the fly ash sample with a No. 325 ($45\text{ }\mu\text{m}$) sieve following the ASTM C 430 method to obtain a representative idea of the particle size of a fly ash in case a complete sieving analysis is not performed. National standards of various countries around the world have different specifications written for the maximum residue that should be retained on the $45\text{ }\mu\text{m}$ to consider the fly ash as a suitable pozzolan in concrete. The particle size distribution of fly ashes varies from $0.2\text{ }\mu\text{m}$ to $200\text{ }\mu\text{m}$ depending upon the burning efficiency of the power plant boilers and origin of the coal. The shape of the particles depends upon the nature of the coal burnt as well as combustion conditions and temperature. Usually the particles are spherical in nature, which results due to melting of the mineral matter and its sudden cooling afterward. The spheres may be hollow (cenospheres) or contain a number of smaller spheres (plerospheres).

The Blaine method is usually employed to measure the specific surface or fineness of a fly ash and it varies from 250 to $550\text{ m}^2/\text{kg}$. The fineness also depends on the collection efficiency of electrostatic precipitators. Nitrogen adsorption BET is also used to measure the fineness of fly ashes, however the results between the two tests may not correlate very well due to the difference in their fundamental approaches.

1.3.6 Pozzolanicity

The pozzolanicity of a SCM is defined as its capacity to react with CaO or Ca(OH)_2 in the availability of water to form secondary products or masses. This secondary reaction in fly ash blended cement systems often starts at later ages (14 or 28 days later) but the onset and the progress actually depends on the reactivity of a given fly ash. A fine fly ash with reactive amorphous phases may begin its pozzolanic reaction earlier than a coarse fly ash with inert, crystalline phases. Higher reactivity leads to higher production of hydration products in a cement system leading to a denser and more impermeable matrix contributing towards higher mechanical strength with progression of age.

Accurate and complete characterization of a fly ash demands that for a given fly ash, all the properties listed above must be determined with caution, and only then its reactivity can be predicted. If the reactivity is not gauged accurately, fly ash continues to stay as a waste material, probably only serving as a filler. It is primarily due to this reason that establishing the reactivity of a fly ash is of utmost importance before it can be effectively replace higher proportions of cement and thus employed to obtain a sustainable concrete.

1.3.7 Existing Methodology for Obtaining Pozzolanic Reactivity of a Fly Ash

Fly Ash has been used as a replacement in cement for construction practices due to its pozzolanic properties and environmental benefits for a long time now [6, 11] . While Class C fly ash possess both cementitious and pozzolanic properties, Class F fly ash only exhibits the latter, as being non-hydraulic in nature it only reacts with the cement hydration products (Calcium Hydrate) resulting in formation of C-S-H (Calcium Silicate Hydrate) gel at a later age [12, 13] . The amount of fly ash to be replaced by weight in a cement system depends on this pozzolanic reactivity or efficiency of the fly ash under consideration.

ASTM C 311 [14] provides the strength activity index for this pozzolan which considers both the pozzolanic reaction and size of the fly ash as parameters affecting the compressive strength of concrete. Researchers have also linked this pozzolanic reactivity to the particle size contending that apart from the filling ability - the finer the fly ash, the more is its reactivity due to a larger surface area available for faster reaction with the hydration products [15-19]. It is a proven fact that both the chemical and physical properties of a fly ash affect its reactivity and not every fly ash is similar to another in this regard. Hence, gauging the reactivity or efficiency of a given fly ash is critical before it can be optimally used in cement construction.

The existing equation in ASTM C311 defines the activity of the fly ash merely by comparing the strength of a fly ash modified mortar with that of an OPC control mixture at a given age in days. Such an index provides a vague yet practical scope on the capability of a given fly ash considering the fact that each fly ash develops strength at its own rate (as shown in this study). Since the standard method by ASTM requires a minimum of 28 days to establish the reactivity of this pozzolan, several researchers have suggested quicker methods to determine the same [20-24]. It mostly involves measuring the amount of lime that combines with the pozzolan in a mixture with respect to time, and can also be done through various techniques but not limited to XRD, XRF, SEM, DTA/TGA, MIP etc [25, 26]. Also, it is crucial that all products evolved from the reaction of fly ash with cementitious hydration products be characterized and understood well before judgments about a fly ash can be made.

Most methods rely on following the growth and subsequent depletion of calcium hydroxide (Portlandite) to gauge the pozzolanic reactivity of a fly ash. In this study, a similar approach has been employed with Raman spectroscopy. Additionally, the evolution of sulfate type phases and other hydroxides were also studied as a function of time.

1.4 Hydration Chemistry

This section covers the chemical processes that occur on reaction of cementitious materials with water. It is divided in two sub-sections. The first one deals with the hydration chemistry of ordinary Portland cement (OPC) and the second one deals with the hydration chemistry of cements blended with fly ashes. The description following is very general and meant to provide an overview of the hydration process to the reader and is no way exhaustive because hydration kinetics, mechanisms, and products are all complex functions of heterogeneous materials and the surrounding environment.

1.4.1 Ordinary Portland Cement

Cement science has a set of unique notations which are used commonly among the researchers studying cement and cementitious materials. Table 1 shows the common abbreviations used.

Table 1: Abbreviations used in cement science

Chemical Formula	Abbreviated Symbol
CaO	C
Al ₂ O ₃	A
MgO	M
SO ₃	\bar{S}
SiO ₂	S
Fe ₂ O ₃	F
K ₂ O	K
H ₂ O	H
C	\bar{C}

OPC consists of four primary mineral phases, namely tricalcium silicate, dicalcium silicate, tricalcium aluminate, and tetracalcium aluminoferrite. Their distribution and abbreviations are shown collectively in Table 2.

Table 2: Composition of Ordinary Portland Cement

Mineral Phase	Chemical Compound	Abbreviated Form	Typical %
Tricalcium Silicate	Alite	C_3S	50-70%
Dicalcium Silicate	Belite	C_2S	15-30%
Tricalcium Aluminate	Aluminate	C_3A	5-10%
Tetracalcium Aluminoferrite	Ferrite	C_4AF	5-15%

Cement hydration is commonly referred to the process in which cement when comes in contact with water forms solid hydration products which set with the progression of time. However, the entire process is not as simple as stated and is broken down into several steps as shown in Figure 9.

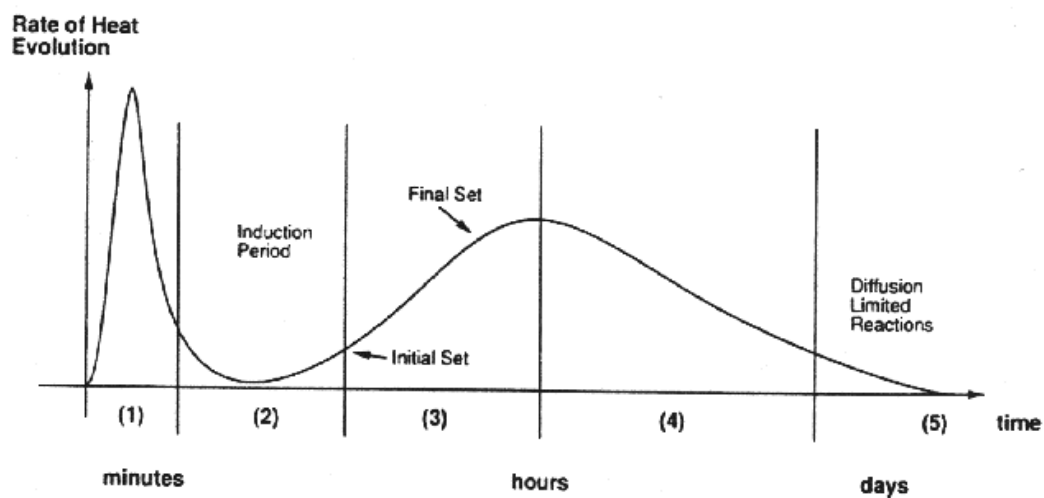


Figure 9: Heat of hydration curve for a normal cement. Adapted from [27]

The first stage known as dissociation or hydrolysis includes a rapid hydration with a large amount of heat release due to the exothermic dissolution of the clinker phases in water. The second period is called the induction period which is dormant in terms of reactions and several theories have been postulated explaining the reason for this dormancy in the reaction. One of the theories explain that this is due to the formation of an impermeable layer of initial hydration products on clinker grains which is breached slowly by the exchange of ions between pore solution and mineral phase. The third period is that of acceleration when cement begins to set and calcium silicates hydrate. The deceleration period starts once the final set has occurred and the cement begins to gain mechanical properties. The last state is diffusion limited and secondary reactions continue at slower pace. Table 3 shows the major hydration products formed during the chemical process.

Table 3: Common hydration products in OPC paste

Chemical Name	Chemical Formula (abbreviated)
Gypsum	$C\bar{S}H_2$
Calcium silicate hydrate, C-S-H	$C_{1.7}SH_4$
Calcium hydroxide	CH
Ettringite	$C_6A\bar{S}_3H_{32}$
Monosulfate	$C_4A\bar{S}H_{12}$
Hydrogarnet	C_3AH_6
Iron hydroxide	FH_3
Calcium hemicarboaluminate	$C_4A\bar{C}_{0.5}H_{12}$
Calcium monocarboaluminate	$C_4A\bar{C}_1H_{11}$

When calcium silicates react with water, an amorphous calcium silicate hydrate (C-S-H) is deposited on the surfaces of clinker minerals while calcium hydroxide (CH) nucleates in the form of crystals in the pore space. With time polymerization of C-S-H occurs while more and more CH is produced. Approximate silicate reactions are listed in the following equations:



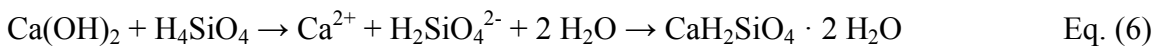
Tricalcium aluminate reacts the fastest in OPC and thus gypsum is added to the clinker to slow down its reaction. C_3A reacts with gypsum to form ettringite which grows as crystalline needles in the cement paste from as early as 10 minutes from the onset of the hydration reaction. As gypsum is consumed, ettringite may begin to decompose and form a monosulphate phase. Hydrogarnet results when gypsum is not present in the system. The ferrite phase is not dominantly present in OPC and its reaction with water is not well understood in a complex system like cement. However, it is assumed that it may lead to the production of extra CH and possible FH_3 . The following equations show the approximate reactions for the aluminate phases.



For a detailed information on the hydration process of cement or cementitious materials, the reader is recommended to refer to the excellent book of Cement Chemistry by Taylor [28].

1.4.2 Cements blended with fly ash

When ordinary cements are blended with fly ashes or any such pozzolans there is a set of additional reactions that take place which are a function of the reactivity of the pozzolan in consideration. The silicates present in an ash react with the excess calcium hydroxide to form additional C-S-H. The aluminates and sulfates present can also result in alumina and sulfate ion inclusion in the C-S-H structure or may completely replace the silicate ion to form stratlingite ($C-A-\bar{S}-H$).



1.5 Introduction to Raman Spectroscopy

This section will give brief information on the technique and its principle, followed by relevant information on the instrumentation and computer programs employed in this study.

1.5.1 What is Raman Spectroscopy?

Raman spectroscopy is a spectroscopic technique which is used to study the vibrational and rotational modes of excited molecules of a material. It happens due to the inelastic scattering in the visible, near infrared or near ultraviolet range. The laser interacts with the molecular vibrations in the system which results in change in the energy of the scattered photons. This change or shift in energy is a characteristic function of the vibrational modes of a molecule and hence helps in characterizing the given compound. Figure 11 shows a basic schematic of

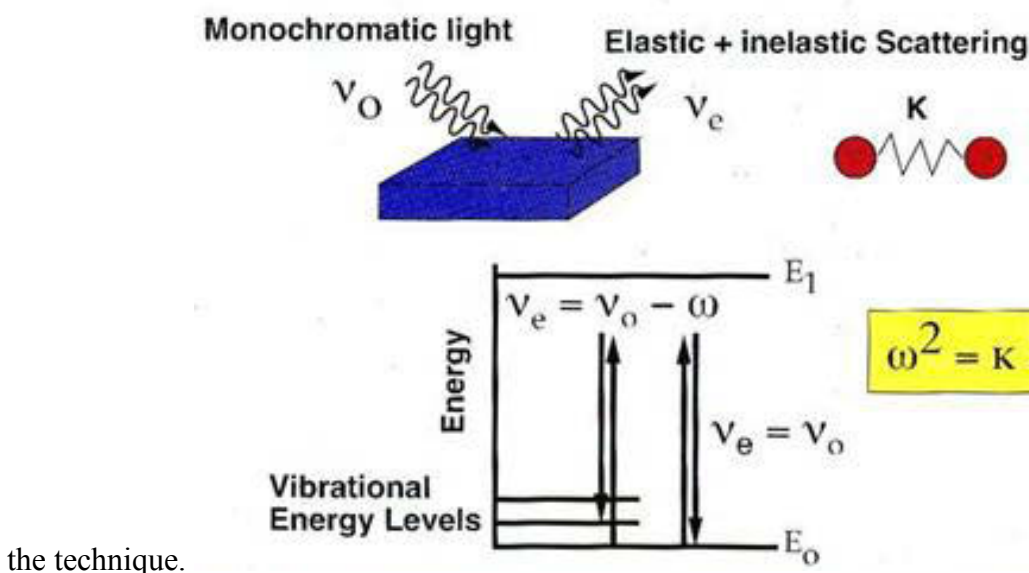


Figure 11: Principle of Raman spectroscopy. Courtesy: Rensselaer Polytechnic Institute

1.5.2 Principle

When a laser light impinges upon a molecule with an initial frequency, the molecules gets excited to a virtual energy state based upon the vibrational/rotational state of its bond

structure. Now, when this molecule relaxes, the photons it emits back either have a frequency greater than that of the original laser photon (Anti-stokes) or frequency lower than that of the original (Stokes). This difference in frequency is known as the Raman Shift (measured in wavenumbers cm^{-1}).

Figure 12 shows the excitation process of the molecule from the ground state to the virtual excited state which results in the stokes and anti-stokes scattering simultaneously. Figure 13 shows the interaction of a molecule with a laser. It must be noted that only 1 in 10^6 photons are inelastically scattered (Raman scattering) while most of them are elastically scattered (Rayleigh scattering). Brillouin scattering occurs due to the scattering of the sound waves and they are not discussed here. Debye and Mie, which are other elastic forms of scattering depending upon particle size of the scatterer are also not discussed here.

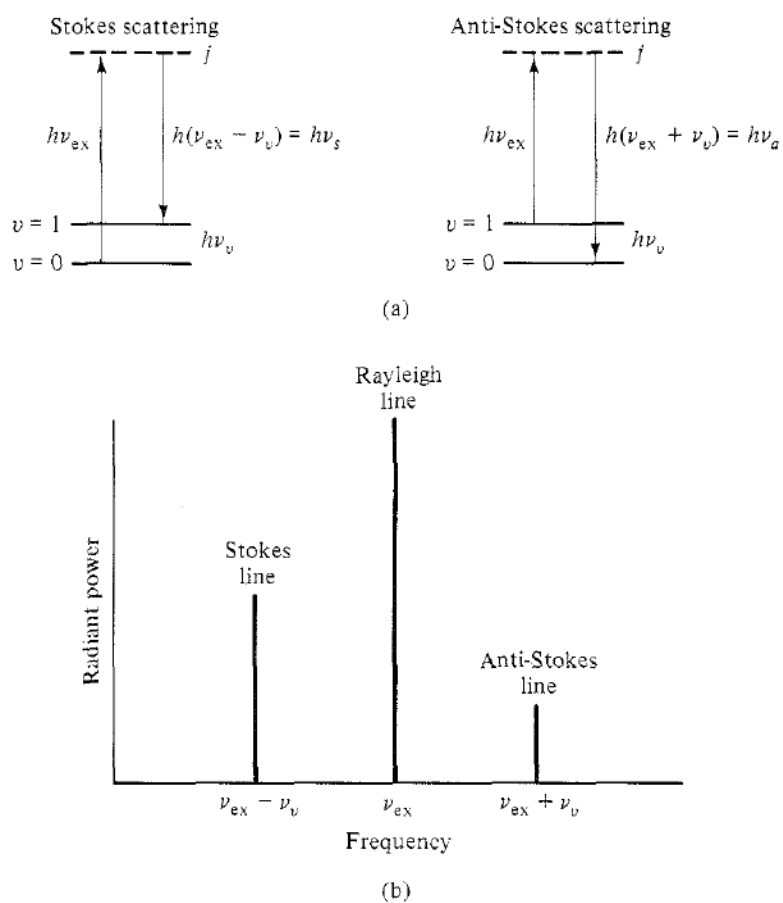


Figure 12: a) Energy level diagrams for Raman scattering b) Raman spectrum. Adapted from [30]

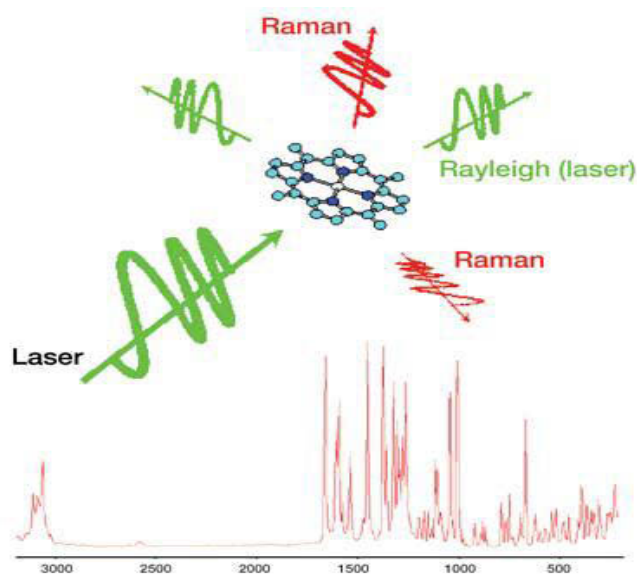


Figure 13: Interaction of a Molecule with a Laser [31]

1.5.3 Theory – Classical Mathematical Treatment

A molecular vibration is Raman active if it changes the polarizability of the molecule. Polarizability is defined as the change in the dipole moment with respect to a change in the electric field.

$$\mu = \alpha.E \quad \text{Eq. (8)}$$

where;

μ = Induced dipole moment of the molecule,

E = Electric field, and

α = Polarizability of the molecule (a tensor).

If the field is oscillating, the amplitude of the electric field (E) at any time (t) can be given as,

$$E = E_0 \cos(2\pi\nu_1 t) \quad \text{Eq. (9)}$$

where;

E_0 = Maximum amplitude of the electric field, and

ν_1 = Frequency of the electromagnetic wave.

Hence,

$$\mu = \alpha.E_0 \cos(2\pi\nu_1 t) \quad \text{Eq. (10)}$$

Consider a diatomic molecule with a natural vibration frequency (ν_0). The normal vibration vector Q can be expressed as a function of time as :

$$Q(t) = Q_0 \cos(2\pi\nu_0 t) \quad \text{Eq. (11)}$$

$$\alpha(r) = \alpha_0 + \left(\frac{\partial \alpha}{\partial Q} \right).Q + \text{higher order terms}$$

$$\alpha(t) = \alpha_o + \left(\frac{\partial \alpha}{\partial Q} \right) \cdot Q_o \cos(2\pi v_o t)$$

Therefore,

$$\mu(t) = \left[\alpha_o + \left(\frac{\partial \alpha}{\partial Q} \right) \cdot Q_o \cos(2\pi v_o t) \right] E_o \cos(2\pi v_1 t)$$

$$\mu(t) = \alpha_o E_o \cos(2\pi v_1 t) + \left(\frac{\partial \alpha}{\partial Q} \right) \cdot Q_o \cos(2\pi v_o t) E_o \cos(2\pi v_1 t)$$

$$\mu(t) = \alpha_o E_o \cos(2\pi v_1 t) + \frac{1}{2} Q_o \cdot E_o \left(\frac{\partial \alpha}{\partial Q} \right) \cdot [\cos(2\pi(v_1 - v_o)t) + \cos(2\pi(v_1 + v_o)t)] \quad \text{Eq. (12)}$$

Elastic component

Inelastic component

Rayleigh scattering

Stokes

Antistokes

1.5.4 Selection Rules for a Molecule

For a molecule to be Raman active, it must have anisotropic polarizability. The Polarizability ellipsoid can be defined by its angular dependence in the terms of α_x , α_y , α_z , where x, y, and z are the principal axis of polarizability of the molecule.

$$E = \frac{1}{4\pi\epsilon_o} \cdot \frac{q}{r^2}$$

$$\alpha = \left(\frac{\partial \mu}{\partial E} \right) = \frac{\text{charge} \cdot \text{distance}}{\frac{\text{charge}}{\text{distance}^2}} = \text{distance}^3 = \text{volume}$$

For completely anisotropic molecules, $\alpha_x \neq \alpha_y \neq \alpha_z$. The volume obtained above shows that the polarizability is denoted by the volume of an ellipsoid which will be defined more clearly in the following paragraph.

We know that, $\mu = \alpha \cdot E$

Hence, dividing it into directional components, we obtain:

$$\begin{matrix} \mu_x \\ \mu_y \\ \mu_z \end{matrix} = \begin{bmatrix} \alpha_{xx} & \alpha_{yx} & \alpha_{zx} \\ \alpha_{xy} & \alpha_{yy} & \alpha_{yz} \\ \alpha_{xz} & \alpha_{yz} & \alpha_{zz} \end{bmatrix} \cdot \begin{bmatrix} E_x \\ E_y \\ E_z \end{bmatrix}$$

The first matrix on the right is called the “polarizability tensor”. This tensor is symmetric in normal Raman scattering. According to the rules of quantum mechanics, a vibration is Raman-active is one of the components of the tensor changes during the vibration. When $1/\sqrt{\alpha_i}$ is plotted for a molecule from the center of gravity in all directions, a three-dimensional surface is obtained which is known as the polarizability ellipsoid. So in order to have a Raman spectrum, the polarizability ellipsoid should change in shape, size or orientation. Figure 14 shows graphic representation of a polarizability ellipsoid.

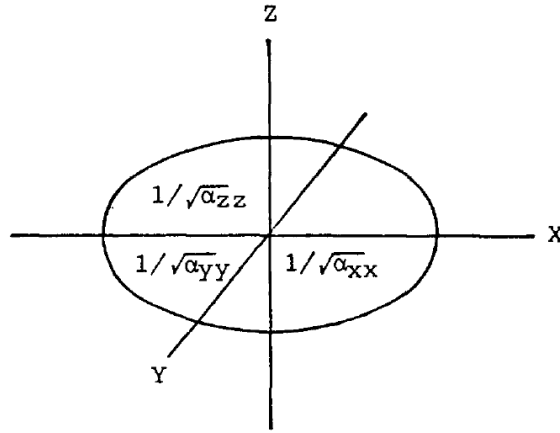


Figure 14: The volume of the polarizability ellipsoid is inversely proportional to $\sqrt{\alpha_i}$. [32]

1.5.5 Vibrational Modes

The random, complex motions of atoms in an excited molecules can compounded into a definite number of so-called normal modes, when analyzed by classical mechanics. In each of the normal modes, the atoms move with a characteristic normal frequency. The number of such modes can be calculated as follows.

Every atom has three degrees of freedom, and a molecule with N number of atoms will have $3N$ degrees of freedom. However, 6 out of these represent the rotational and translational motions around the Cartesian axis, reducing the vibrational modes to $3N-6$. For linear molecules this reduces to $3N-5$ as the rotation around the molecular axis is not accounted for.

In order to show the application of the selection rules discussed earlier, and to deduce the vibrational modes of a molecule, let's consider a CO_2 molecule. Since it is a linear molecule ($\text{O}=\text{C}=\text{O}$), it has four normal vibrational modes ($3N-5 = 3 \times 3 - 5 = 4$). The four vibrational modes are usually assigned as follows:

ν_1 = symmetric stretching of oxygen atoms around carbon,

ν_2 = in-plane bending,

ν_3 = asymmetric stretching of oxygen atoms around carbon, and

ν_4 = out-of-plane bending.

Figure 15 shows the stretching modes and the relevant polarizability ellipsoids alongside. Now, it is easy to see which modes will be Raman active and which modes will be Raman inactive. It is evident that only ν_1 (symmetric stretching mode) results in the change in the shape of the polarizability ellipsoid (comparing final states)

However, the method of analyzing the graphical change in the plotted ellipsoids turns out to be trivial when larger molecules are to be considered. Especially, when there are complex vibrational motions and multiple atoms involved. Then, determining whether a given mode is Raman active or not requires complex methods involving symmetry operations and group theory. Those methods are out of the scope of this thesis work and the reader is encouraged

to refer to excellent texts specializing in this field. F.A. Cotton's text on group theory can be the first place to start [33].

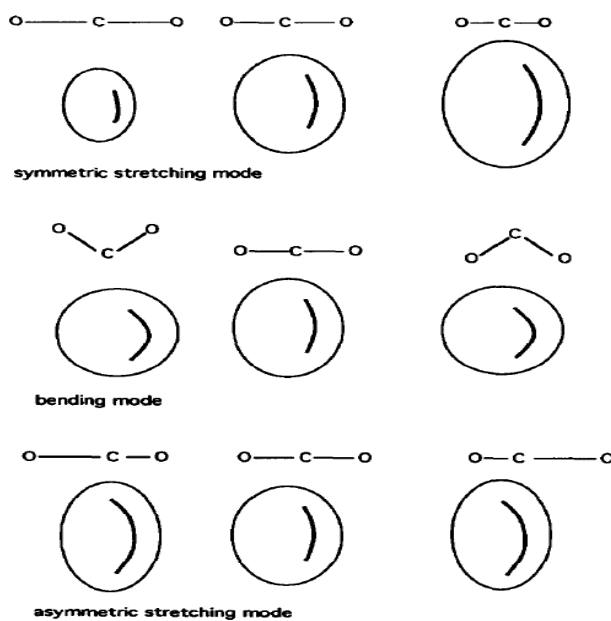
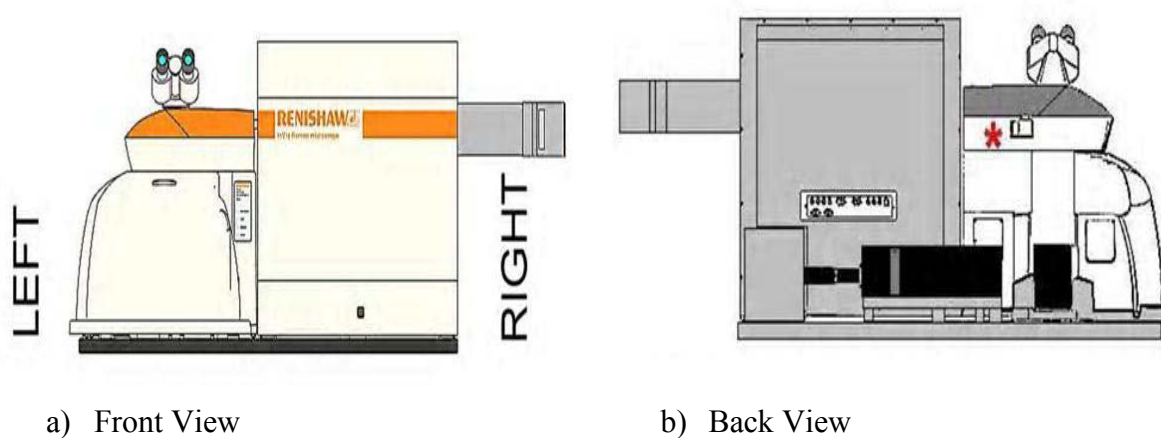


Figure 15: Polarizability ellipsoids for the carbon dioxide molecule [32]

1.5.6 Instrumentation

A Renishaw inVia Reflex spectrometer using a 488nm Ar laser was employed in this study.



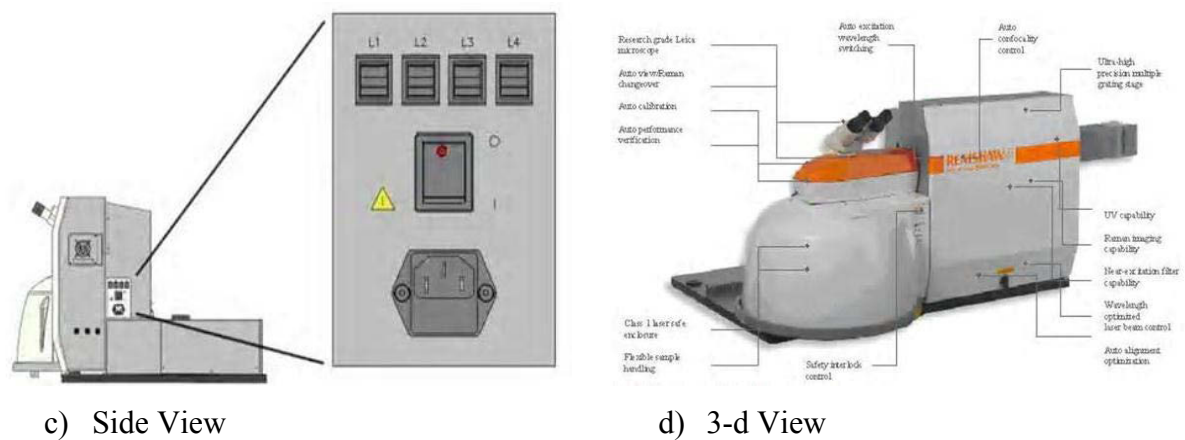


Figure 16: Schematics of the Raman Spectrometer. Adapted from Renishaw User Manual.

Figure 16 shows the schematics of the instrument and Figure 17 shows the picture of the instrument employed in this study.

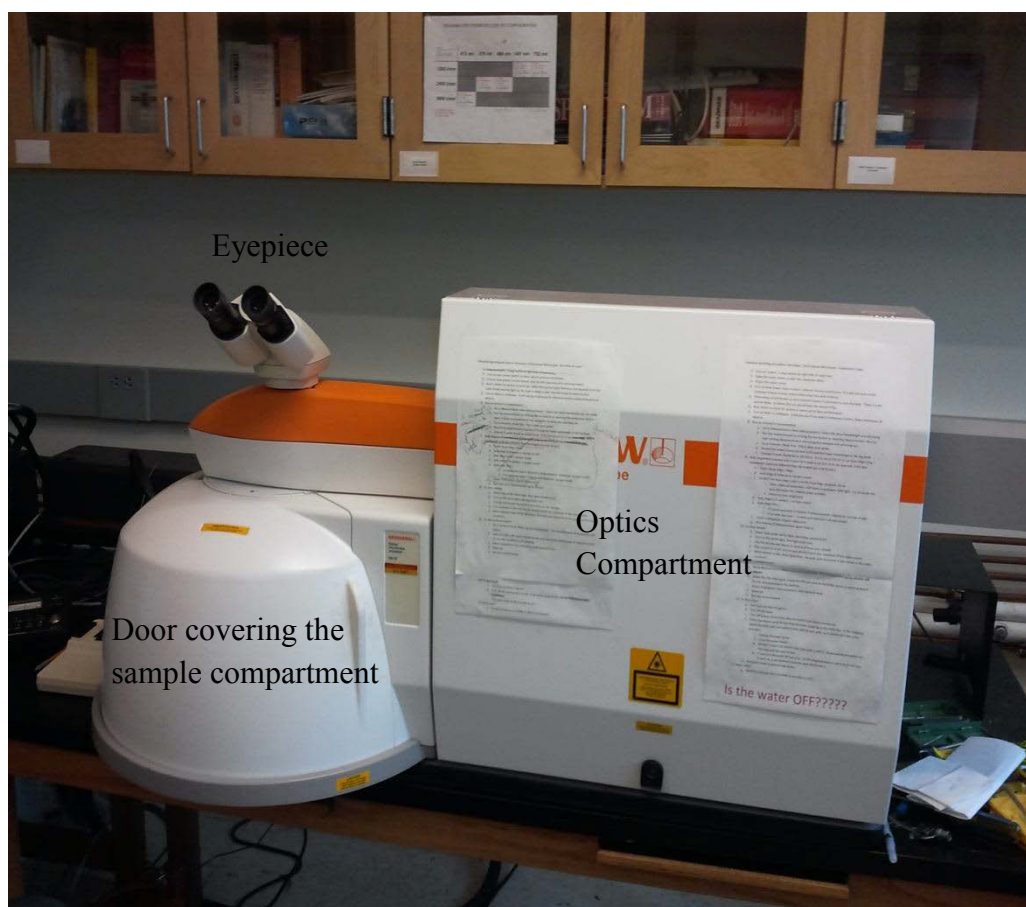


Figure 17: A Picture of the Raman Instrument

Two programs were used for data collection and analysis. Wire v3.1, supplied with the Raman dispersive instrument, was used to collect the Raman spectra. Most of the mapping analysis, data processing was performed in Wire. Some of the data was exported in text files to be analyzed in another software package called Origin v8.6.

1.6 Scope of This Research

This work is primarily focused on characterizing a chosen OPC and a set of chemically/physically different 3 FA's. This characterization is done by aiming at obtaining

the fingerprint spectra for each phase present in these multiphase systems. A complete, or as much as is possible, characterization is the first and foremost aim.

The secondary aim is to observe the evolution of the hydration products of binders containing OPC and FA as a function of time. The scope of this research is such that the hydration process is followed carefully and closely at early ages (with shortly spaced temporal intervals) and then is continued up to the age of 56 or 90 days.

The tertiary aim is then to focus on specific hydrating species; one of them is evolution of sulfates to see a possible depletion of Gypsum and formation of Ettringite, and to see the conversion of AFt to AFm. A secondary focus is to observe the spatial and temporal distribution of calcium hydroxide in various mixes and then to compare its growth with the pozzolanic reactivity of the given fly ashes.

Lastly, the observed phenomena from Raman spectroscopy will be correlated with results obtained from supplementary techniques. It must also be noted that the scope of this work is largely inclined towards a qualitative study of fly ashes and less towards a semi-quantitative analysis. A full-fledged quantitative analysis of the hydration products formed in the complex hydrating systems is clearly out of scope and would take additional time and money.

CHAPTER 2: LITERATURE REVIEW

2.1 Major Anhydrous Cementitious Minerals

The pioneering study of cement clinkers by Raman spectroscopy was conducted by John Bensted [34], after which he continued his work on application of Raman quite actively [35-37]. Following him, a few studies done by Conjeud and Boyer[38], Dyer and Hendra [39], Bonen[40] and Tarrida et al.[41] in the early eighties and the nineties were done. However, prior to the year 2000 most of these studies were conducted on primitive Raman spectrometers with low spatial and spectral resolution. With the advent of multi-channel detectors, charge-coupled devices more and more researchers have been interested in application of Raman spectroscopy to cementitious materials as is clear from the increased number of works available in the past decade [42].

In a comprehensive review, Richardson et al. [43] noted that Raman may not be a routine analysis technique but cementitious materials can be still studied by this technique to a certain extent considering its limitations. Fluorescence often hinders the effective study of OPC which can be avoided by using longer wavelengths like 1064 or 784 nm but again these high wavelengths result in occurrence of photo luminescent bands [39, 40] due to the rare earth elements embedded in a cement lattice.

Authors have suggested that although WPC (white Portland cement), oil well, CSA (Calcium Sulpho-Aluminate) cements have been largely studied by Raman, OPC (ordinary Portland cement) remains elusive. OPC analysis usually results in high background signals which may be due to a number of reasons. In the past it was assumed that it was probably due to the presence of Iron but later on it was disproved by some researchers studying oil well cement having 19% ferrite. The other explanation given was the introduction of defects due to particle scattering after the grinding process. A series of tests in the literature pointed out that primary reasons behind high fluorescence are: a) organic contamination b) inter particle scattering due to grinding. Authors have agreed on these conclusions and pointed out that

both of these factors can be removed by washing in organic solvents and photobleaching respectively as per the existing literature.

2.1.1 Calcium Silicates (Alite & Belite)

Based on the literature published in the past four decades, Alite (C3S) and Belite (C2S) are by far the most analyzed mineral phases of cement clinker by Raman spectroscopy. The primary reason behind that is the dominant abundance of calcium silicates in ordinary Portland cement, which is the most common type of cement used worldwide. A few researchers also chose White cement (free from iron oxides) for their studies as it is more suitable for Raman spectroscopy. Table 4 shows the Raman shifts for alite and Table 5

shows the Raman shifts for belite. All the strong peaks marked with s have been bolded for better presentation. Silicates provide a spectrum which is dominated by the internal modes of SiO_4^{4-} tetrahedral units. The symmetric and antisymmetric stretching of Si-O bonds, ν_1 and ν_3 occurs at 777 and 935 cm^{-1} , respectively. Also, the symmetric and antisymmetric bending of the O-Si-O bonds, ν_2 and ν_4 occurs at 448 and 607 cm^{-1} respectively. Any modes below 300 cm^{-1} usually belong to the external lattice modes of the Ca^{2+} and SiO_4^{4-} ions in calcium silicates [44].

A quick glance at the summarized Table 4 and Table 5 provide a summary of various experimental conditions, type of samples, and peaks assigned. It is to be noted that among majority of works there is some variance in the appearance of peaks which can be assigned to the different sample/experimental conditions noted herein. Table 4 for Alite clearly indicates that the major peaks are located within the 800-850 cm^{-1} region with many peaks around ~840 cm^{-1} . Similarly for Belite, as per Table 5 the major peaks are more spread out with 800-900 cm^{-1} ($\nu_1/\nu_3[\text{SiO}_4]^{4-}$) as the primary region of interest with several secondary minor peaks in 0-400 and 1200-1600 cm^{-1} region.

Table 4: Raman shifts for Alite

Year	Authors	Experimental Conditions	Mineral Phase	400-800 cm ⁻¹	800-1200 cm ⁻¹	1200-1600 cm ⁻¹
1976	J. Bensted [34]	514+632 nm	C ₃ S triclinic		848 s, 852 w	
1980	Conjeud and Boyer [38]	514.5 nm ?mW 1um	C ₃ S triclinic		845 s, 855 s, 813 m, 885 m	
		514.5 nm ?mW 1um	C ₃ S alite (OPC)	750 mbr	845 s, 832 s	
		514.5 nm ?mW 1um	C ₃ S alite (WC)		845 s, 832 m	
1993	Dyer and Hendra [39]	1064 nm 1000 mW	C ₃ S triclinic	574 sbr, 626 sh	1007 w, 1393 wbr	
		514 nm	C ₃ S triclinic		842 s	
1994	Bonen et al.[40]	1064 nm (FT) 65-5 um	C ₃ S triclinic	541 s, 714 sh, 798 w	925 wbr	1340 wbr
		1065 nm (FT) 65-5 um	C ₃ S monoclinic	593 s	935 w	1361 br
		1066 nm (FT) 65-5 um	C ₃ S alite (OPC)	666 s	1017 w	1431 w
1995	Tarrida [41]	514.5 nm 400 mW	C ₃ S triclinic	518 w, 542 w	840 s, 850 s, 809 ms, 880 ms	
2002	Deng et al. [45]	632.8 nm 5 mW 2 um	C ₃ S monoclinic (OPC)	517, 544 wm	838 s	

Table 4. (continued)

2005	Newman et al. [46]	1064 nm 4 mW 40 um	C ₃ S triclinic	570 s	940 wbr	
		1065 nm 4 mW 40 um	C ₃ S alite (OPC)	650 s	1000 wbr	1400 wbr
		514+632.8 nm 4 mW 40 um	C ₃ S triclinic		840, 890	
2006	Ramirez et al [47]	514.5 nm 50 mW	C ₃ S alite (WC)	539	836, 851	
2006	Ramirez et al [48]	1064 nm 50 mW (FT)	C ₃ S alite (OPC)	654		
2007	Ibanez et. al [49]	514.5 nm 2mW 1um	C ₃ S monoclinic	760	826 s , 840, 854, 892, 916	
2007	Black and Brooker [50]	514 nm 5mW 0.8 um 10s exp	C ₃ S alite (OPC)	521, 551, 735	834, 882	
2009	Frias and Ramirez [51]	784 nm 100 mW	C ₃ S alite (WC)	518-542	834, 851	
2011	Ramirez and Carrasco [44]	unknown	C ₃ S	520 w, 540 w	813, 845, 855, 885, 895, 903, 917	
2011	Chollet and Horgnies [52]	514 nm 5um	C ₃ S alite (OPC)	548	838, 880	

* s = strong, m = medium, w = weak, br = broad, sh = shoulder

Figure 18 shows typical spectra for pure forms of the two silicates. It can be seen that Raman spectroscopy is effective in distinguishing both major clinker components even though most of the peaks originate from same vibrational modes with some overlap. However, it must be kept in mind that while studying OPC there may be significant overlaps and the region around 800-850 may appear a broad hump instead of sharp peaks as will be seen later in the results of this study cm^{-1} .

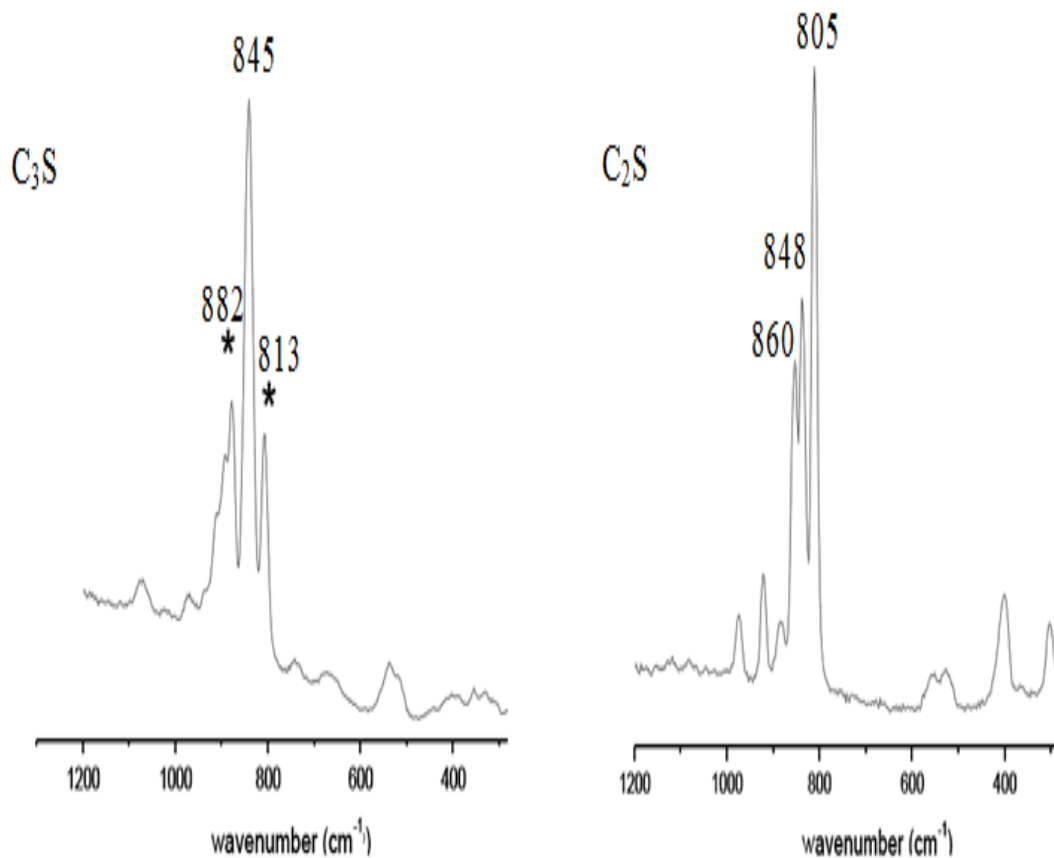


Figure 18: Raman spectra for Pure Calcium Silicates (* indicates satellite bands) [44]

Table 5: Raman shifts for belite

Year	Authors	Experimental Conditions	Mineral Phase	0-400 cm^{-1}	400-800 cm^{-1}	800-1200 cm^{-1}	1200-1600 cm^{-1}
1976	Bensted, J [34]	514+632 nm	α' -C ₂ S			828 s, 864 s, 892 s	
		514+632 nm	β -C ₂ S			852 sh, 864 s	
1980	Conjeud and Boyer [38]	514.5 nm ?mW 1um	β -C ₂ S (syn)		512 w, 556 w, 535 m	848 s, 860 s , 900 m, 979 m	
		514.5 nm ?mW 1um	C ₂ S belite (WC)		522 w, 540 w, 558 w	860 s, 848 s , 900 w, 980 m	
		514.5 nm ?mW 1um	C ₂ S belite (OPC)		740 mbr	848 s, 860 s	
1993	Dyer and Hendra [39]	1064 nm	β -C ₂ S (syn)			1023 sbr, 1105 sh	1376 wbr
		514 nm	β -C ₂ S (syn)			856 s , 972 m, 1084 w	
1994	Bonen et al.[40]	1064 nm (FT) 65-5 um	β -C ₂ S (clinker)		722, 799	1016, 1116	1389
		1065 nm (FT) 65-5 um	β -C ₂ S (syn)		679-671	980-1030, 1112-1125	1450-1460
1997	Remy et al. [53]	514.5 nm 0.4 W 5 um	α -C ₂ S (syn)	380-400	517-530	850-855, 900, 966	
		514.5 nm 0.4 W 5 um	β -C ₂ S (syn)		424, 520, 538, 556	845, 858, 896, 977	

Table 5. (continued)

		514.5 nm 0.4 W 5 um	γ -C ₂ S (syn)		400, 410	813, 838, 885, 924	
2002	Deng et al. [45]	632.8 nm 5 mW 2 um	C ₂ S (OPC)		422 wm, 554, 536, 516 wm	857 s, 976 w	
2005	Newman et al. [46]	1064 nm 4 mW 40 um	β -C ₂ S		730 m	805 s	
2006	Ramirez et al [47]	514.5 nm 50 mW	C ₂ S belite (WC)		420	851, 972, 1010, 1121	
2006	Ramirez et al [48]	1064 nm 50 mW (FT)	C ₂ S belite (OPC)			811, 1010, 1124	
2007	Ibanez et. al [49]	514.5 nm 2mW 1um	β -C ₂ S			843 s, 857 s , 876 w, 897 w, 915 w, 974 s	
		514.5 nm 2mW 1um	γ -C ₂ S			809	
2007	Black and Brooker [50]	514 nm 5mW 0.8 um 10s exp	C ₂ S belite (OPC)		423, 520, 535, 553, 735	846, 857, 896, 977	
2007	Gastaldi et al. [54]	632.8 nm 20 mW 50 um	β -C ₂ S (CSA)	396 vw	425 vw, 515 vw, 537 w, 557 vw	846 s, 861 vs , 899 m, 980 w	
2009	Frias and Ramirez [51]	784 nm 100 mW	C ₂ S belite (WC)		518-542	851, 887, 1010, 1121	
2011	Chollet and Horgnies [52]	514 nm ?mW 5um	C ₂ S belite (OPC)	371	416, 512, 533, 552	840, 853, 889, 945, 973, 1000	

2.1.2 Calcium Aluminates (Aluminate & Ferrite)

While calcium aluminates are individually less studied than the silicates, still there have been several studies focusing on the characterization of these clinker phases due to their significant role in evolution of alumino-sulfates and sometimes even ferrites. Figure 19 shows the typical spectrum for C_3A .

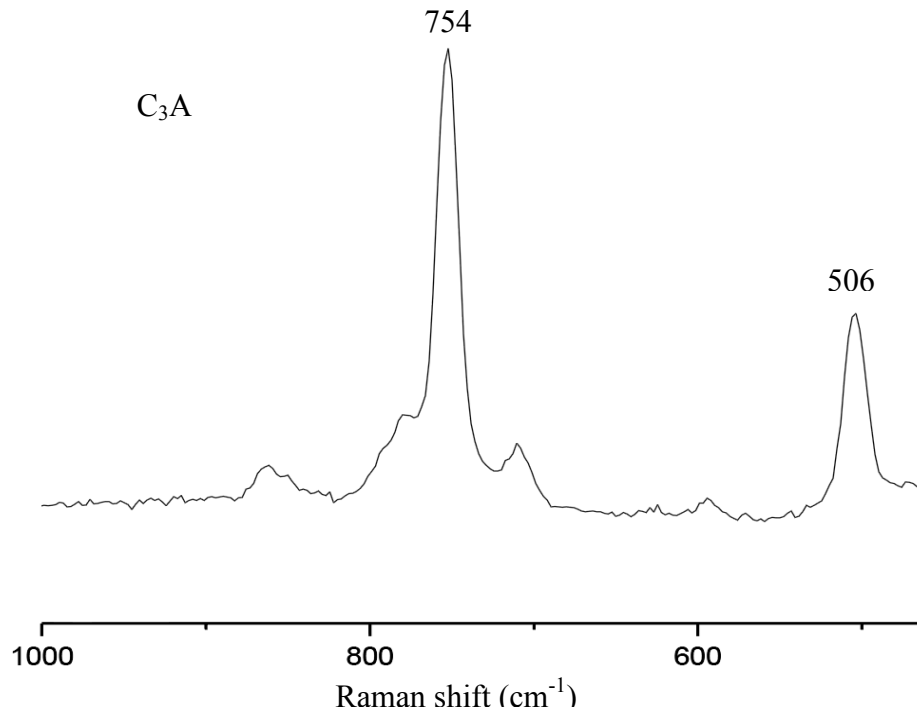


Figure 19: Typical Raman spectrum for C_3A [44]

Table 6 shows the Raman shifts for C_3A and Table 7 shows the Raman shifts for C_4AF . As can be seen from the Table 6

the spectra has major bands within the 400-800 wavenumber region. There are usually two dominant signals in most spectra, one at 761 cm^{-1} due to the stretching vibration of Al-O bond ($\nu_3[AlO_4]^{5-}$) and the other at 508 cm^{-1} corresponding to the deformation mode ($\nu_1[AlO_4]^{5-}$). Most of the past work has similar peak locations as seen in the tables.

Table 6: Raman shifts for C₃A

Year	Authors	Experimental Conditions	Mineral Phase	400-800 cm ⁻¹	800-1200 cm ⁻¹	1200-1600 cm ⁻¹
1976	Bensted, J [34]	514+632 nm	C ₃ A (clinker)	740, 756 m		
1980	Conjeud and Boyer [38]	514.5 nm ?mW 1um	C ₃ A aluminate (syn)	508, 761		
		514.5 nm ?mW 1um	C ₃ A aluminate (OPC)	750		
1993	Dyer and Hendra [39]	1064 nm	C ₃ A (syn)		1050 mbr	
1994	Bonen et al.[40]	1064 nm (FT) 65-5 um	C ₃ A cubic	504, 753	1083	1525
		1065 nm (FT) 65-5 um	C ₃ A ortho	493, 521, 763	1078	
2002	Deng et al. [45]	632.8 nm 5 mW 2 um	C ₃ A (clinker)	506 wm, 754 m		
2005	Newman et al [46]	1064 nm 4 mW 40 um	C ₃ A (syn)	510 w, 760 w		
2006	Black et al. [55]	632.8 nm 5 mW 5 um	C ₃ A cubic (syn)	506, 754		
2006	Ramirez et al. [47]	514.5 nm 50 mW	C ₃ A aluminate (WC)	731		
2007	Black and Brooker [50]	514 nm 5mW 0.8 um 10s exp	C ₃ A aluminate (OPC)	750		

Table 6. (continued)

2011	Chollet and Horgnies [52]	514 nm 5um	C ₃ A aluminate (OPC)	500, 749		
------	------------------------------	--------------	-------------------------------------	----------	--	--

Figure 20 shows the typical Raman spectrum for C₄AF which usually is dominated by high fluorescence. The common assignment includes three broad bands, one at 736 cm⁻¹ due to ν_1 [(Fe,Al)O₄⁵⁻] or [(Fe,Al)O₆⁹⁻], the second at 311 cm⁻¹ corresponding to ν_4 [(Fe,Al)O₄⁵⁻] or [(Fe,Al)O₆⁹⁻], and the third at 258 cm⁻¹ corresponding to ν_2 [(Fe,Al)O₄⁵⁻] or [(Fe,Al)O₆⁹⁻].

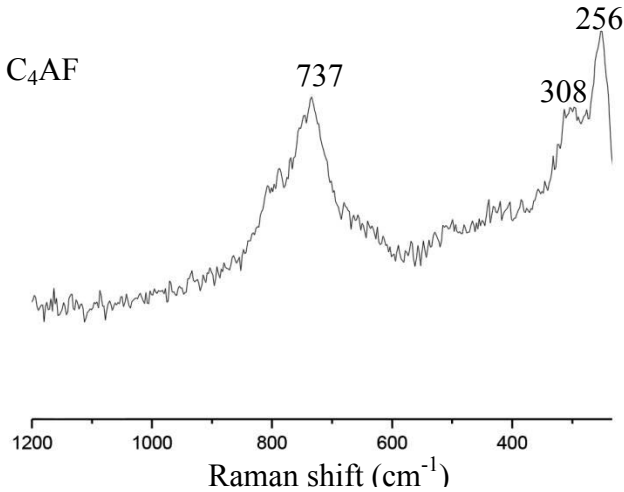


Figure 20: Typical Raman spectrum for C₄AF [44]

Table 7: Raman shifts for C₄AF

Year	Authors	Experimental Conditions	Mineral Phase	0-400 cm ⁻¹	400-800 cm ⁻¹	800-1200 cm ⁻¹	1200-1600 cm ⁻¹
1980	Conjeud and Boyer [38]	514.5 nm 1um	C ₄ AF ferrite (syn)		750		
1994	Bonen et al. [40]	1064 nm (FT) 65-5 um	C ₄ AF		581	1064	
2002	Deng et al. [45]	632.8 nm 5 mW 2 um	C ₄ AF ferrite (clinker)	256 m, 308 wm	737 m		
2007	Black and Brooker [50]	514 nm 5mW 0.8 um 10s exp	C ₄ AF ferrite (OPC)	265, 310	590, 695, 820		
2008	Gastaldi et al. [54]	632.8 nm 20 mW 50 um	C ₄ AF ferrite (OPC)	311 w	740 m		
2011	Chollet and Horgnies [52]	514 nm ?mW 5um	C ₄ AF ferrite (OPC)	260, 313	728	912	1461

Table 7 shows the Raman shifts recorded by previous researchers. As can be seen, there has not been much focus on characterizing C_4AF which is partly due to the fact that it forms a small percentage of the commercial clinker and partly due to the reason that its hydration chemistry is not well resolved.

Potgieter et al. [56] did a comprehensive analysis of various materials by Raman to see its applicability to commercial, impure materials like OPC, fly ash and slag. In their study, the ν_1 SiO_4 stretching vibration at 832 cm^{-1} indicating alite was seen in all laser wavelengths. The presence of ν_1 for belite was only seen by NIR (Near Infra-Red Region) at 860 cm^{-1} , showing that Raman is also suitable for analyzing clinker which is a composite of the above discussed silicates and aluminates. Figure 21 shows a Raman spectra for a OPC clinker nodule, and Figure 21 shows a composite figure for all the major clinker phases discussed so far.

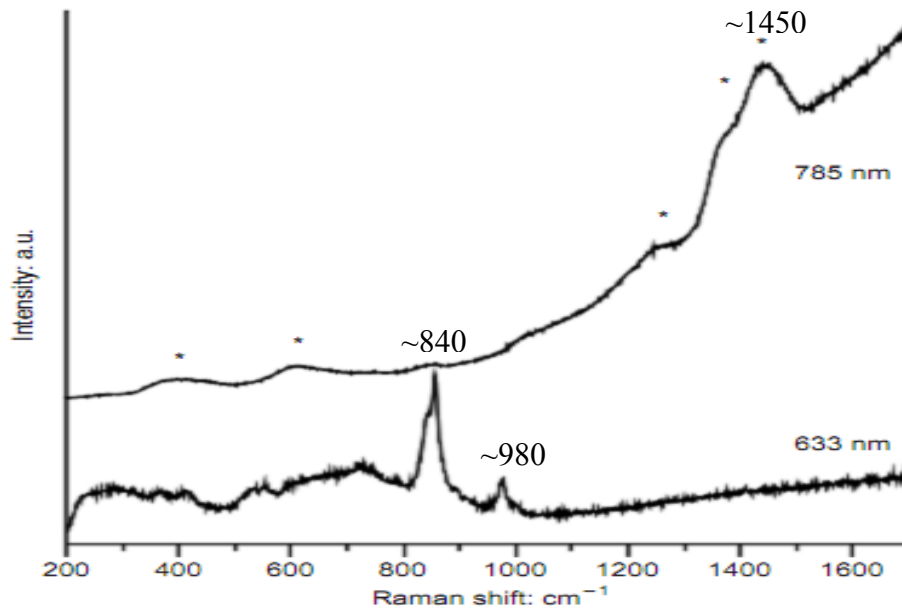


Figure 21: Raman spectra obtained from an OPC clinker nodule using 633 nm and 785 nm [43]

Figure 21 shows that in a clinker nodule, the final spectrum obtained is a blend of the four major phases discussed earlier and that is the primary reason previous researchers have focused on studying individual, pure components. However, this being said, application of Raman to real, composite systems is where the research will be focused in the coming years.

Figure 22 shows all the major phases separated by Y offsets to clearly represent the sensitivity of Raman spectroscopy towards detection of these principal phases. Gastaldi et al. [57] recently applied Raman to study the formation of mineral phases (by-products) in a rotary kiln for clinker production. The authors aimed to understand the chronological order of deposition of several overlapped layers of by products in order to improve the efficiency of the cement production process. They also noted that all principal phases characterized were in good agreement with parallel XRD studies and while “XRD requires accurate grinding and consequently leads to the destruction of the sample; micro-Raman analyses, instead, does not need any sample preparation.” While they found Raman to be advantageous for qualitative analyses of clinker principles, they also noted that, “quantitative information is not easy to be deduced from Raman spectra: the intensity of Raman bands depends on a number of variables and cannot be directly related to phase concentration in the sample.”

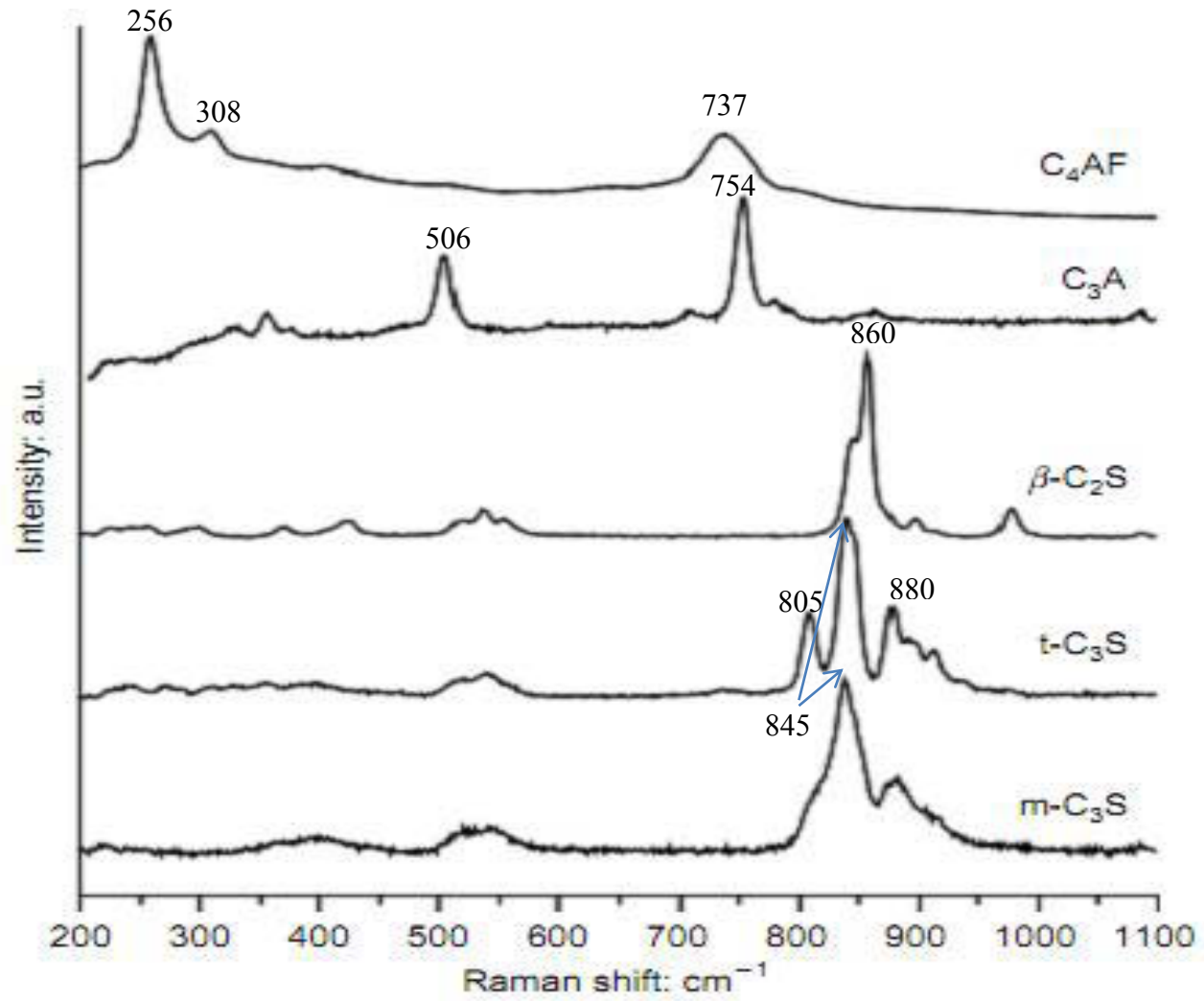


Figure 22: Raman spectra of the principal phases in anhydrous clinker [43]

2.2 Major Hydrous Cementitious Materials

Black [58] noted that, “considering the limitations of Raman spectroscopy, cementitious materials can still be studied to an extent.” Raman’s low sensitivity towards water to enable in-situ analysis, ability to couple with an optical microscopy resulting in a spatial resolution of a couple of microns, high sensitivity to sulfate and carbonate environment are some of its major advantages.

2.2.1 C-S-H

In Raman spectroscopy, crystalline phases result in sharp peaks due to consistent bond lengths and on the other hand amorphous phases result in broad, poorly defined bands due to the varying distribution of bond lengths and bond angles. The broad bands observed for the C-S-H phase in hydrated clinker reflects the absence of long range order in symmetry. The broad shape of the band is actually formed by the superposition of several adjacent symmetrically shaped bands around a region.

Table 8 shows the past work done on the characterization of C-S-H by Raman spectroscopy. There is usually a broad band in the 3000-3800 wavenumber region due to the OH stretching vibrations in the water molecules attached to hydrated calcium silicate. Then, the region 800-1200 cm^{-1} consists of Si-O silicate symmetrical stretching bands, wherein the frequency of the band changes with the extent of polymerization [44]; silicate units (Q^3) appear at 1050-1100 cm^{-1} , chains (Q^2) appear at 950-1010 cm^{-1} , dimers (Q^1) at 870-900 cm^{-1} and monomers (Q^0) at $\sim 850 \text{ cm}^{-1}$. Additionally, the wavenumber region 300-500 is due to $\nu_2[\text{SiO}_4]$ and the region 400-600 cm^{-1} is due to $\nu_4[\text{SiO}_4]$.

Table 8: Raman shifts for C-S-H gel

Year	Authors	Experimental Conditions	Mineral Phase	0-400 cm ⁻¹ ₁	400-800 cm ⁻¹	800-1200 cm ⁻¹
1980	Conjeud and Boyer [38]	514.5 nm ?mW 1um	C-S-H		640 wbr, 670 br	
1995	Tarrida [41]	514.5 nm 400 mW	C-S-H		524, 662	
1997	Kirkpatrick et al. [59]	488 nm	C-S-H		450, 664-669	950-1000
2002	Deng et al. [45]	632.8 nm 5 mW 2 um	C-S-H		450 w, 620, 680 w	850 wm
2004	Black and Breen [60]	632.8 nm	C-S-H		430-540, 600-630, 650-680	858, 960-980, 1010-1021
2006	Ramirez et al [48]	514.5 nm 50 mW	C-S-H (WC)		600-700	1133
2007	Ibanez et. al [49]	514.5 nm 2mW 1um	C-S-H		680 b	
2007	Garbev et al. [61]	633 nm 20 mW 5 um	C-S-H (syn) C/S = 1.5	333, 359	445, 495 vw, 672	889, 975 vw, 1022
2007	Black et al. [50]	633 nm 20 mW 5 um	C-S-H (syn) C/S = 1.5 (fresh)	333 s	445 s, 485 vw, 672 s	889 s, 865 sh, 935 w, 1022 s
			C-S-H (syn) C/S = 1.5 (6	330 sh	435, ~490, 665 w,	970 vw, 1009 vw

			months)		800 vw	
--	--	--	---------	--	--------	--

Richardson et al. [43] noted that Raman spectroscopy is useful to study the C-S-H phases which are dominated by symmetrical silicate bending bands at $\sim 670 \text{ cm}^{-1}$ and symmetrical stretching bands at $800\text{-}1050 \text{ cm}^{-1}$. While bending bands are insensitive to structural changes, the stretching bands are quite sensitive to extent of silicate polymerization.

Kirkpatrick et al. [59] compared the structures of C-S-H, Tobermorite, and Jennite with Raman spectroscopy found their atomic configurations in agreement with previously published data with XRD and NMR. C-S-H structure was related to the defect Tobermorite model. The C-S-H spectrum was found to have features similar to the spectra of 11, 14-Å Tobermorite and Jaffeite. Figure 18 shows one of their comparative results of C-S-H and naturally occurring minerals.

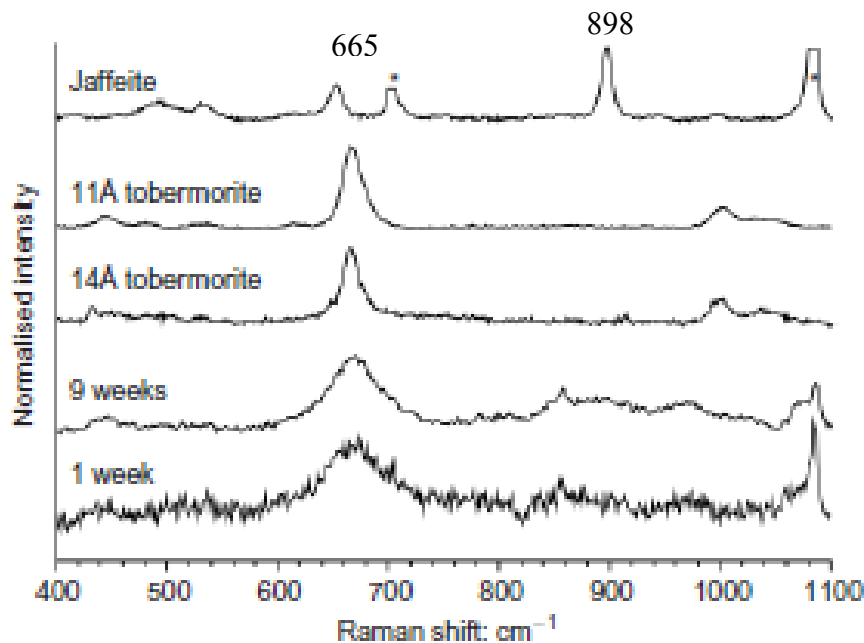


Figure 23: Raman spectra of C3S pastes plus those of crystalline 11Å and 14Å tobermorite and jaffeite. [59]

Garbev et al. [61] studied fresh C-S-H(I) phases in close detail to measure the extent of silicate polymerization as well as the effect of carbonation [50]. Sharp Q^2 and Q^1 bands for the silicate network were observed for mixes with low Ca/Si ratio indicating the presence of

uniformly distributed long chains and end groups of SiO_4 , respectively. Increasing the Ca/Si ratio resulted in depolymerization of silicates and broadening of the bands. Figure 24 shows a result from their study depicting the polymerization process of silicates.

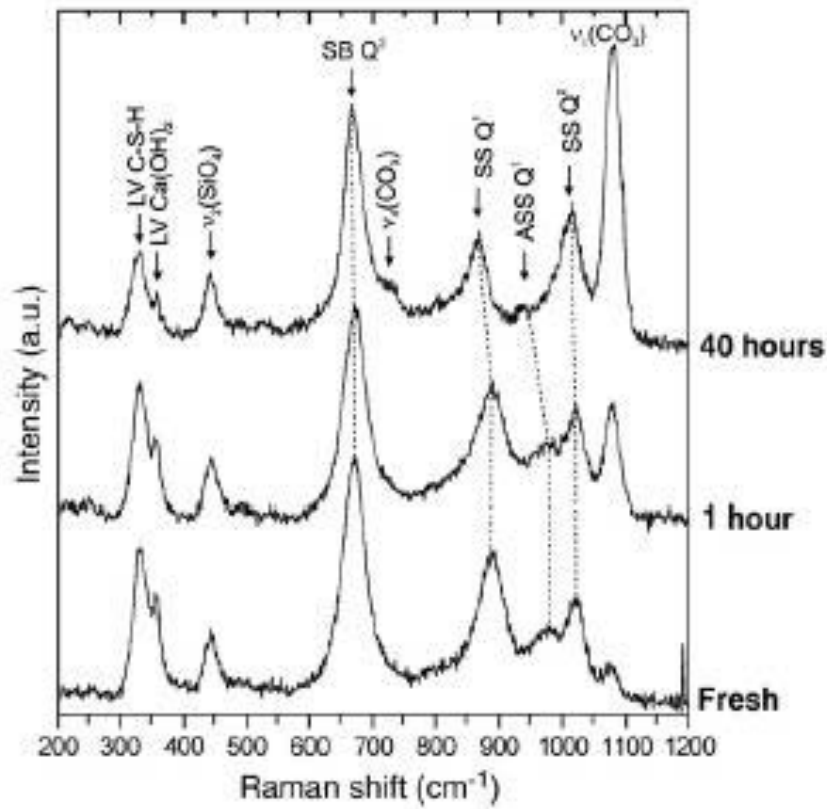


Figure 24: Raman spectra of C-S-H(I) synthesized with Ca/Si = 1.50 [50]

It must be noted here that the band positions for the C-S-H phase continuously change as a function of time, initial C/S ratio, and extent of polymerization. A very detailed discussion on that change is out of the scope of this thesis as C-S-H was not the target phase studied in this work. The reader is encouraged to refer to the articles cited in Table 8.

2.2.2 Portlandite

Portlandite is the mineralogical name for Calcium Hydroxide ($\text{Ca}(\text{OH})_2$) is crystalline in nature and thus has two well defined peaks in the past studies. The first one usually at 3616 cm^{-1} is due to the presence of OH stretching vibration and the second one at 353 corresponds to Ca-O lattice vibrations. Table 9 shows the Raman shifts for CH recorded by past researchers.

The crystal vibrations for CH were established by Padanyi [62] back in 1970s when he found four Raman active vibrational modes for CH. Based on the literature review summarized in Table 9, it can be seen that all four modes have been experimentally found over the years with the modes at 3616 and 356 most prominent.

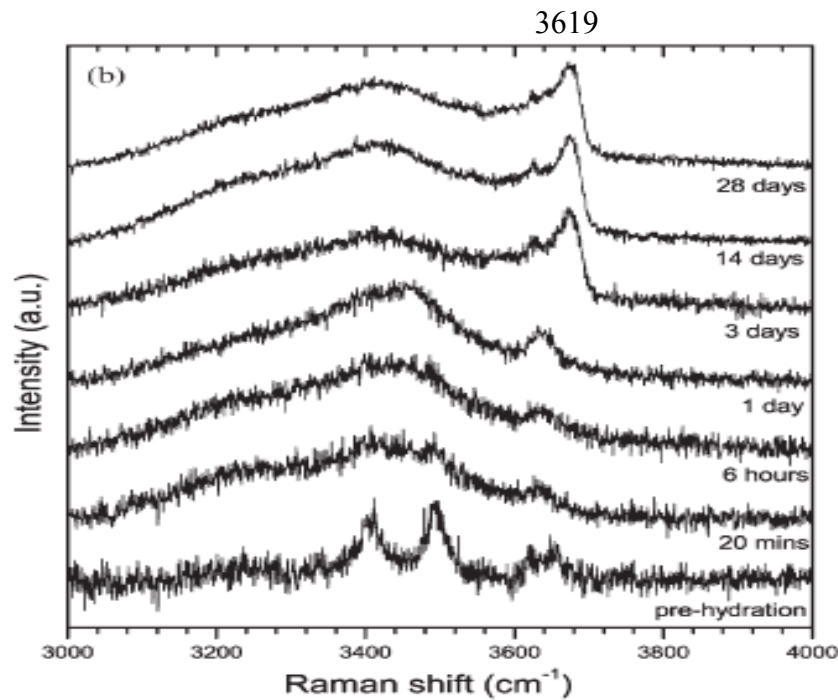


Figure 25: Evolution of Portlandite

Table 9: Raman shifts for Portlandite

Year	Authors	Experimental Conditions	Mineral Phase	0-400 cm ⁻¹ 1	400-800 cm ⁻¹	3000-4000 cm ⁻¹
1970	Padanyi [62]	514.5 nm 150 mW	Ca(OH) ₂ (syn)	260±4, 359±4	684±8	3620±5
1995	Tarrida [41]	514.5 nm 400 mW	Ca(OH) ₂ (syn)	253, 356	680 br	
2002	Deng et al. [45]	632.8 nm 5 mW 2 µm	Ca(OH) ₂ (hydrated clinker)	254 wm, 356 s	677 w	
2006	Black et al. [63]	632.8 nm 5 mW 5 µm	Ca(OH) ₂ (hydrated C ₃ A)	356		3620
2007	Black and Brooker [50]	514 nm 5mW 0.8 µm 10s exp	Portlandite	356		
2007	Ibanez et. al [49]	514.5 nm 2mW 1µm	Ca(OH) ₂	250, 355		
2009	Frias and Ramirez [51]	784 nm 100 mW	Ca(OH) ₂ (hydrated clinker)	356		3617
2011	Chollet and Horgnies [52]	514 nm ?mW 5µm	Ca(OH) ₂ (hydrated clinker)	354		3616

2.2.3 Calcium Aluminate Hydrates (C-A-H)

The literature on C-A-H phases is very little due to their infrequent presence or detection in common commercial clinkers. However, some authors have studied them and performed characterization work on identifying major phases. Table 10 shows the recorded Raman shifts from two past works.

Table 10: Raman shifts for C-A-H phases

Year	Authors	Experimental Conditions	Mineral Phase	400-800 cm^{-1}	800-1200 cm^{-1}	3000-4000 cm^{-1}
2006	Black et al. [55]	632.8 nm 5 mW 5 μm	C_4AH_{19} or C_2AH_8	510	825	
			C_3AH_6	540		
			$\text{C}_4\text{A}\bar{\text{C}}\text{H}_{11}$	530	1067	3540, 3627
			$\text{C}_8\text{A}_2\bar{\text{C}}\text{H}_{24}$	530	1060	3540, 3627
2009	Frias and Ramirez [51]	784 nm 100 mW	C_4AH_{13}			3650
			C_2ASH_8	531		3692

2.3 Others

This section covers additional components of hydrous/anhydrous cementitious mixes. Brief discussion on application of Raman spectroscopy to the study of environmental attacks like sulfate attack, carbonation etc is also included.

2.3.1 Sulfates

The major sulfate hydration product is ettringite which shows the following Raman bands: i) 3637 cm^{-1} ($\nu_1[\text{OH}]^-$) ii) $[\text{SO}_4]^{2-}$, ν_1 at 989 cm^{-1} , ν_2 at 450 cm^{-1} ; ν_3 at 1114 cm^{-1} and ν_4 at 605 cm^{-1} ; iii) 550 cm^{-1} (Al-(OH)) stretch [44]. When gypsum or any other form of sulfate is not present in the system, aluminate phases from the clinker hydrate rapidly to form needle like hexagonal hydrates C_4AH_{19} and C_2AH_8 , with subsequent conversion to C_3AH_6 . However, when Gypsum is available, the sulfate to alumina ratio decreases which favors the formation of monosulphoaluminate phase (AFm). This phase can be easily distinguished from the AFt phase as its ν_1 sulfate mode appears at 982 cm^{-1} which is far from the principle ettringite peak at $989\text{--}991\text{ cm}^{-1}$. Also, the water molecules present in AFm stretch to induce a Raman shift at 3688 cm^{-1} which is 50 cm^{-1} away from the OH stretch of AFt phase at 3637 cm^{-1} . Table 10 shows the Raman shifts for various sulfates (both hydrous and anhydrous forms are grouped together for better comparison and reference).

Renaudin et al. [64] did an extensive Raman study on comparison of Ettringite and Monosulfoaluminate in which they were successful in proving that Raman spectroscopy is capable of distinguishing between these two major sulfate hydration products. They used Raman to probe the inter-columnar and inter-lamellar regions of the sulfate structures. They found that the most significant advantage of employing Raman to study these phases was that there was no sample preparation required and hence the experimentation involved no risk of damage to these compounds. Figure 26 shows major results from the authors' comparison of the two phases.

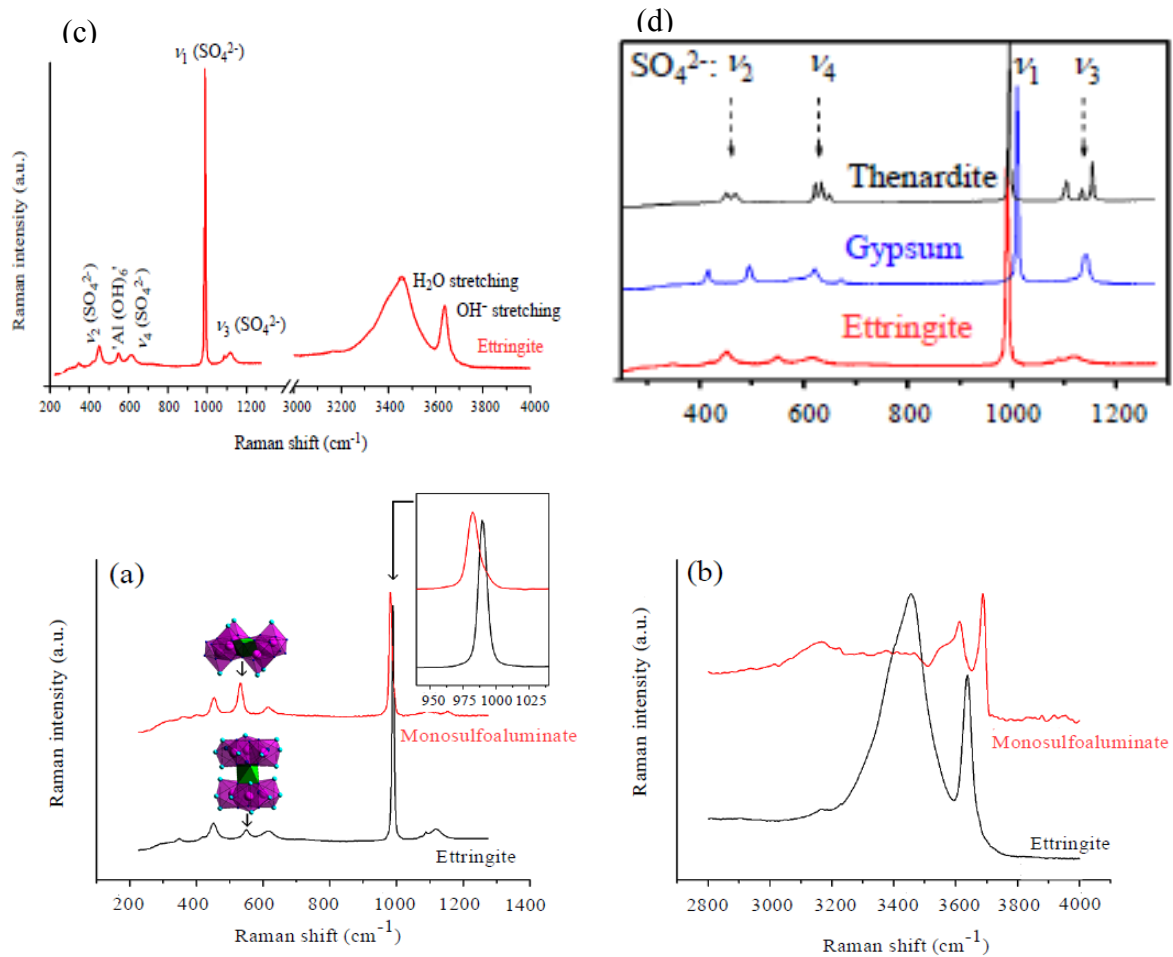


Figure 26: Raman shifts for hydrated sulfates [64] (a) & (b) show the comparison of AFt and AFm at lower and higher wavenumber regions respectively, (c) shows the fingerprint spectrum for pure ettringite crystal, (d) shows comparison between the sulfate stretching modes of thenardite, gypsum, and ettringite.

Out of the four main components of cement, two of them, C_3S and C_2S hydrate over a long period of time contributing to the mechanical strength, while the other two, C_3A and C_4AF hydrate rapidly controlling the setting time of cement. If gypsum ($\text{CaSO}_4 \cdot 2\text{H}_2\text{O}$) is present, it reacts with C_3A and forms a layer of ettringite (AFt) on the grains which retards the formation of hexagonal hydrates thus preventing flash set. If the system contains sufficient sulphur, AFt is stable but if the sulfur/aluminium ratio falls below $3/2$ then it is not stable and converts to monosulphate (AFm). This creates more AFm which further reacts with unhydrated C_3A and forms more AFm until all of it is consumed. XRD can report the presence on only certain crystalline phases and that too only at longer times whereas Raman may be used to do rapid in-situ analysis at very early ages.

Black et al. [63] pursued a detailed experiment on hydration of C_3A in the absence and presence of Gypsum to obtain AFt or AFm. The samples were prepared with S/Al ratios of 0, $\frac{1}{2}$, $\frac{3}{2}$ with a w/b of 0.5 and mixed for 1 minute. They were stored in upturned lids, covered with parafilm and sealed with inverse glass vials so as to store them for later ages. It is to be noted here that while sample preparation is not a big issue in Raman studies, sample storage is critical to avoid deteriorating processes like carbonation, surface drying [49]. Some of these problems were experienced by the author in this present work and their adverse effects are briefly discussed in the results section of the carbonated paste samples.

A 632.8nm (25mW) laser with notch filter at 200 cm^{-1} was calibrated with Silicon at 520 cm^{-1} . Recent studies usually employ low wavelength lasers in the visible range. A particular area was studied in the first 24 hours and after that different areas were chosen up to 28 days. There was a 10 second exposure, 3 accumulations at $200\text{--}1700\text{ cm}^{-1}$ and $3000\text{--}4000\text{ cm}^{-1}$ and each sample was analyzed in triplicate. The exposed surfaces reacted very fast with carbonation and that effect was also shown through selected spectra in their paper.

The characteristic C_3A bands were found at 506 and 754 cm^{-1} . The strong bands at 1368 and 1397 were found to be Cr^{3+} emission lines due to impurities causing ruby fluorescence. The C_3A bands reduced by time as hydration products formed and increased. In the $3000\text{--}4000\text{ cm}^{-1}$ band region, there were additional OH stretching bands when sample was exposed to CO_2 other than the characteristic ones of AFm. In the mix with sufficient amount of gypsum with C_3A , the bands of Gypsum (1000 , 670 cm^{-1}) and C_3A gradually faded and gave rise to characteristic bands of AFt (988 cm^{-1}). The extensive work clearly showed the strength of Raman spectroscopy in following the hydration of aluminates and subsequent conversion of AFt to AFm. Similar studies are also conducted in this thesis work.

Table 11: Raman shifts for sulfates

Year	Authors	Experimental Conditions	Mineral Phase	0-400 cm^{-1}	400-800 cm^{-1}	800-1200 cm^{-1}	3000-4000 cm^{-1}
1978	J. Bensted [65]	632 nm	Gypsum		414 mw, 494 mw, 622 w, 624 w, 676 w	1010 vs, 1114 w, 1138 w, 1144 w	
			Hemihydrate		438 mw, 494 mw, 602 w, 678 w	1018 vs, 1132 w, 1150 w, 1174 w	
			Anhydrite		438 mw, 498 mw, 604 w, 636 w, 678 w	1020 vs, 1131 w, 1150, 1172 w	
1999	Chang et al.[66]	514.5 nm 20 mW	Gypsum	176	416, 494, 622, 672	1010, 1138	341, 3498
			Hemihydrate		434, 488, 630, 672	1017, 1124, 1154, 1168	3516, 3568
			Anhydrite		423, 490, 612, 630, 670	1024, 1120, 1166	
2001	Prasad et al. [67]	514 nm	Gypsum		420 mw, 494 mw, 623 w	1008 vs, 1114 w	
			Hemihydrate		421 mw, 490 mw, 630 w, 680 w	1014 vs, 1152 w, 1174 w	

Table 11. (continued)

2002	Deng et al. [45]	632.8 nm 5 mW 2 μ m	Gypsum		491 wm, 626 wm	1010 s, 1135 wm	
			Ettringite	450 wm	615 wm	988 s	
2002	Sahu et al. [68]	532 nm 100 W	Thaumasite		417 w, 453 w, 479 w, 658 s	990 s, 1076 s	
			Ettringite			990 s, 1088 s	
			Gypsum		417 w, 496 w, 621 w, 673 w	1009 s, 1137 w	
2006	Black et al. [63]	632.8 nm 5 mW 5 μ m	Gypsum	415	620, 671	1009, 1137	3404, 3495
			Aft (C6AS ⁻ 3H32)		450, 550, 605, 989, 1114		3637
			Afm-14 (C4AS ⁻ H14)	215, 360, 396	447, 531, 614	983, 1114	
			Afm-12 (C4AS ⁻ H12)			981	
2007	Gastaldi et al. [54]	632.8 nm 20 mW 50 μ m	Anhydrite		417 m, 499 m, 609 m, 627 m, 676 m	1018 vs, 1130 m, 1161 w	

Table 11. (continued)

2007	Renaudin et al. [69]	514.5 nm 15 mW 1 μm	Gypsum			1009	
			Ettringite		451, 549, 615	988, 989, 990, 991, 992, 1087	3440
			Monosulfate /AFm		453, 532, 615	982, 991 sh, 1095/1154	3688
			Gypsum		414 w, 493 w, 618 w, 671 w	1007 vs, 1096 w, 1135 m	
2009	Frias and Ramirez [51]	784 nm 100 mW	Monosulfate		450, 529	986, 991	3676
2011	Chollet and Horgnies [52]	514 nm ?mW 5μm	Ettringite			989	

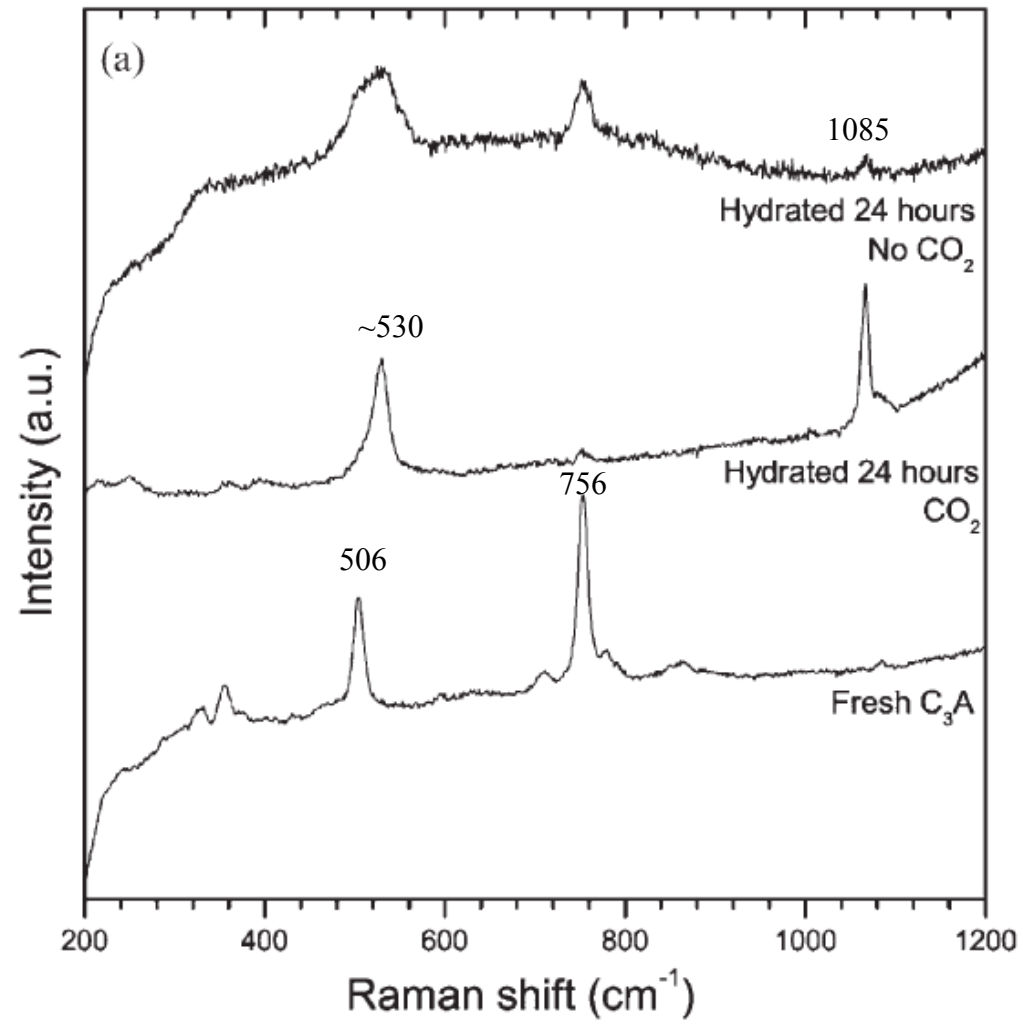


Figure 27: Damaging effect of CO₂ on C₃A [63]

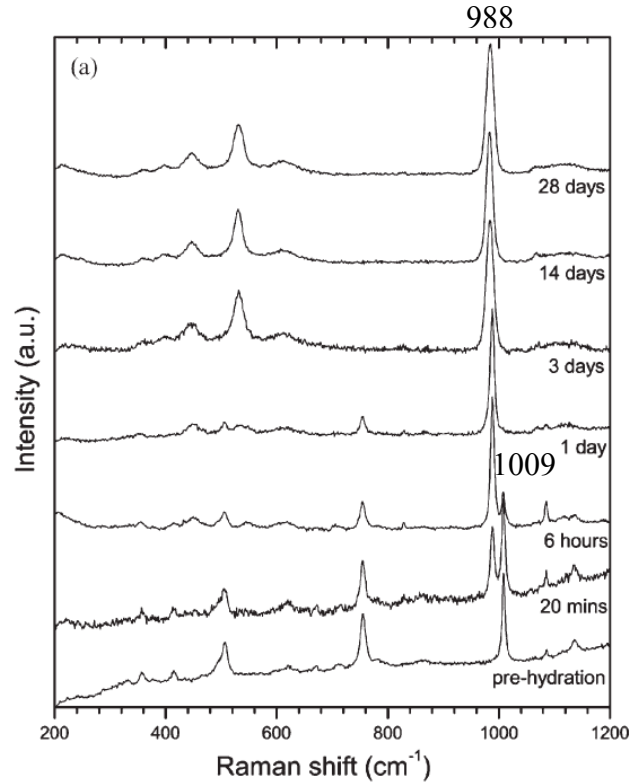


Figure 28: Disappearance of Gypsum and formation of Ettringite in C_3A paste [63]

Livingston et al. [70] studied the decomposition of ettringite group crystal by parallel application of XRD and Raman spectroscopy. They were successful in studying the breakdown of crystalline beginning phase into a final amorphous product, and the results from XRD and Raman were in well agreement. Gastaldi et al. [54] proposed Raman spectroscopy as a versatile characterization tool for calcium sulfoaluminate cements for studying their composition as well as following the hydration progress. They concluded that Raman can serve as an effect quality control technique which monitor the product process of CSA cements onsite without any sample preparation, which is an operation impossible to perform by a technique like XRD.

Brough and Atkinson [71] efficiently applied Raman spectroscopy for the detection and indentification of Thaumasite. With a good spatial resolution, they were able to distinguish Thaumasite in veins from ettringite in two specimens of field concrete. Sahu et al. [68]

combined Raman spectroscopy with optical and digital imaging to detect thaumasite in concrete. The authors found that Raman chemical imaging was powerful in determining the spatial distribution of thaumasite in an excellent way. Jallad et al. [72] applied Near Infrared Raman imaging microscopy to clearly reveal thaumasite, ettringite and gypsum microstructures which are not so easy to distinguish by XRD or SEM.

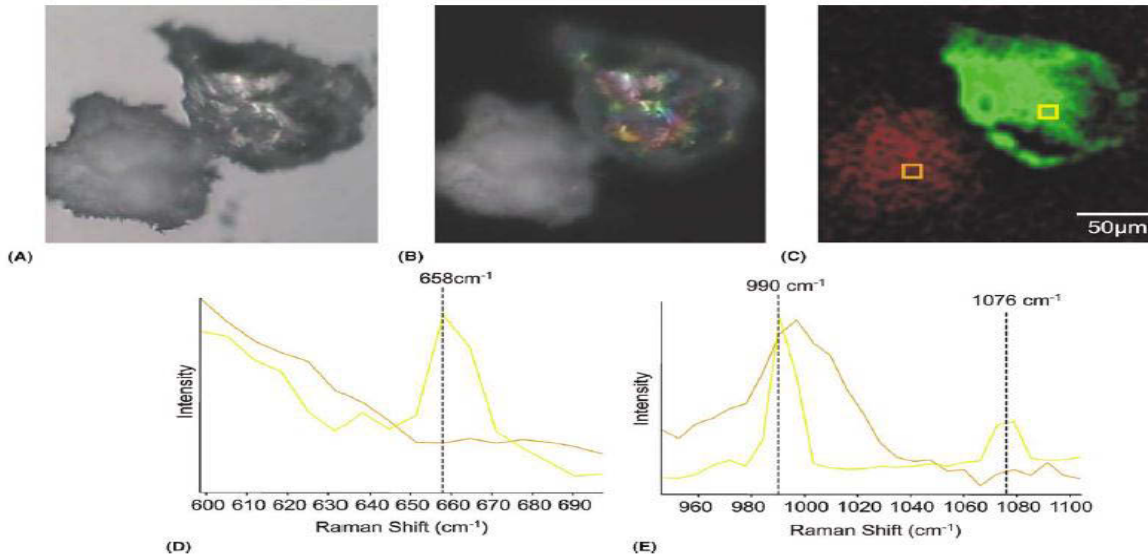


Fig. 3. Raman chemical imaging of thaumasite and ettringite: (A) Brightfield reflectance image; (B) polarized light image; (C) RGB image; and (D) LCTF-generated Raman spectra associated with thaumasite (yellow box) and ettringite (orange box), respectively. (10× magnification, 10 s per frame, LCTF tuning parameters: 600–700 and 950–1100 cm⁻¹, 43 W/cm² laser power density at sample).

Figure 29: Raman chemical imaging distinguishing thaumasite (yellow) to ettringite (orange) [68]

2.3.2 Carbonates

Calcium carbonate phases are formed due to the carbonation of major hydration products of cement clinker like C-S-H or CH. Out of three main identified phases (calcite, vaterite, and aragonite), vaterite is the least thermodynamically stable phase. However, often the surface carbonation of CH by ambient CO₂ results in formation of vaterite. The vibrational bands for calcium carbonate phases can be split into three main groups: i) symmetric stretching $\nu_1[\text{CO}_3]^{2-}$ ii) split in-plane bending vibrations $\nu_4[\text{CO}_3]$ and iii) Ca-O lattice vibrations. Figure 22 shows the distinction between the three phases at two different wavenumber regions, and Table 12 contains the major Raman shifts recorded for calcium carbonate phases so far.

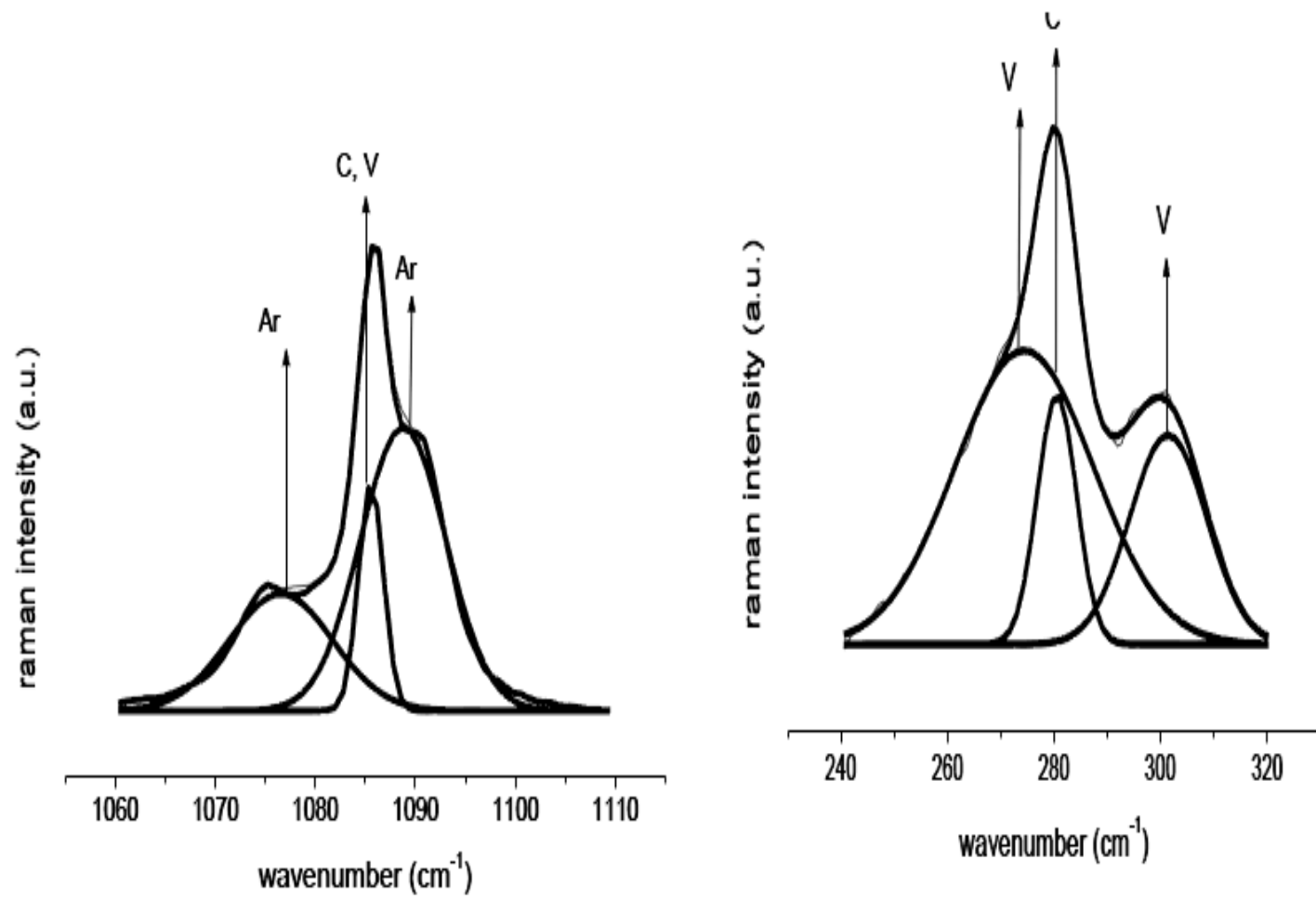


Figure 30: Calcite (C), vaterite (V) and aragonite (Ar) [44]

Table 12: Raman shifts for carbonates

Year	Authors	Experimental Conditions	Mineral Phase	0-400 cm^{-1}	400-800 cm^{-1}	800-1200 cm^{-1}	1200-1600 cm^{-1}
1977	Bensted [36]	1064 nm	Aragonite			852-854 vw	
		785 nm	Calcite	280 w	712 w	1085 vs	1450 w
			Aragonite	205 w	700+704 w	1085 vs	
			Vaterite	300	740+750 w	1074+1090 vs	
1994	Bonen et al. [40]	1064 nm (FT) 65-5 um	Calcite	156, 278	714	1087	1432
2002	Deng et al. [45]	632.8 nm 5 mW 2 um	Calcite	280 m	714 m, 879 m	1087 s	
2006	Black et al. [63]	632.8 nm 5 mW 5 um	Calcite	280	713	1085	
			Aragonite	207	704	1085	
2007	Ibanez et. al [49]	514.5 nm 2mW 1um	Aragonite	205	700, 705,	1085	
			Vaterite	301	738, 750	1074, 1089	
2011	Chollet and Horgnies [52]	514 nm ?mW 5um	Calcite	156, 283	713	1083	

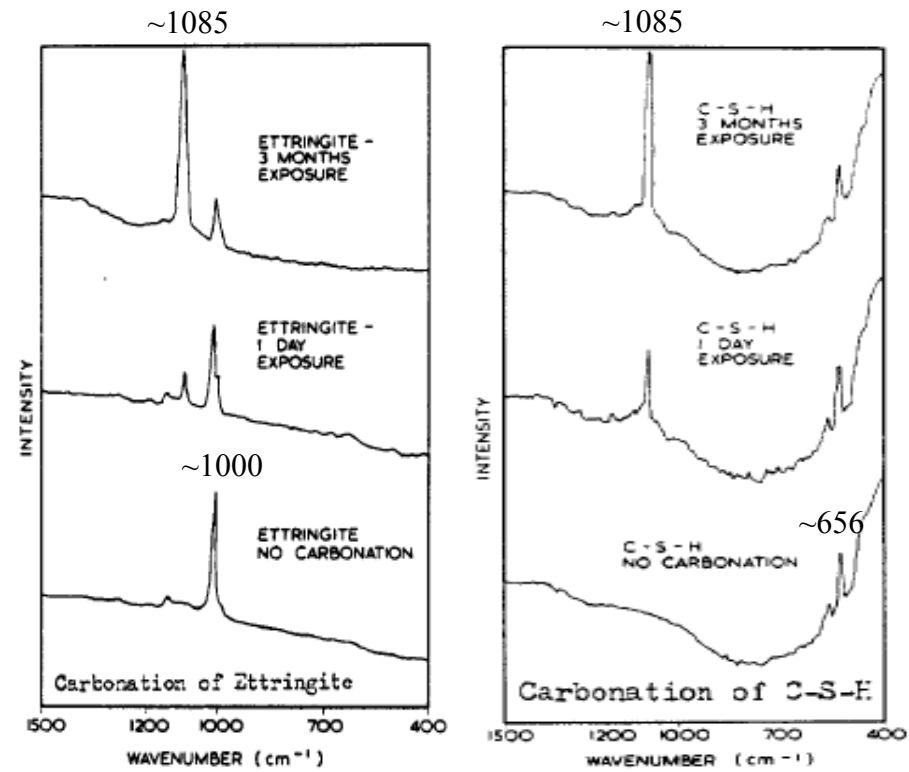


Figure 31: Effect of Carbonation on Ettringite and C-S-H (growth of peak ~1080) [36]

Martinez et al. [73] reported three active vibrational modes for calcite ν_1 (1085), ν_3 (1450) and ν_4 (712). All three phases of calcium carbonate were studied at different depths of lime mortar and their spectra were peak fitted by standard crystals precipitated in laboratory. The peaks at a wavenumber below 400 were related to the lattice mode, the area of those peaks in ratio to other peaks (A280/A712) was used to correlate with the crystal size. The ratio of different bands was also compared to establish the relative amounts of calcite and aragonite present. No vaterite was found to be present in carbonated lime mortar. However, while Raman was found to be effective in distinguishing these species, no clear relationship between mortar depth and carbonate polymorphs was found. The authors suggested further research on quantification and possible correlations between depth and carbonate phases.

Black et al. [50] did an extensive study on carbonation on synthetically prepared C-S-H phases with varying C/S ratio. While C_3S pastes often carbonate leading to formation of calcite, it was interesting to find a different behavior in the carbonation of C-S-H. Based upon the bulk composition, when $C/S < 0.83$ aragonite was formed and when $C/S > 0.83$ vaterite was formed. Tlili et al. [74] characterized $CaCO_3$ hydrates by micro-Raman spectroscopy for the first time in 2001. Although these hydrates have not much relation with cementitious hydrates, it is important to note that Raman spectroscopy was successfully applied towards distinction of possible varieties of calcite, while being able to detect both crystalline and amorphous phases. Gabrielli et al. [75] applied in-situ Raman spectroscopy to electrochemical scaling for characterizing different phases of calcium carbonate. Raman was able to unambiguously determine the vaterite structure and it matched well with the crystal structure proposed in the literature.

Hence, Raman seems to have a lot of potential in studying the phenomena of carbonation. Figure 32 shows the various phases formed due to the result of carbonation of cementitious materials. In this study too, some results on carbonation are shared (see the results section).

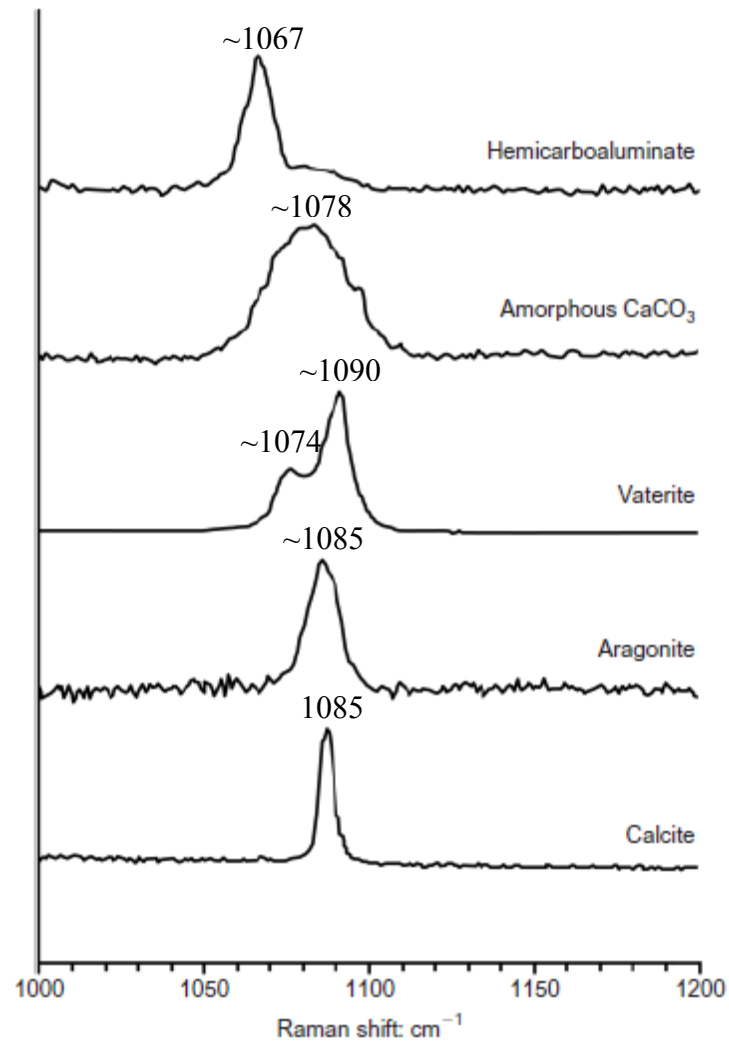


Figure 32: ν_1 carbonate bands of phases observed on aged cement samples [43]

2.3.3 Fly Ashes

There is only sparse literature on the application of Raman spectroscopy to fly ashes. Grieken and Xhoffer [76] reviewed various techniques for microanalysis of individual environmental particles in 1992 and stated that, “although Raman microprobe analysis has been available for more than a decade and offers a fantastic potential, so few publications on its environmental application are available.”

Table 13 shows the summary of observed modes for relevant studies conducted on fly ashes. Studies on bottom ashes, other CCPs, and carbonaceous aerosols were excluded from this review.

Scheetz and White [77] concluded that Quartz, sulfates and other silicates give the cleanest spectra while disordered silicates, aluminosilicates, and opaque minerals are rather difficult to measure. Also, the capability of Raman to do grain-by-grain analysis was proposed as an effective way to do bulk characterization of fly ash samples.

Guedes et al. [78] employed micro-Raman spectroscopic analysis to study fly ash samples collected from different locations of a coal power plant to characterize various inorganic and organic materials present in a fly ash. They were efficiently able to characterize individual grains showing phases of quartz, hematite, magnetite, calcite, glass, aluminium and calcium oxides as well as different types of organic constituents. They found Raman as a quick analysis technique for studying fly ashes. Figure 33 shows a selected result from their study.

Table 13: Raman shifts for fly ashes

Year	Authors	Experimental Conditions	Mineral Phase	0-400 cm ⁻¹	400-800 cm ⁻¹	800-1200 cm ⁻¹	1200-1600 cm ⁻¹	3000-4000 cm ⁻¹
1985	Scheetz and White [77]	514.5nm 10-20 mW	Quartz	200, 263, 355, 356	461 s, 463			
			Anhydrite		415, 497, 626, 674	1016		
1994	Bonen et al. [40]	1064 nm (FT) 65-5 um	Gypsum Quartz	128, 206, 265, 355	414, 492, 616 465	1006 809, 1081		
2006	Potgieter-vermaak [56]	514.5 nm 25 mW	Carbon				1353, 1603	
			Quartz		461			
			Anhydrite			1016		
			Magnesioferrite/Iron Chromite	343	484, 537, 709, 724			
			Iron Sulphide	228.8, 295.7	412.8			
			Calcium aluminate glass		730			
2008	Guedes et al.	632.8 nm	Quartz	202, 265	463			

	[78]							
			Hematite	226, 247, 293	413, 498, 614			
			Magnetite	213, 288, 348	441, 537, 653	905		
			Calcite	158, 282	711	1087		
			Cements, hydroxides			858		3425, 3626
			Aluminium oxides	683				
			Fe-oxides, glass and $\text{Fe}_2(\text{SO}_4)_3$	213, 328	480, 640, 707	826, 898, 1014, 1103		

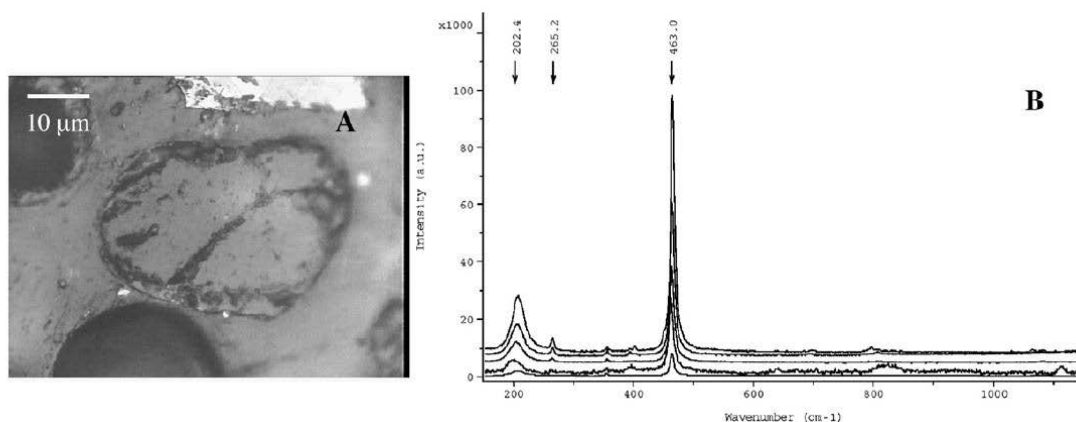


Figure 33: Analysis of a Quartz grain a) Microscopic image of particle analyzed b) Raman Spectra

In a nutshell, while some literature pertaining towards dry analysis of fly ashes is available, there is absolutely no study involving the characterization of wet pastes having OPCs blended with fly ashes, to the author's knowledge. The reason behind this maybe two fold. One, as is seen from the literature review, OPCs and fly ashes are by themselves inherently, complex, heterogeneous materials, which, when combined, may result in a spectra which is incomprehensible and potentially difficult to analyze. The second reason is somewhat related to the first one, in the sense that Raman's application to such systems have only recently witnessed a surge of interest and with lack of available literature, there is a need for more similar studies to appear in the cement science community before bold attempts to study such composite mixtures can be made.

2.4 Why use Raman spectroscopy?

Raman spectroscopy, being relatively immature in the field of cement science, may often be the target of the questions, "Why use Raman spectroscopy?" or "What has Raman to offer as opposed to XRD, NMR, DTA/TGA etc?" The justification of using and studying Raman can be laid down by considering some of the advantages and the limitations this technique offers.

2.4.1 Advantages

The advantages have been often proposed by the authors of the articles referred to in the previous sections and thus are not entirely the views of the writer.

- Raman is a completely non-destructive technique as it requires virtually no sample preparation or manipulation and has the potential to follow the hydration process of cementitious materials and characterize the evolving hydration products. In comparison to XRD which requires the hydration process to be stopped and the sample to be grinded before analysis can be done. This involves time and skill. SEM analysis requires time and skill demanded by various sample polishing/etching techniques, which again may be destructive to the sample surface and hence not completely representative.
- Raman offers the capability of in-situ live studies of samples. The development of on-site, portable Raman spectrometers has made this possible in various fields. Similar options may look bright for cement science once the technique is widely accepted. Raman instruments can be bundled with fiber optics to collect data from sample locations which are not generally accessible for the user or instrument itself.
- The unique mapping capability of Raman sets it apart from most techniques out there as it can give a representative distribution of hydration products on a given area of a sample, often on the bulk scale (order of a few millimeter square)
- In comparison to NMR, Raman is much cheaper, and does not require highly trained individuals to conduct a nominal spectrum run. While NMR can only probe the local structure around a molecule, Raman is capable to probe the global structure in a material.

2.4.2 Limitations

The list of advantages above is by no means exhaustive and there may be several more depending upon the need and requirement of the hour. However, it must be kept in mind that as with every technique, Raman has its own limitations too (which shall be clearer as we move forward in this thesis work). Some of them are noted as follows:

- There is a lack of available or established literature for Raman spectra of various chemical species, especially its application in the field of cement science is currently premature.
- Comparison of results (intensity/quantitative) from one Raman instrument to another is often difficult as the intensity is usually dependent on the laser power, cell geometry, and instrumental characteristics.
- Raman spectroscopy does not have the best detection limits and is not suitable for trace analysis.
- Lastly, and most importantly, the efficiency of the Raman process is very low as only a small fraction of the incident photons are converted to scattered photons that reach the detector. This results in making fluorescence emissions and background the biggest challenge towards obtaining true Raman bands.

Ultimately, any technique cannot replace the other, nor it can serve as one final answer to all problems of characterization. A variety of techniques must be used to probe a material if a complete characterization has to be performed.

Lastly, the writer wishes to share an interesting graph (Figure 34) that came across recently which explains the steep growth of Raman spectroscopy these days. (Not to mention the previous literature review tables, which were shown chronologically, prove that the majority of literature is published in the last few years).

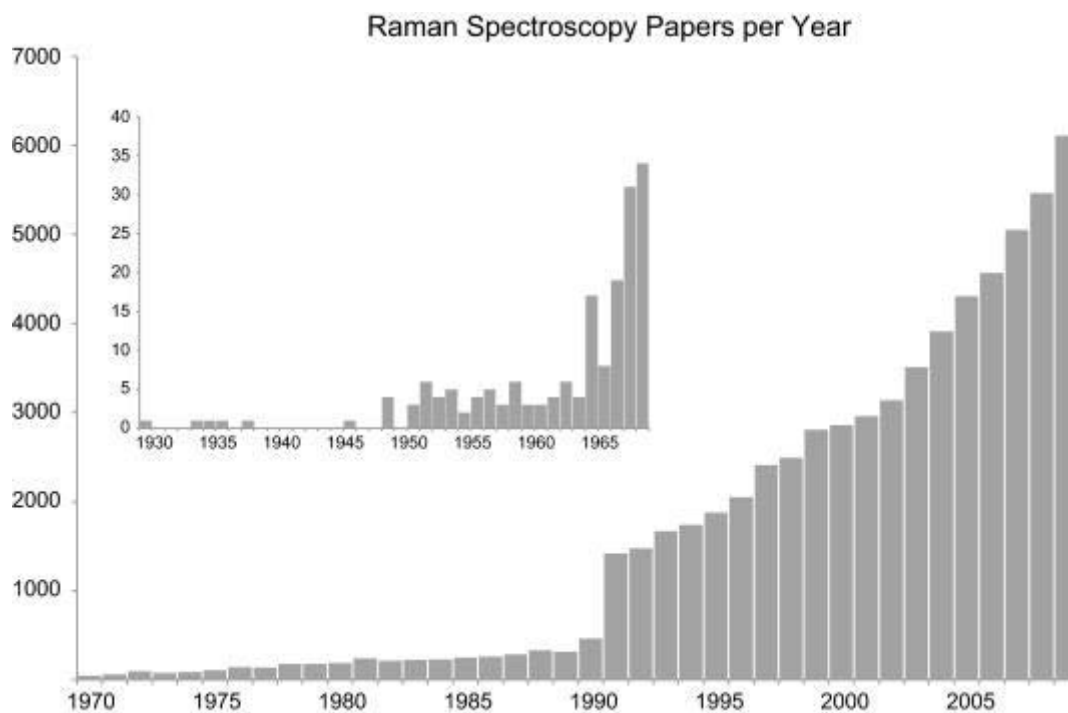


Figure 34: Based on Thomas Reuters Web of Knowledge database [79]

CHAPTER 3: EXPERIMENTAL PROGRAM

3.1 Introduction to Materials (Cementitious Binders)

In this study, a set of three different fly ashes and one ordinary Portland cement was used.

Table 14 shows the sources of these materials, and Table 15 shows their chemical composition.

Table 14: Sources of binders

ID	Material	Source
OPC	Cement Type I/II	Lafarge, Davenport, IA, USA
FA1	Class C Fly Ash	Boral Advanced Technologies Inc. USA
FA2	Class F Fly Ash	Cumberland Fossil Plant (CFP), TVA
FA3	Class F Fly Ash	John Savier Plant (JSP), TVA
Int-Si	Inert Silicon Dioxide	Sigma-Aldrich, USA

Table 15: Chemical Composition of Binders

Compound (%)	Cement	FA1	FA2	FA3
SiO₂	20.2	29.2	46.0	53.5
Al₂O₃	4.7	17.7	17.8	25.2
Fe₂O₃	3.3	5.48	18.2	7.2
SO₃	3.3	3.41	2.59	0.32
CaO	62.9	30.1	8.40	1.46
MgO	2.7	7.65	0.95	1.43
Na₂O	-	2.16	0.59	0.49
K₂O	-	0.31	2.16	3.51

Eq. Na₂O	0.54	2.36	2.01	2.80
P₂O₅	-	0.97	0.11	0.23
TiO₂	-	1.30	0.93	1.14
SrO	-	0.59	0.03	0.11
BaO	-	1.09	0.05	0.14
LOI	1.1	0.40	1.49	4.87
Carbon	-	N/A	0.55	5.30

As can be seen from Table 14 and Table 15, the FA1 is the only Class C fly ash in the series while FA2 and FA3 are the Class F ashes. The three fly ashes were chosen based on their widely different calcium oxide content in order to do a representative study of all fly ashes which can be potential SCMs.

3.2 Supplementary Experiments on Fly Ashes

3.2.1 Chemical and Physical Properties

3.2.1.1 XRF: X-Ray Fluorescence tests were performed for cement and fly ashes a PANalytical PW2404 X-ray fluorescence spectrometer. Chemical compounds of the tested materials were obtained and presented on an oven dry basis in the form of elemental oxides. Loss of ignition (LOI) and moisture content (MC) of the tested materials were also found from the tests. The results are already shown in Table 14.

3.2.1.2 XRD: X-Ray Diffraction tests were conducted for fly ashes using a Siemens D 500 diffractometer with Cu tube operated at 45 kV and 30 mA. Mineral phases of the tested materials were identified from the test results. The results will be shared in the results section.

3.2.1.4 AAS: Atomic absorption spectrometry was used to analyze slurries made of fly ash and OPC to measure the Ca^{2+} ion concentration. The API value [20] was defined on the basis of measuring the free calcium ion concentration in the OPC slurry and comparing it to the slurries having OPC and fly ash.

3.2.1.3 #325 Sieve: Sieve #325 wash tests were also performed for all cementitious materials used in this project according to ASTM C430.

3.2.2 Calorimetry and Compressive Strength

The mortars comprising 50% replacement of OPC with three different fly ashes were prepared according to ASTM C305. Their heat of hydration up to 25 hours was recorded in a 8 channel semi-isothermal calorimeter set at a reference temperature of 20° C. Then 2"x2"x2" mortar cubes were cast, and cured at 23±2° C and ≥95% RH in a curing room for 7, 28, 56, and 90 days to be tested for their compressive strength as per ASTM C109. A consistent sand-to-binder ratio of 2.75 and water-to-binder ratio of 0.45 was adopted in all mixes. Table 16 shows the four mixes prepared.

Table 16: Mix proportions of mortars

No	Mix ID	OPC	FA1	FA2	FA3
1	100%OPC	100%	-	-	-
2	50%FA1+50%OPC	50%	50%	-	-
3	50%FA2+50%OPC	50%	-	50%	-
4	50%FA3+50%OPC	50%	-	-	50%

3.3 Establishment of Raman Testing Configuration and Parameters

The configuration and parameters of Raman testing was established after a series of testing and determining which configuration optimized the data for the samples under consideration.

3.3.1 Possible Variations in Instrument Configuration

- a) Laser Power was varied from 10%, 50%, 100% of 25 mW
- b) Magnification was varied between 5x, 20x, and 50x objectives as these change the size of the laser spot incident on the sample.
- c) Accumulations on a given sample location were done to see after how many accumulations a good signal to noise (S/N) ratio was obtained. (1 to n)
- d) Exposure time of the detector to the Raman scattered photons was varied to find the optimum time to get the maximum S/N and minimum fluorescence. (10 sec to n sec)
- e) Excitation wavelength was fixed in this study to 488 nm based on the literature review, which suggested that for weak scatterers high frequency wavelengths were better.

3.3.2. Possible Variations in Sample Preparation

- a) Sample storage was compared in terms of inverted or upright placement.
- b) Effect of thin films/sheets/coverings on the sample surface (to avoid carbonations) was studied.
- c) Air exposed sample: These results are for the samples that were exposed to air during the course of study.

3.3.3. Methodology of Data Collection

- a) Fixed point/area data collection methodology is described (which eventually lead to carbonation, surface drying).
- b) Mapping an Area: Introduction to mapping acquisitions is done. Analysis included shifting from 4 point to 9 point to 49 point analysis.

3.3.4. Analysis Techniques

- a) Multi spectra averaging
- b) Effect of smoothening
- c) Effect of Normalization
- d) Effect of Base line Corrections

3.5. Dry Analysis (1 OPC & 3 FA's)

3.5.2. Bulk levels scans with 5x (200-1200 cm^{-1}) (25 locations)

1 OPC and 3 fly ashes were each analyzed in their raw, powder form with 5x objective magnification, within the 200-1200 cm^{-1} range at 25 different locations.

3.6. Wet Analysis (5 pastes) (0-90 days)

For the wet analysis, five different pastes were prepared with mix proportions as shown in Table 17. The pastes having 50% replacement of OPC with fly ashes or silica had their dry ingredients first pre-mixed in the dry form prior to wet mixing. The pastes were hand mixed for 1 minute in a bowl and the paste was transferred to different sample holders. Each sample holder was to be tested at a given age and then discarded.

Table 17: Pastes for Raman wet analysis

No.	Mix ID	OPC	FA1	FA2	FA3	SiO ₂
1	OPC	100%	-	-	-	-
2	FA1	50%	50%	-	-	-
3	FA2	50%	-	50%	-	-
4	FA3	50%	-	-	50%	-
5	Int-Si	50%	-	-	-	50%

3.6.1. Qualitative Evaluation of Developing Hydration Products (200-1200 cm^{-1}) (9 locations)

All five types of pastes were prepared for this study and the paste was stored in 11 different sample holders (XRF sample storage cups), all of them were sealed air tight to avoid any carbonation attack.

3.6.2. Evolution of Sulfates at Low Range Wavenumbers (950-1050 cm^{-1}) (49 locations)

Only four pastes were focused upon in this study, as Int-Si paste was not included.

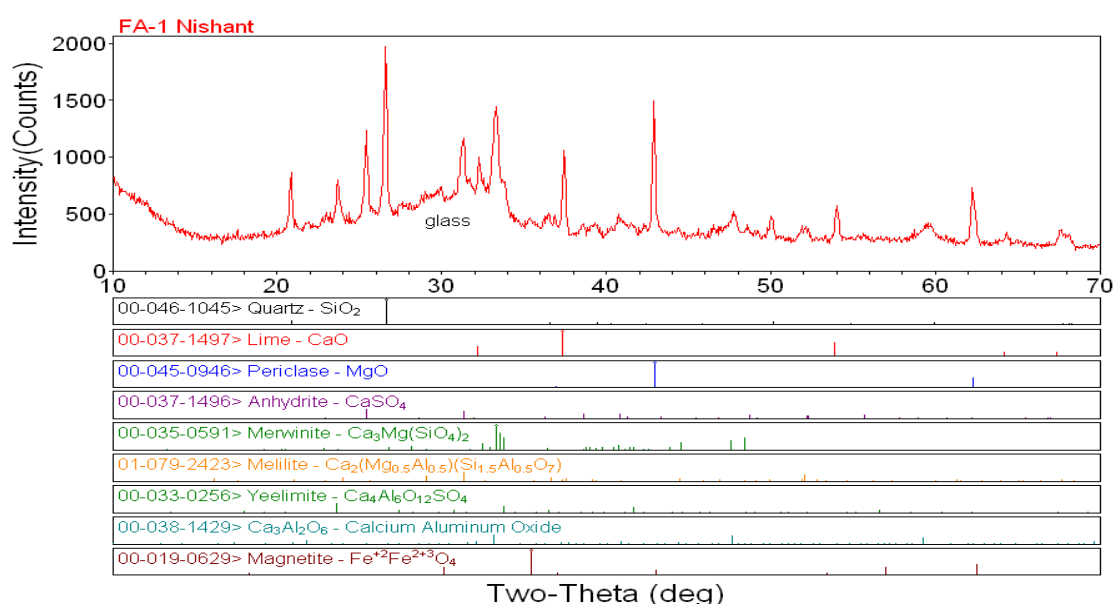
3.6.3. Evolution of Portlandite at High Range Wavenumbers (3600-3700 cm^{-1}) (49 locations)

The pastes used for evolution of sulfates were also employed to study the evolution of portlandite at high range wavenumbers.

CHAPTER 4: RESULTS, ANALYSIS, AND DISCUSSION

4.1. Supplementary Experiments on Fly Ashes

Figure 35 shows XRD of FA1, which is the Class C fly ash having the highest amount of CaO in it based on the XRF results (Figure 38). Apart from Quartz, Magnetite, and Periclase, it can be easily seen that, a lot of calcium based phases are present in this fly ash.



Iowa State University

Figure 35: XRD of FA1

Figure 36 and Figure 37 show the XRD patterns for the other two fly ashes (FA2 and FA3, respectively). Apart from the expected mineral phases occurring in the fly ashes, the interesting observation to make here is the presence of calcium based mineral phases is decreasing while moving down from FA1 to FA3. This correlates well with the lowest calcium oxide percentage present in FA3 (Figure 38). It also should be noted that FA1 has a calcium aluminate type glass while FA2 and FA3 have a calcium silicate type glass due to difference in the centroid of the glass hump. This suggests that FA1 has a reactive aluminate phase in it which might play a significant role in evolution of sulfo-aluminates.

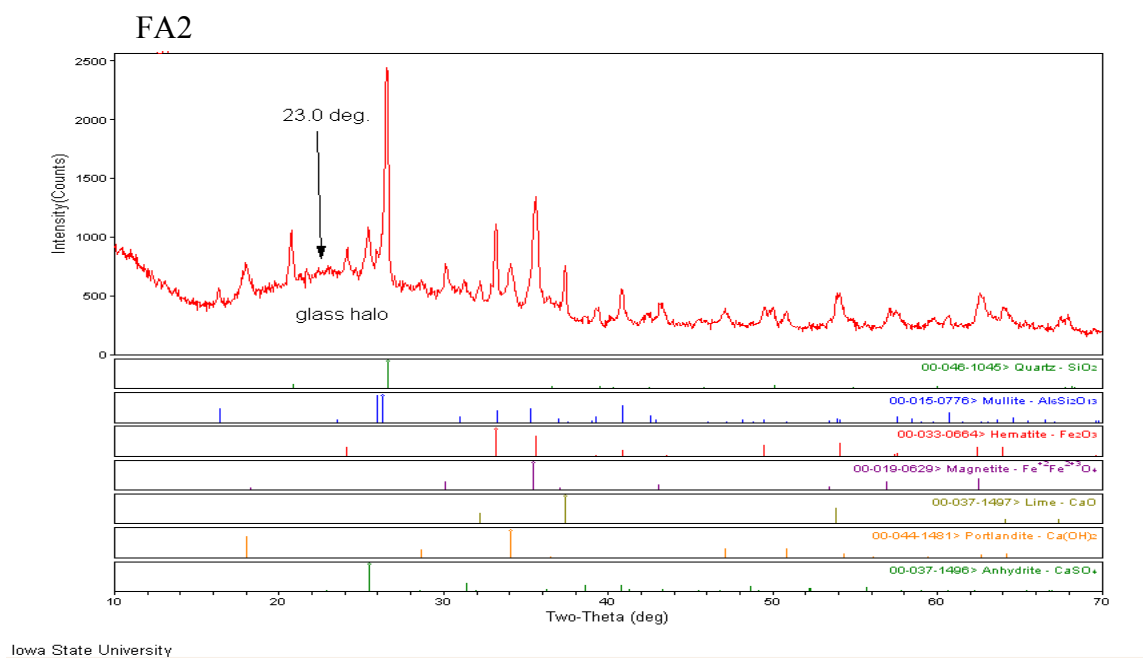


Figure 36: XRD of FA2

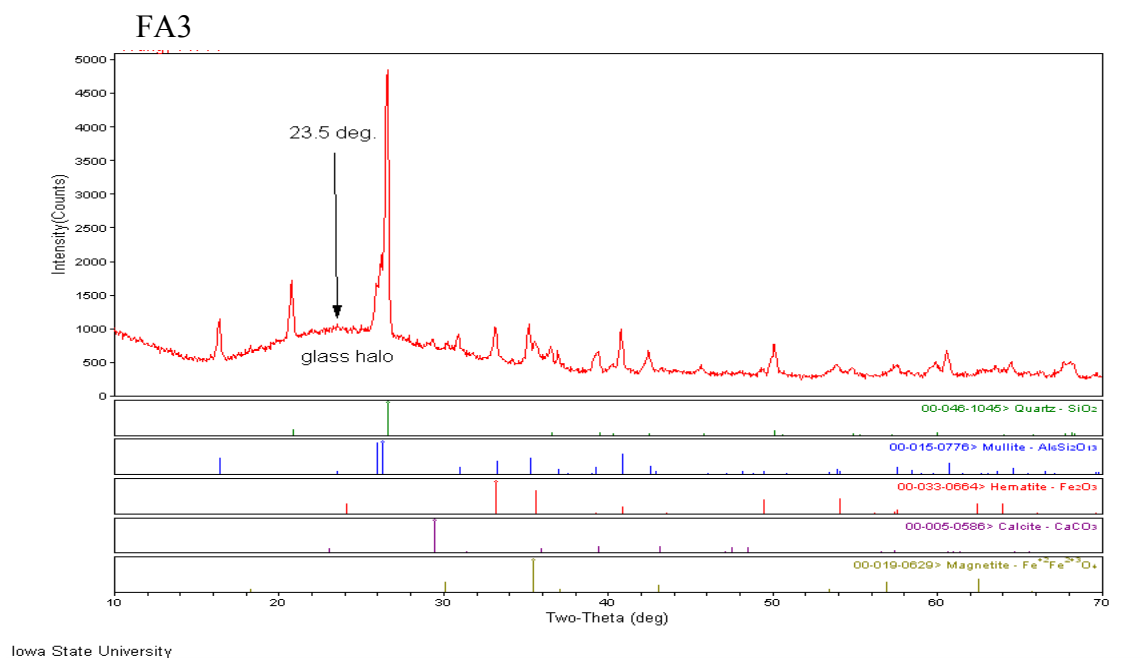


Figure 37: XRD of FA3

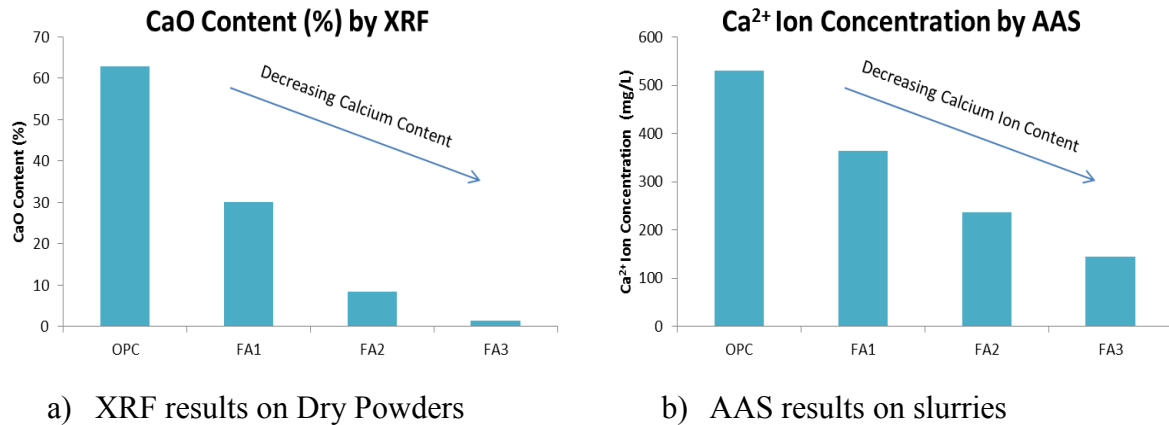


Figure 38: Variation in presence of Calcium in OPC and Fly Ashes

Figure 38 shows the results from XRF and AAS. As expected for a Class C fly ash there is a higher calcium content both in the dry form as well as the pore solution. The calcium contents are followed by FA2, and FA3 in the same pattern.

Figure 39 shows the isothermal calorimetry data for the different mortar mixes prepared using the given fly ashes. It is interesting to see in the case of FA1 which is a Class C fly ash, there is a secondary peak of heat generation at 20 hours which may be due to the formation of ettringite. Other than that, the area under the curves of the three fly ashes is calculated to represent the cumulative heat generated.

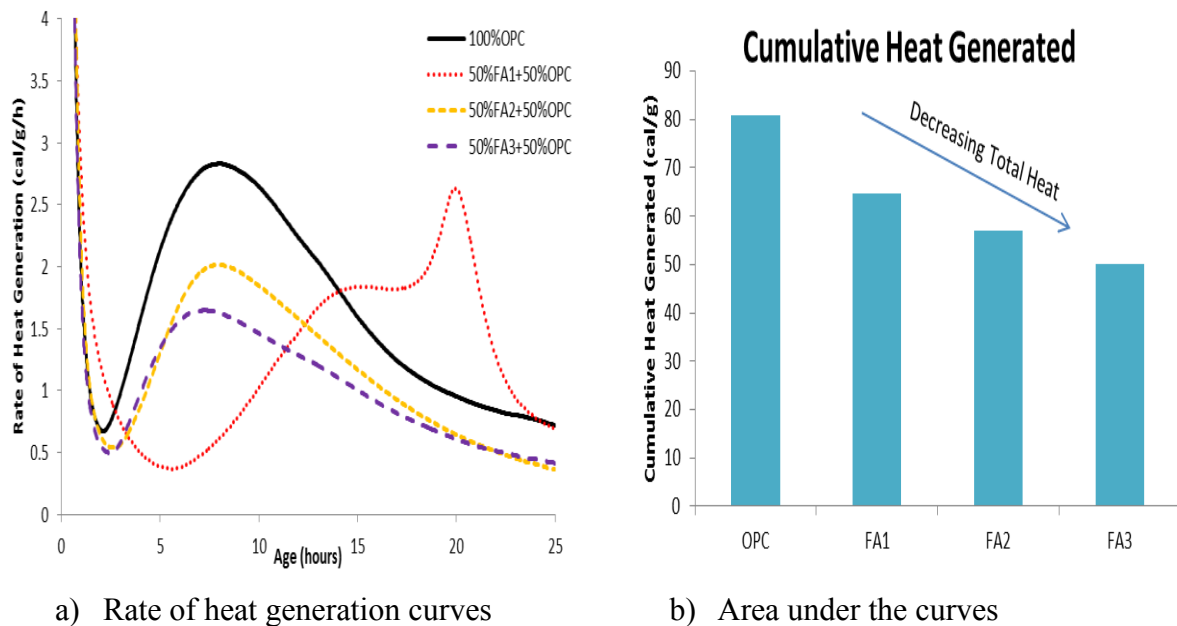


Figure 39: Calorimetric data of mortars

When compared, this shows that FA1 mortar releases the most amount of heat, followed by FA2, with FA3 mortar generating the least amount of heat. This suggests that the hydration process in the mortar containing FA1 is more intense than FA2 and FA3. Figure 40 shows the compressive strength data of the mortars made with these fly ashes, and somewhat similar trends have been obtained. The mortar containing 100% ordinary Portland cement has obviously the highest strengths achieved at all ages, followed by the mortars containing 50% fly ash replacement. Roughly, FA1 is found to be more reactive than FA2, and FA2 is more reactive than FA3 based on the observed trends.

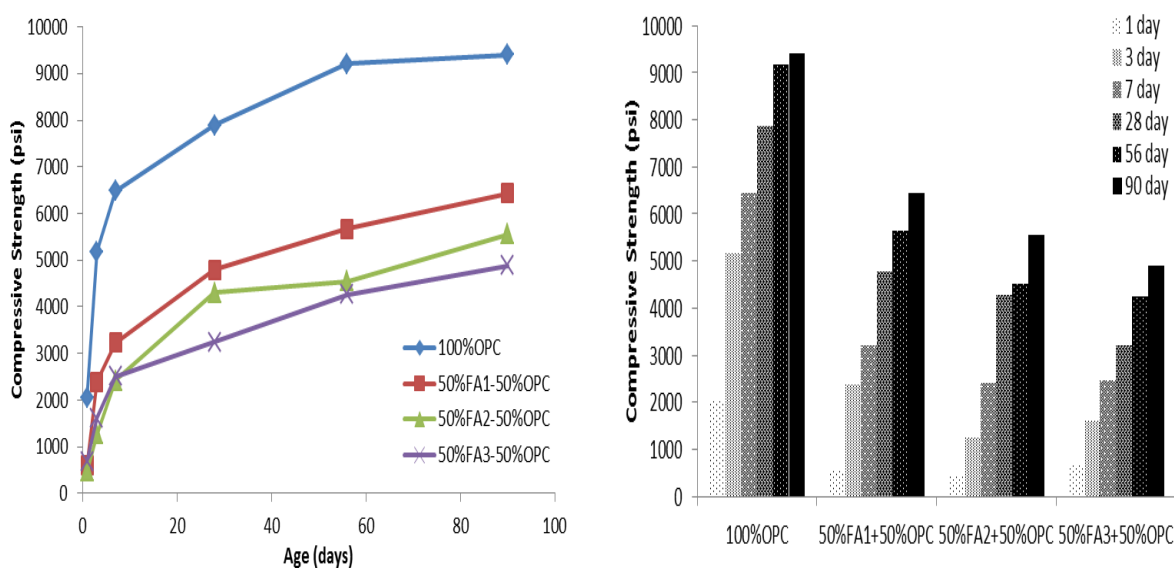


Figure 40: Compressive strength data of mortars

4.2 Establishment of Raman Testing Configuration and Parameters

Figure 41 shows a typical setup of a sample plate placed under the microprobe, ready to be imaged and analyzed by Raman spectroscopy. This section deals with several instrumental settings and choices that were made to collect optimum quality data. A set configuration was

given preference over all other possible configurations and the justification behind that choice is presented in this section.



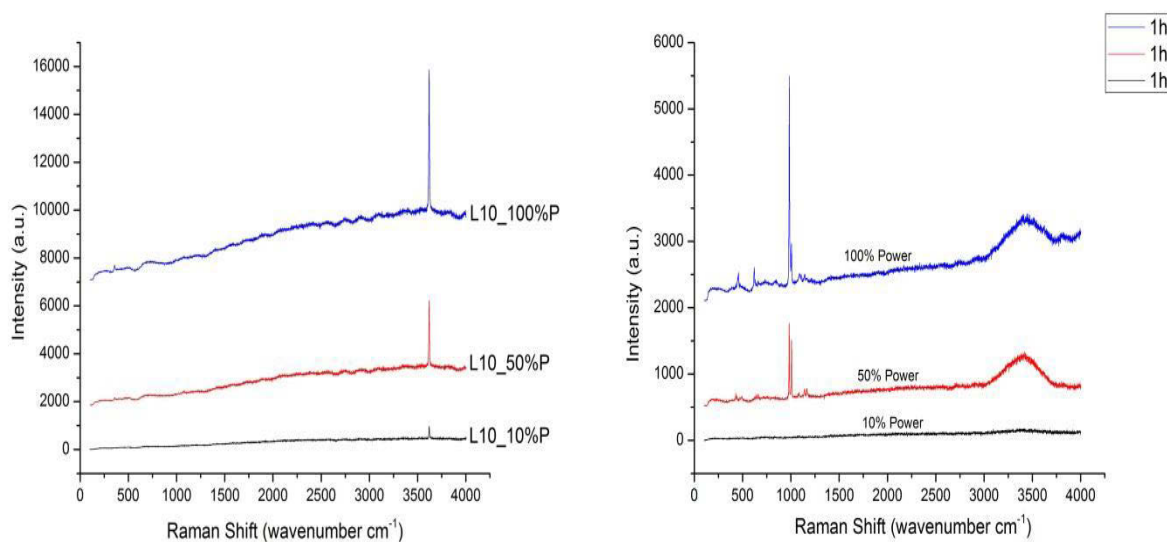
Figure 41: Typical setup of sample stored under the Raman microprobe

4.2.1 Possible Variations in Instrument Configuration

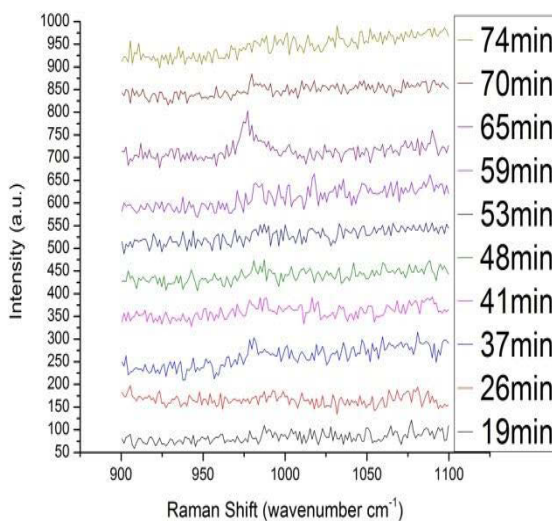
a) Laser Power was varied from 10%, 50%, 100%. Figure 42 shows the effect of laser power on aged paste showing the calcium hydroxide peak at 3619 cm^{-1} . As expected increasing power increases the incident intensity on the sample, resulting in more photons subjected to the Raman effect.

The visual effect of the laser on the sample was also analyzed to see if the laser caused any physical damage to the sample's wet surface. Figure 43 shows the apparent surface interaction effect of the laser on the sample. It seems that laser is causing some kind of damage to the surface based on this figure. However, a more detailed study of this effect showed the hot laser is merely evaporating the shining, bleed water on the top surface of the sample, which results in the revelation of the dry surface beneath. If the sample is allowed to stay in its position for some time (approximately 10 minutes), the surrounding water will soon fill the dry hole dug by the laser interaction, eventually leading to a flawless surface covered by a thin film of water. This means that Raman's 488 nm laser employed in this study, especially at early ages, is completely non-destructive and effects such as sample

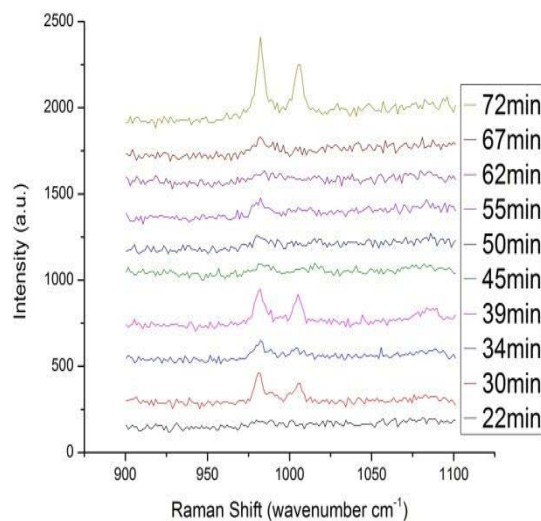
heating or burning are not expected to be a major concern. Figure 44 shows this evidence for the non-destructive nature of the employed laser in this study.



a) Different laser powers on same location of a sample



b) 50% Power on sample



c) 100% Power on similar sample

Figure 42: Effect of laser power on S/N

It must also be noted in Figure 44 that once the samples are hardened, there is not even a visual effect on the sample surfaces from the interaction of the laser. Repeated sampling at the same location in a sample did not result in any damaging effect in the spectra.

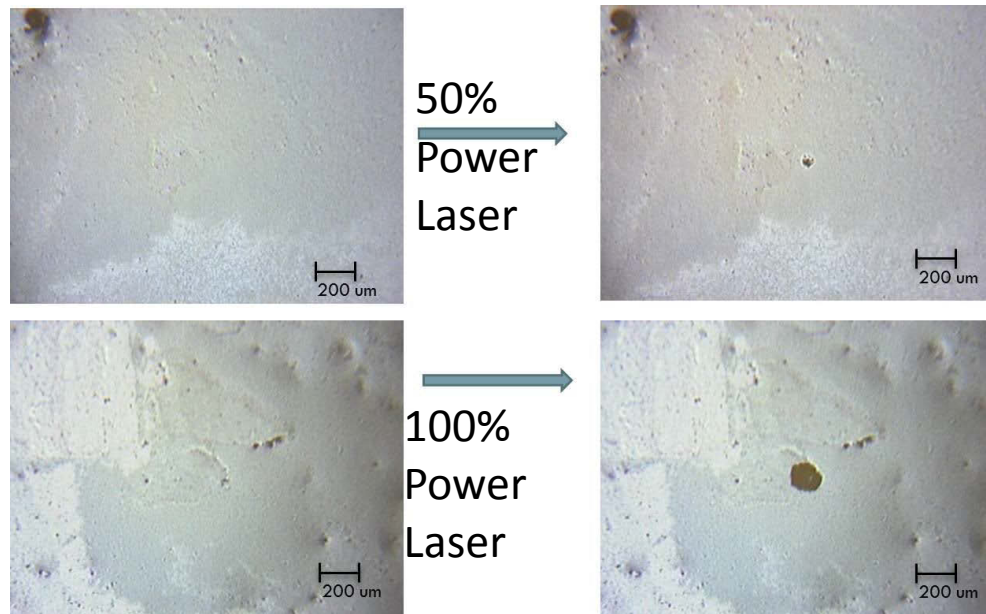


Figure 43: Effect of laser on sample surface as seen by the microscope on a 1 hour old OPC paste.

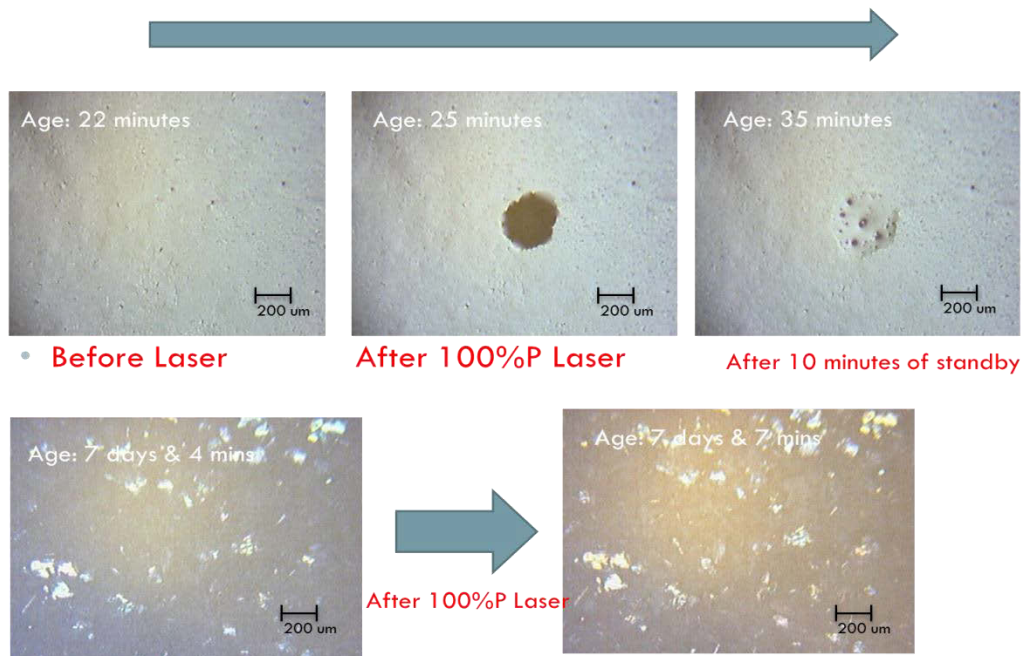


Figure 44: The non-destructive nature of the 488 nm laser on cementitious samples

b) Magnification was varied between 5x, 20x, and 50x objectives as these change the size of the laser spot incident on the sample. As is seen in Figure 45, while increasing the magnification objective results in images at the macro-scale, it must be noted that the images obtained at the 50x magnification are usually not focused well. This is because the surface is very rough as no sample preparation was done.

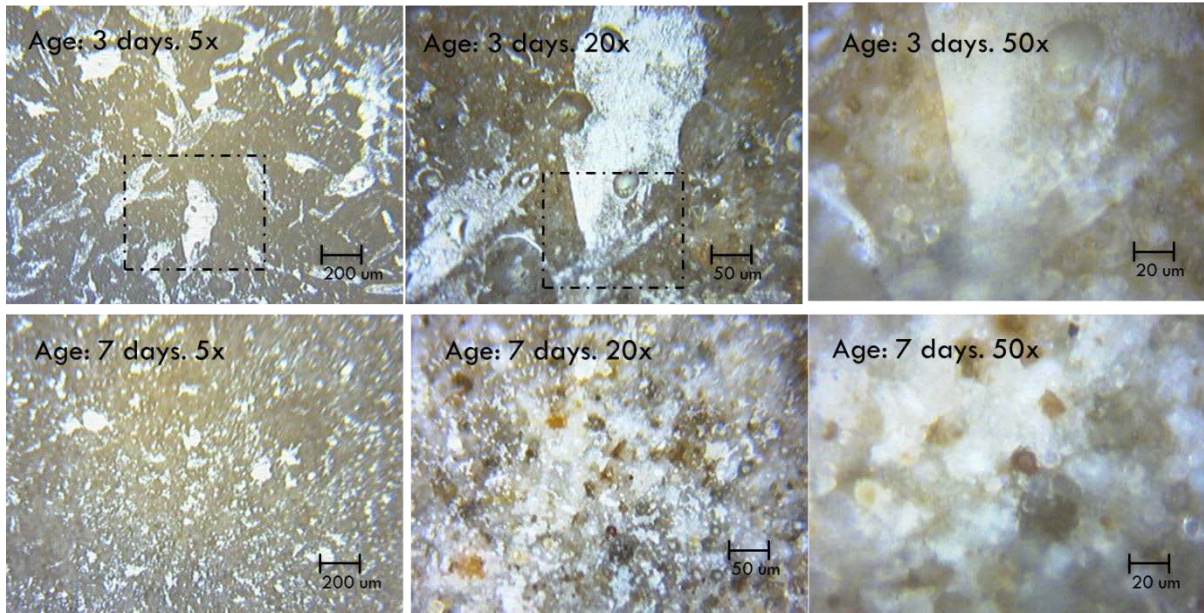


Figure 45: Effect of Magnification on the microscopic images of hydrated OPC samples

In order to decide which magnification level the analysis should be conducted, several samples at same locations were analyzed from different objectives to see which objective gives the maximum S/N. Figure 46 shows the attempt to determine the optimum laser spot size/magnification level and it is clear there is no definite answer to this problem. While one may expect a linear trend between S/N and decreasing spot size (increasing magnification level) due to increased focus on laser energy, such a trend was not observed. This can be explained by the microscale physical and chemical heterogeneity of the OPC hydrated pastes studied at different locations. The crystal orientation, grain surface, distribution of the hydrate, all of these can vary with changing area of the laser spot incident on the sample.

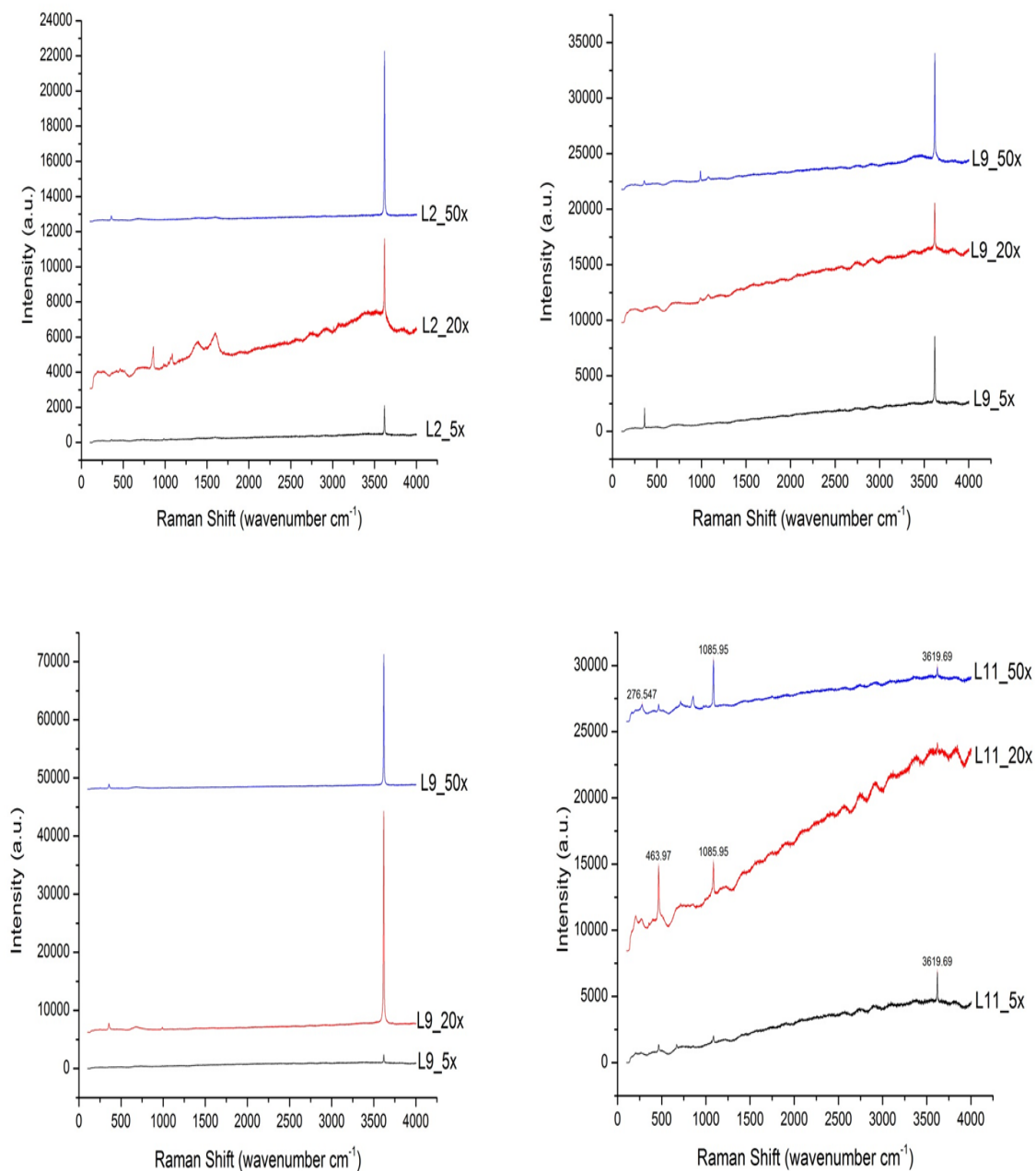


Figure 46: Effect of magnification/laser spot on S/N (L means the location of the hydrated OPC paste)

Hence, finally a laser spot size of 5x was arbitrarily chosen, considering the fact that it is able to map the area of a circle with a diameter of $100\mu\text{m}$ (=area of spot size incident on the sample surface).

c) Accumulations on a given sample location were done to see after how many accumulations a good signal to noise (S/N) ratio was obtained. The number of accumulations was limited to 1 at each sample location as instead of increasing accumulations at a single point, more points in a sample were considered to be analyzed.

d) Exposure time of the detector to the Raman scattered photons was varied to find the optimum time to get the maximum S/N and minimum fluorescence.

e) Excitation wavelength was fixed in this study to 488 nm based on the literature review, which suggested that for weak scatterers high frequency wavelengths were better.

4.2.2. Possible Variations in Sample Preparation & Storage

The samples were prepared by hand mixing for at least one minute in a glass bowl and once a visually uniform paste of cement, fly ash, and water was obtained (free from lumps) at water-to-binder ratio of 0.45, it was immediately transferred to N number of sample cups (where N = # of ages at which the sample is to be studied). Figure 47 shows the typical sample preparation setup employed in this study.



a) Before mixing

b) After mixing

Figure 47: Sample preparation

Figure 48 shows the sample storage method employed in this study. The samples were stored and kept from air to avoid the carbonation attack. Each sample was stored in a dark, humid chamber and it was opened only the day it was to be tested.

The following sub-sections will explain why this particular method for sample preparation and storage was preferred.



Figure 48: Sample storage in sealed sample cups

a) Sample storage was compared in terms of inverted or upright placement. The samples were chosen to be stored upright instead of inverted. While inverted storage in a sample cup, did result in a smooth surface at the top, it may induce a wall effect on the reacting clinker grains and hence the hydration products formed on the surface might not be represented of those formed inside the bulk matrix.

Figure 49 shows a typical upright sample storage method which was selected in this study. However, it must be noted that this type of storage eventually results in condensation of water, and it escaping from the hydration process on the bottom surface of the plastic sealing film. After this Raman spectra cannot be collected by focusing through the film and the film needs to be removed before collection. And since the sample gets exposed to atmospheric

CO₂ after removing the top sealing film, a new sample has to be used at every new curing age.



Figure 49: Upright sample storage results in condensation of water bubbles on sealing plastic film

b) The effect of thin films/sheets/coverings on the sample surface (to avoid carbonations) was studied. Figure 50 shows the way sample sealing was tried by pasting a thin film on the surface of the paste. Figure 51 shows the effect of imposing such films on the surface of the samples to be studied.



Figure 50: Sample sealing involving pasting a thin film on the surface of the paste

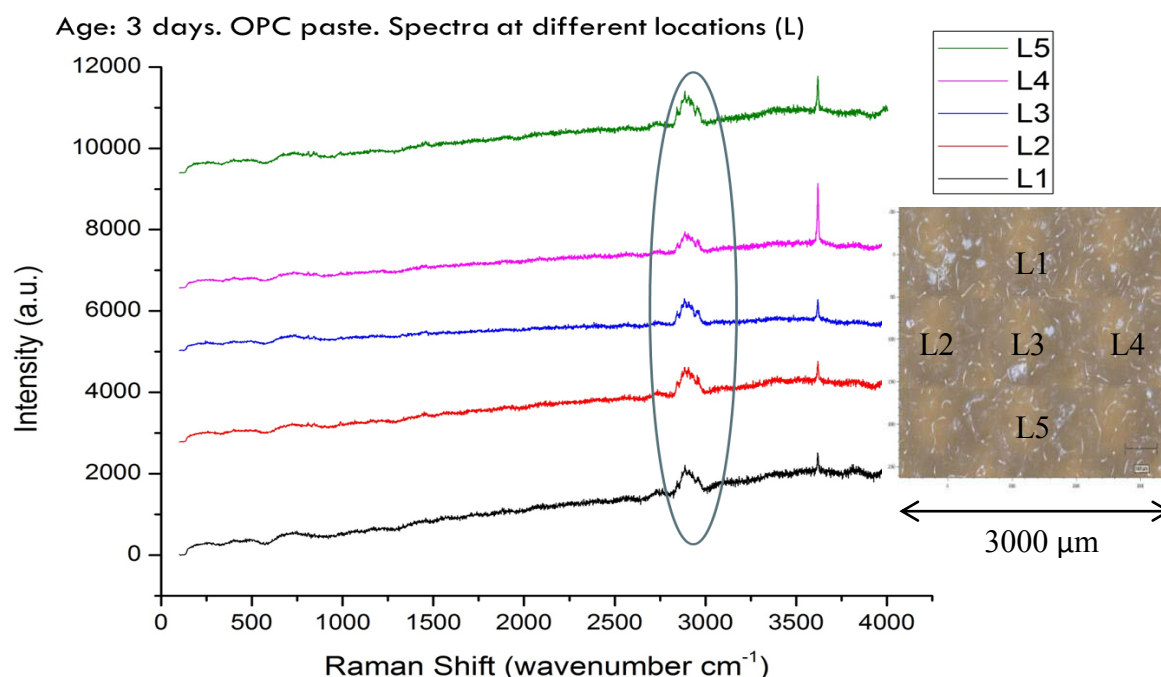


Figure 51: Effect of imposing thin film on surface. The marked circle shows the additional unexpected peaks. The optical image on right shows the various locations measured on the sample.

To verify that the humps at 2900 cm^{-1} are due to the interference caused by the thin film imposed, the films were individually analyzed by isolating them and then focusing the laser on their surface. It is interesting to see that, as shown in Figure 52, the hump near 2900 wavenumber region is from the thin films. Hence, it was decided that an air gap was to be maintained in the sample surface and the sealing film on the upright sample storage cups.

c) Air exposed sample: These results are for the samples that were exposed to air during the course of study. Exposure to air resulted in surface carbonation within less than an hour, usually within thirty to forty minutes of air exposure. Figure 53 shows the visual effect of air exposure on paste samples as it results in a dry, light surface texture as opposed to a damp, dark surface.

Figure 54 shows that from the data collected 2 hours onwards, the sample surface is covered by a layer of calcite which progressively increases in concentration over time. At 3 days, all four vibrational modes for calcite are clearly visible suggesting a strong and dominant presence of calcite on the surface. This also means that avoiding carbonation is critical if

characterization of evolving hydration products on the surface is to be done by Raman spectroscopy effectively. Thus, it was decided to avoid air exposure as much as possible, and each sample was discarded after the 20 minutes of analysis at a given age. At every new age, a new sample from the same mix was employed.

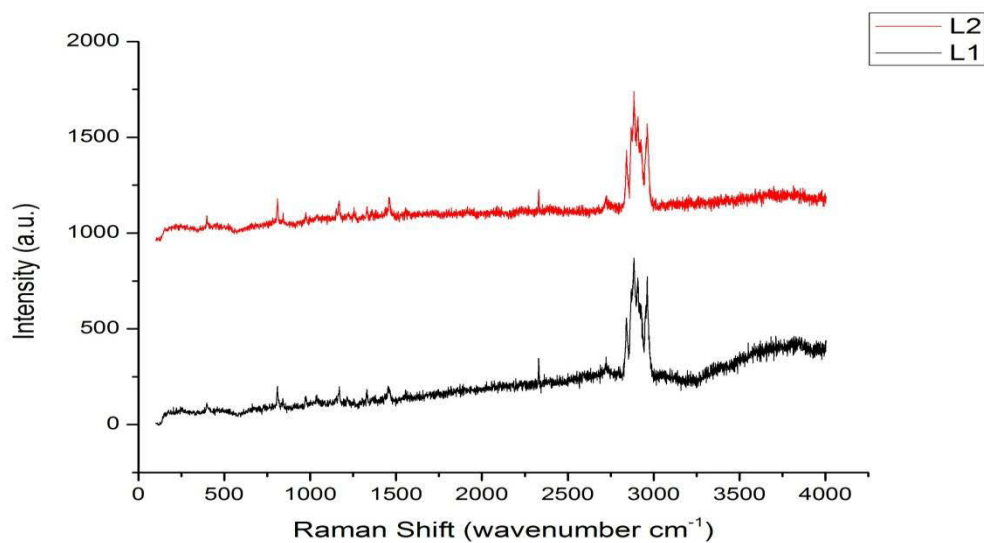


Figure 52: Raman spectra of the thin film alone

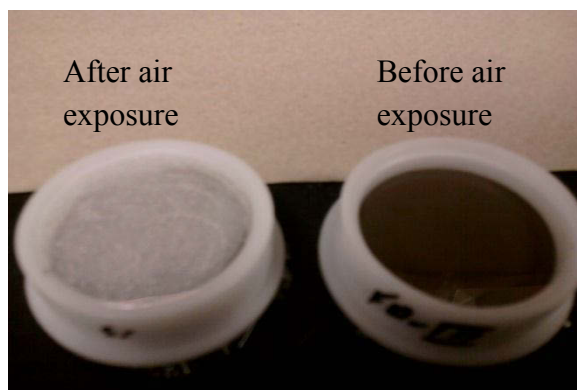


Figure 53: Effect of air exposure on fresh pastes

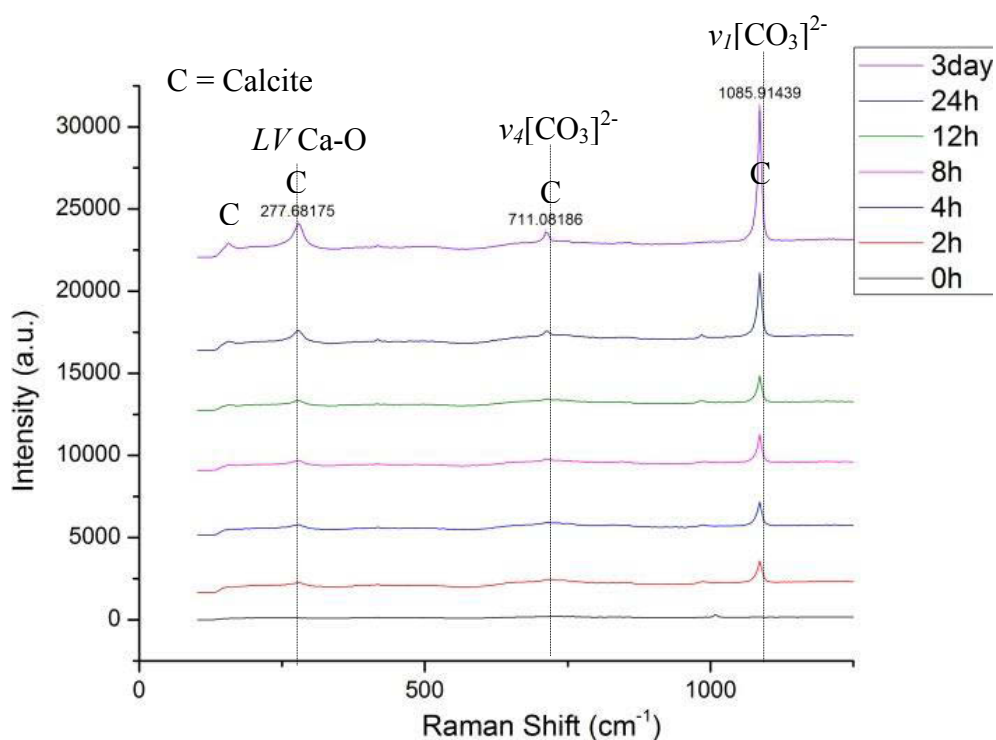
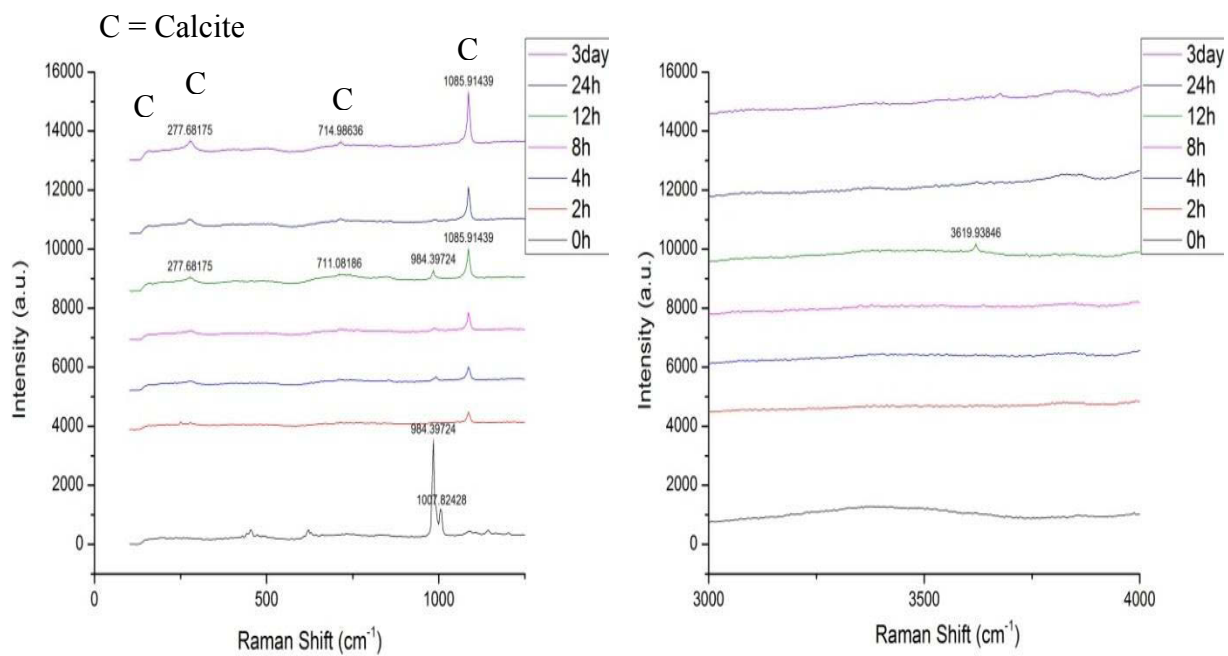


Figure 54: Raman spectra of hydration of 100% Raman spectra.

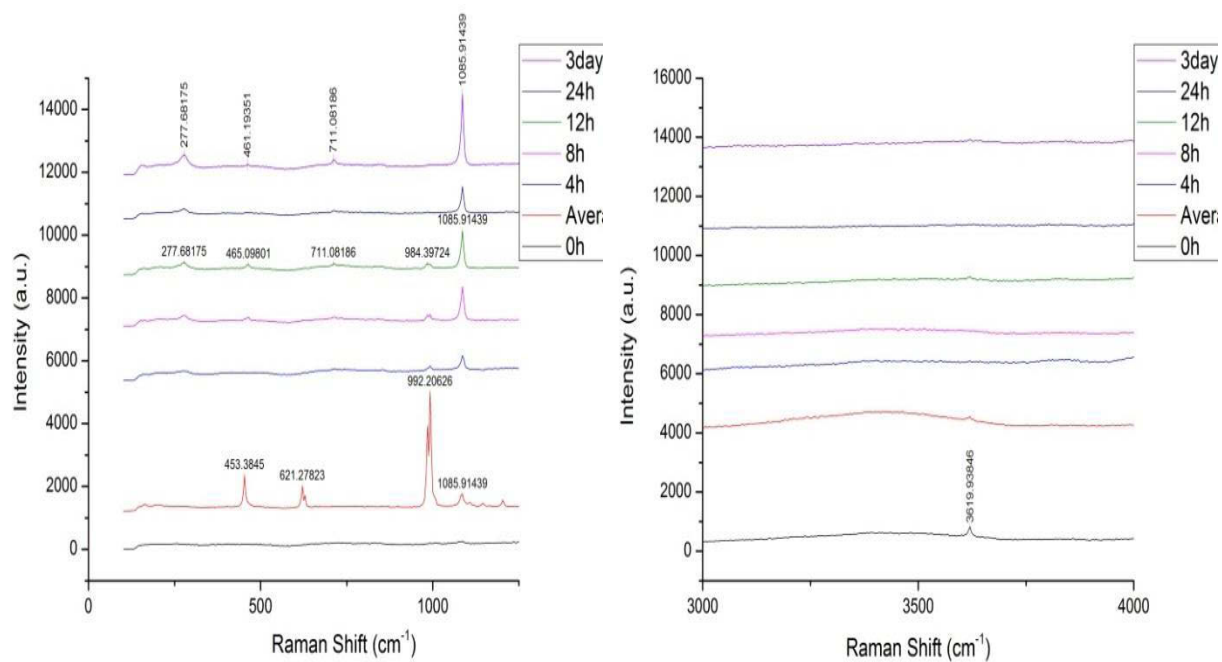
4.2.3. Methodology of Data Collection

a) Fixed point/area data collection methodology:

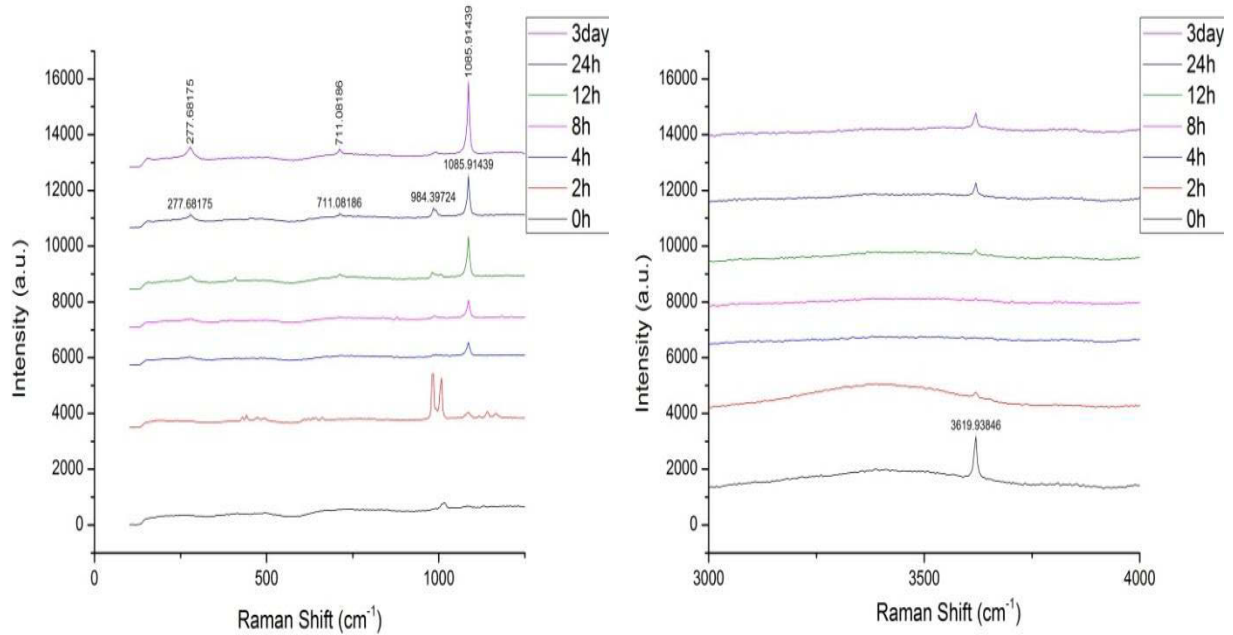
This methodology is the one that resulted in the air exposure explained in the previous section. While studying a fixed point/area may be advantageous in following the hydration process of a selected clinker grain, sample surface exposed to air is highly susceptible to carbonation. Although laser is capable of penetrating through a glass slide or thin sheet but during this study it was found, after passing through a medium the received signal had lower S/N and often more noise. Since the materials studied herein are weak Raman scatterers, adding a medium in the path of reflected inelastic photon reaching the detector makes the signal much weaker. Figure 55 shows some selected results of effect of carbonation on various mixes. It is interesting to note that calcite reduces the intensity of both CH (3619 cm^{-1}) and other possible hydration products in the lower wavenumber region of $200\text{-}1200\text{ cm}^{-1}$



1) 50%OPC+50%FAI (Class C)



2) 50%OPC+50%FAII



3) 50%OPC+50%FAIII

Figure 55: Carbonation attack on fly ash-cement pastes

(C-S-H, AFt/AFm) It will be seen later that while in covered fly ash-cement mixes, portlandite peaks grow quite rapidly and easily visible. However, in the carbonated mixes, they are barely visible.

b) Mapping an Area:

Mapping acquisitions are done in this section. Analysis included shifting from 4 point to 9 point to 49 point analysis. More points were selected for the quantitative analysis of sulfates and hydroxides. It was found that the intensity collected from each sample location was not only dependent on the concentration of the analyte but also dependent on various sample surface properties for example the orientation of the surface, roughness, etc. Hence, it was necessary to measure spectra on as many points as possible, so that a Gaussian distribution of peak intensities could be obtained.

In order to setup a mapping experiment, in the wire program, go to New>Mapping Acquisition and specify the x,y co-ordinates, type of area to be measured, kind of coverage (roster vs snake), step size, all of these can be selected based on the analysis time that is

budgeted for an experiment. Also, images can be montaged together, by snapping 9 pictures with motorized stage and then selecting the montaged area to be mapped.

The snake method was chosen for area coverage as it was found to be faster than the raster method (which involved diagonal movement of laser, from the right end of the top row to the left end of the middle row as compared to the snake movement which involved movement from the right end of top row to right end of the middle row) Figure 57 shows the wire setup for 49 point mapping.

While one would expect that mapping 49 point (duration 05:43) would take much longer than mapping 9 points (duration 05:33), the reason here both analysis take almost the same time is due to the wavenumber region that was analyzed in each study.

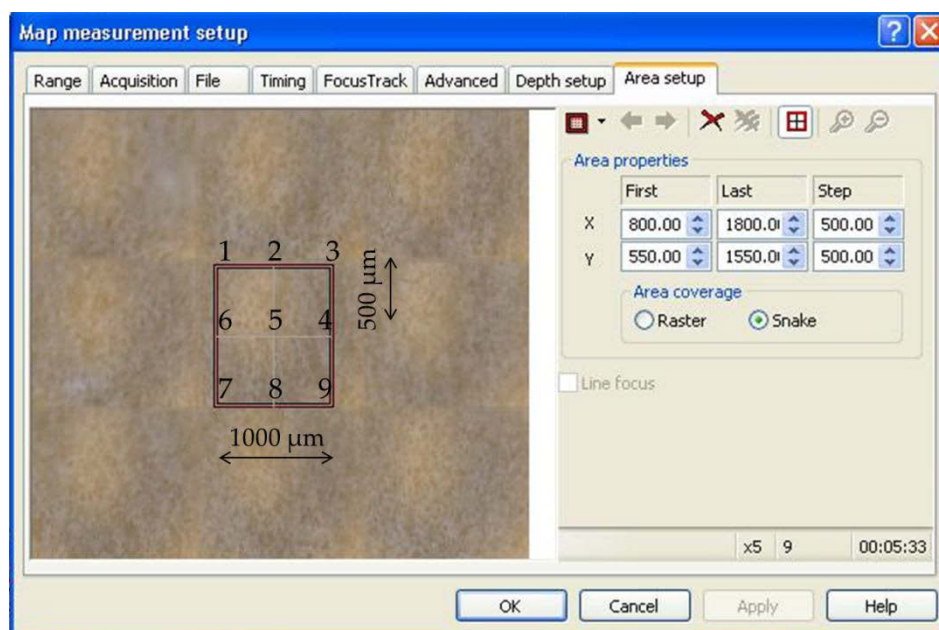


Figure 56: Wire setup for 9 point mapping

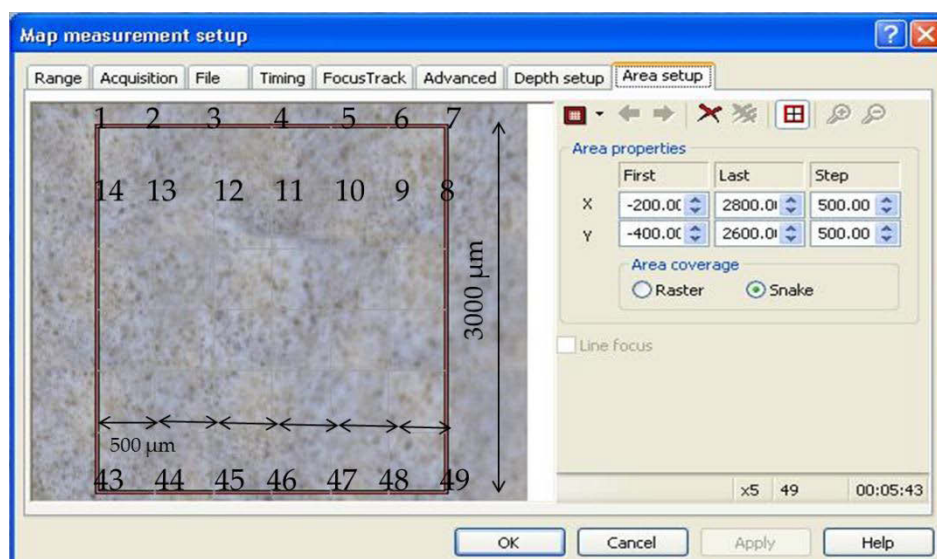


Figure 57: Wire setup for 49 point mapping

For the 9 point study, the full low range 200-1200 wavenumbers were studied for qualitative purposes, and for 49 point study narrow wavenumber range of 950-1050 (for sulfates) or 3600-3700 (for hydroxides) was taken under consideration for quantitative purposes.

Figure 58 shows a sample screenshot of the mapping analysis for 9 points. The real analysis time is often longer than the expected duration time listed during the mapping setup due to several other steps that take time every time a spectrum is collected (movement of stage, opening/closing of laser shutter, exposure to detector etc). The Wire program interface shows the collection of live spectrum along with a review of the mapping location under study.

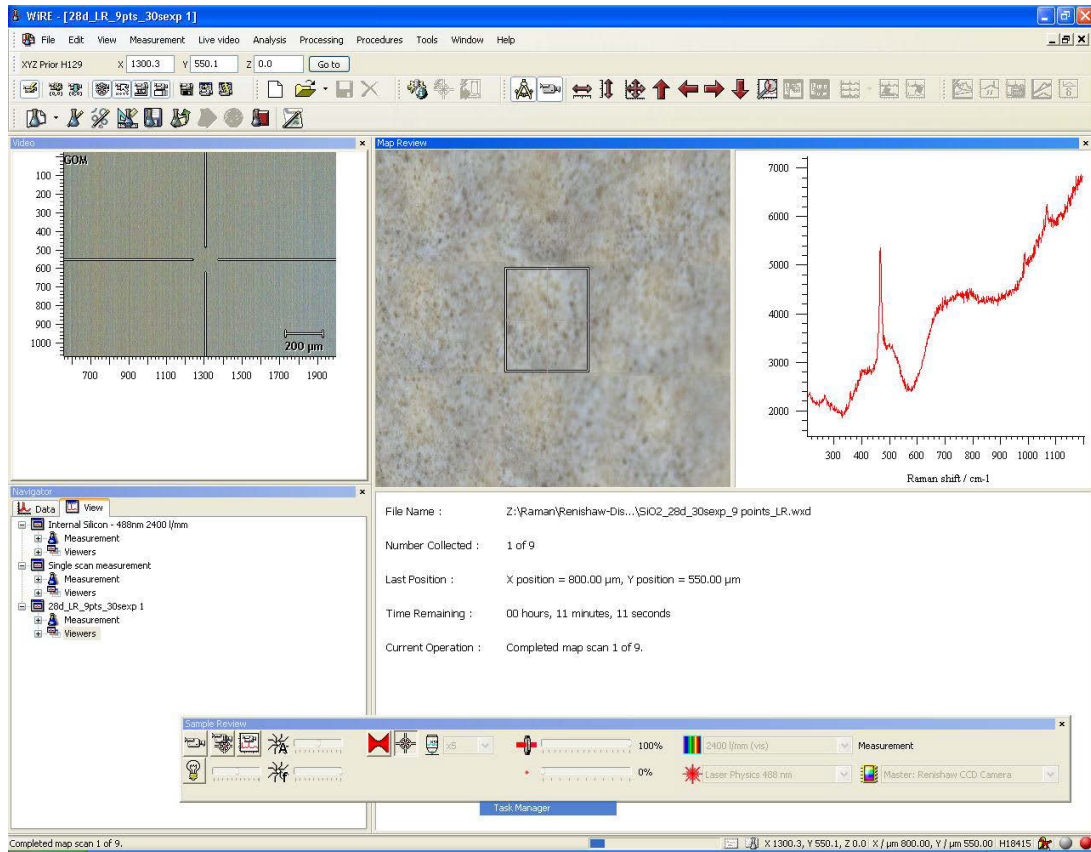


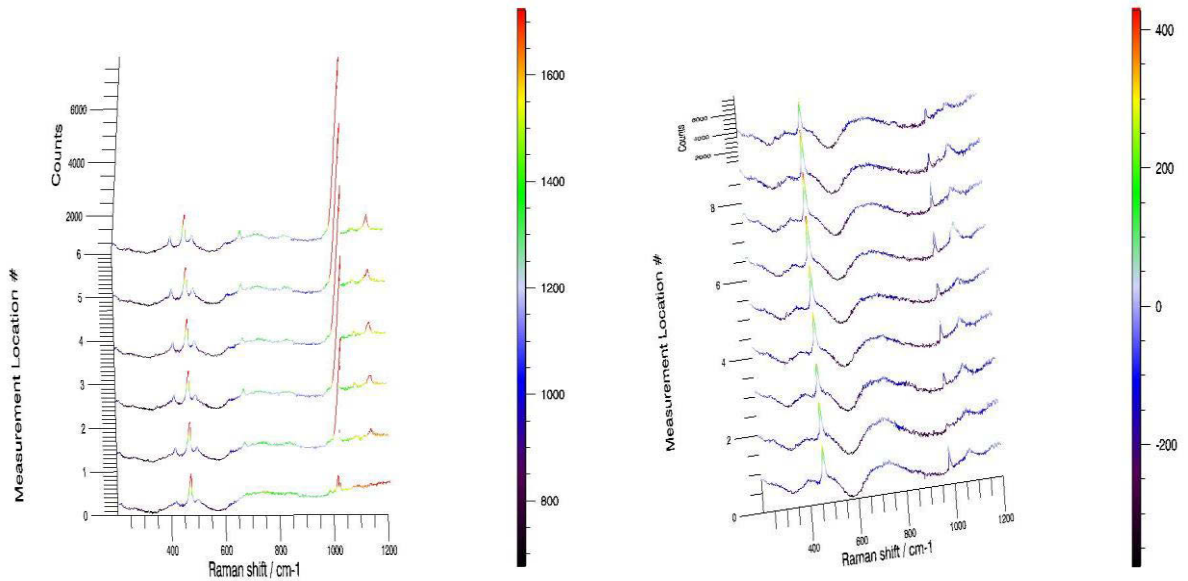
Figure 58: A sample screenshot of Wire performing mapping analysis

4.2.4. Analysis Techniques

a) Multi spectra averaging

The reproducibility of multiple spectra collected at different locations often varies and depends on the heterogeneity of the sample. And since all the samples studied in this thesis research are complex and heterogeneous, often a spectrum obtained at one location (L1) may appear entirely different from the spectrum obtained at another location (L2). However, by employing data post-processing techniques, it was found that the spectra at different locations of a given sample was more or less the same, once all the interfering background, baseline was removed, and the data was smoothened and normalized. Figure 59 shows a set

of two data showing the general reproducibility of the qualitative studies done at 200-1200 cm^{-1} .



a) SiO2_0.2h old_30s exp

b) SiO2_24hr old_30s exp

Figure 59: Average reproducibility of selected hydrating pastes (exp = exposure)

However, in the case of quantitative studies where no data processing was performed, the intensity of the peaks usually follow a normal distribution (Figure 60).

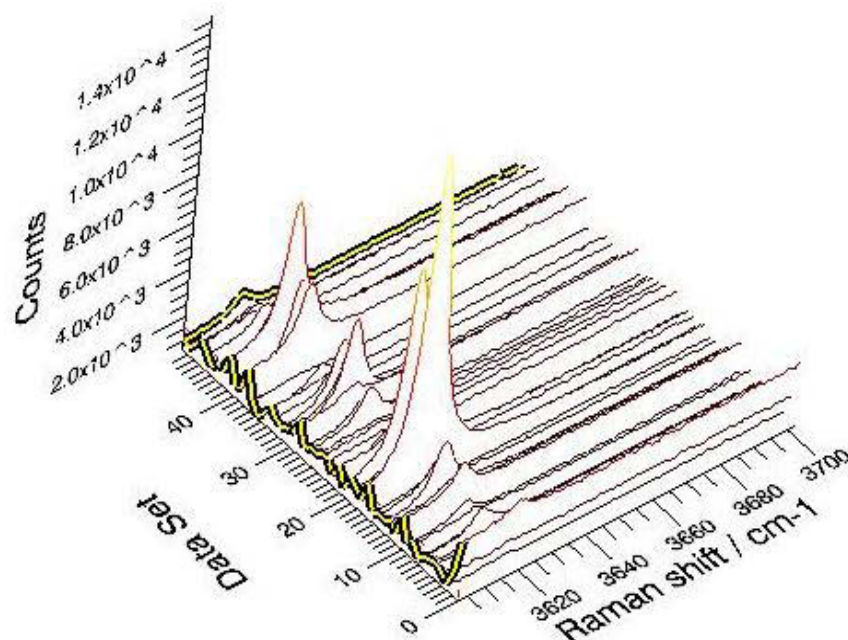


Figure 60: Distribution of CH intensities at different locations (data set 1-49 = L1-L49)

b) Effect of smoothening

The in-built smoothening function of Wire was used to smoothen out noisy data for better peak observation and presentation. Figure 61 shows a sample result from the application of the smoothening function.

OPC_Dry Powder Form

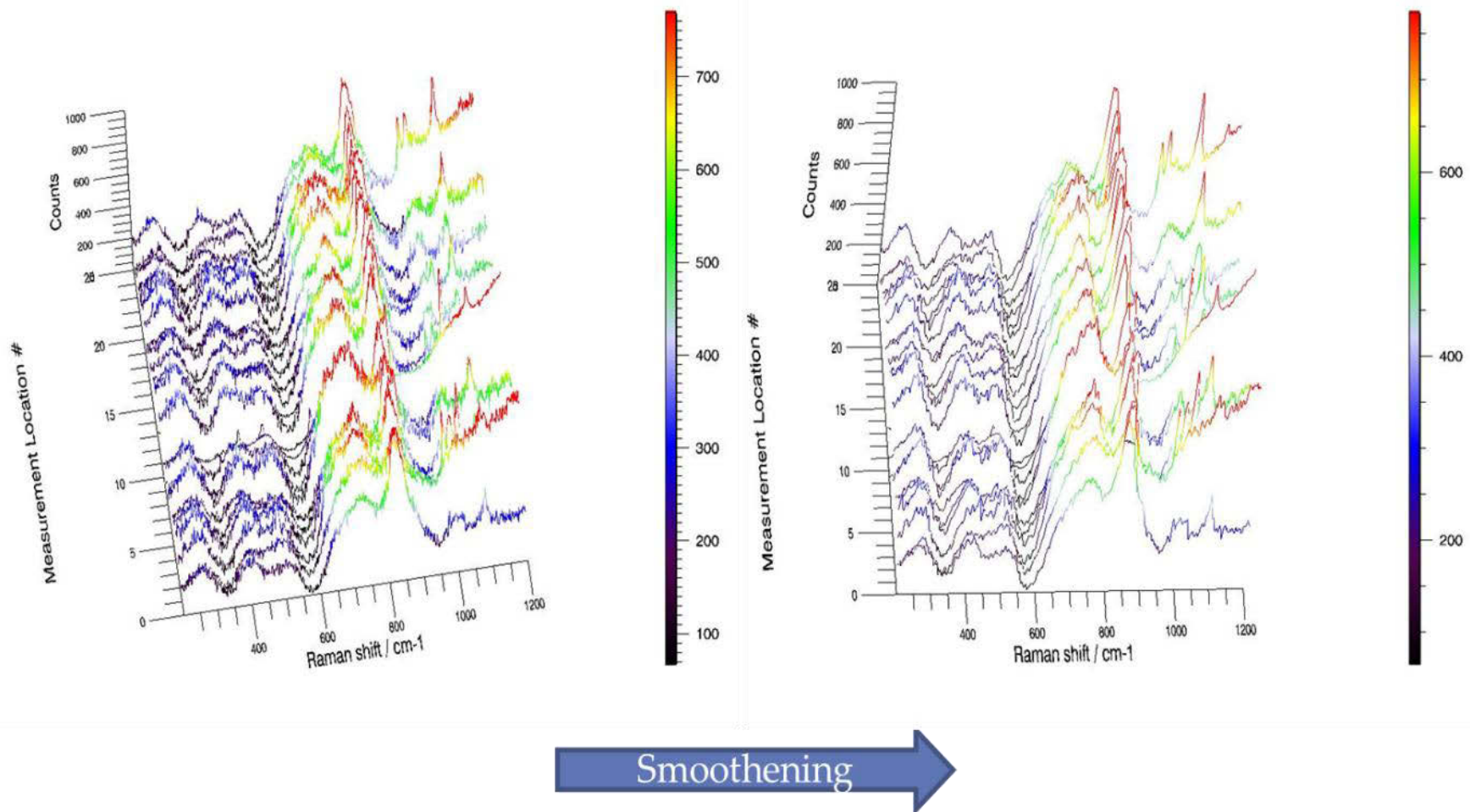


Figure 61: Application of the smoothing function

c) Effect of Normalization

Figure 62 and Figure 63 show the effect of normalization on the data. The qualitative data for characterizing the hydration products, and evolution of sulfates was normalized by the highest peak in each spectrum to a chosen intensity of 1000. The reason why each spectrum was normalized to its highest peak was to make sure to minimize unexpected background, fluorescence, and to bring all spectra to an equal scale for better comparison.

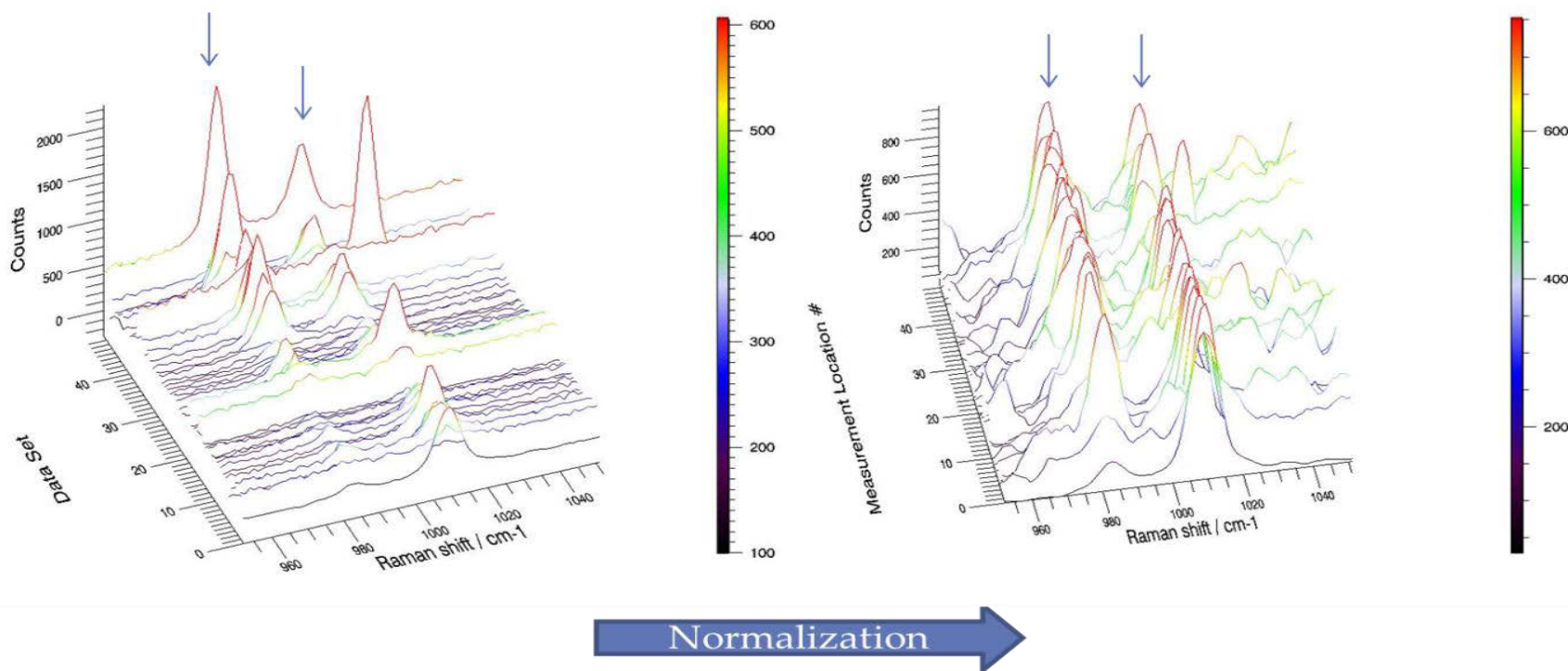
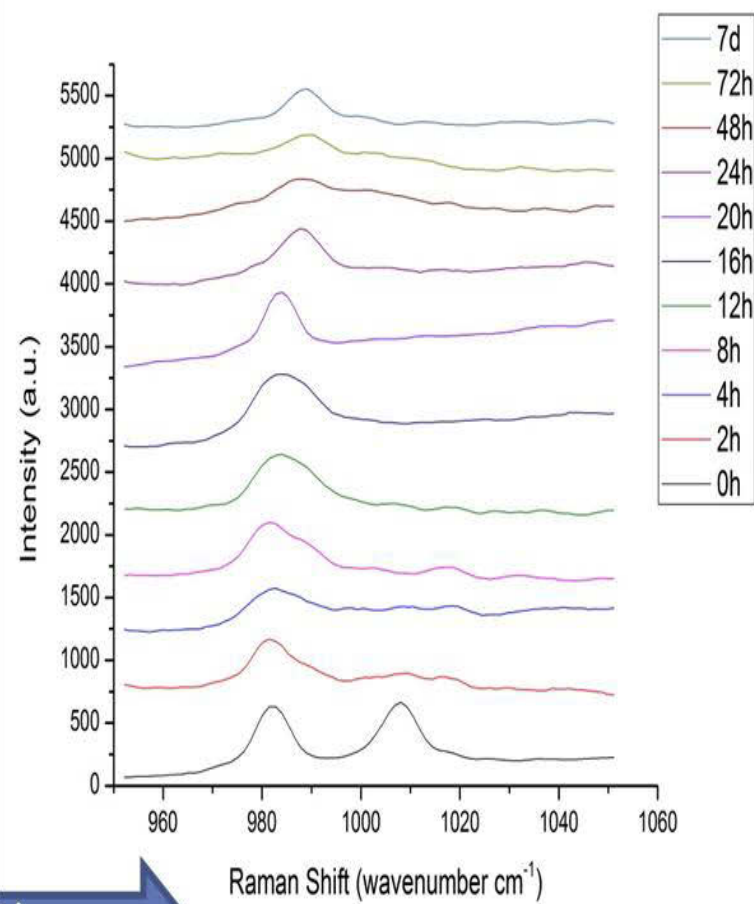
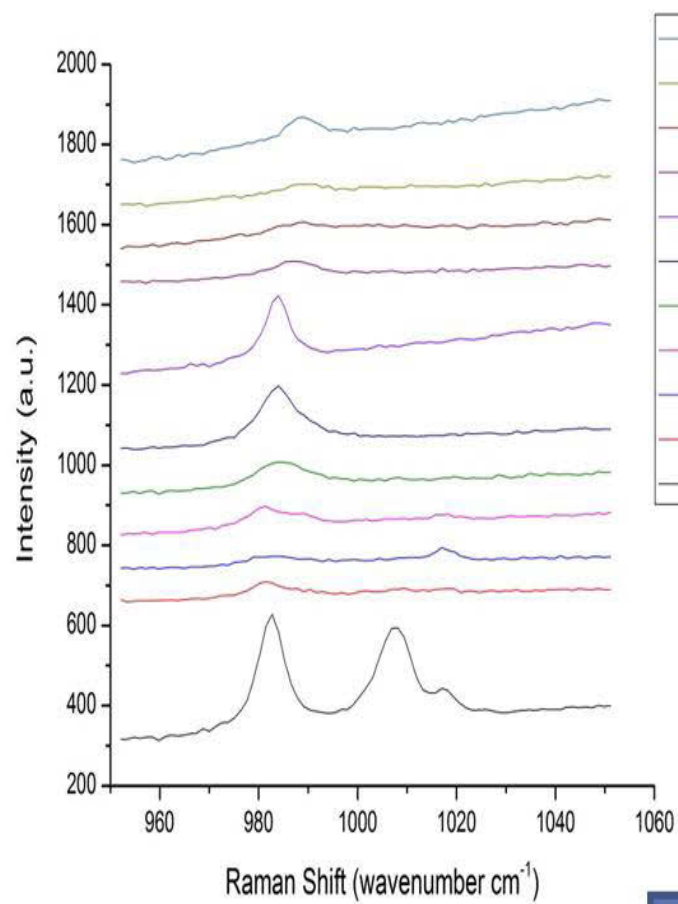


Figure 62: Normalization of 0.2h old hydrated OPC



Normalization

Figure 63: After normalizing at each age, the change in average spectra of 49 spectra

d) Effect of Base line Corrections

The base lines were corrected on the spectra after they were normalized and smoothened. The sequence of processing the data was selected to be normalization->smoothening->baseline correction. All of this processing was performed in Wire 3.1 Origin 8.6 was used to take the average of the 49 spectra and plot the averaged spectra of different ages by offsetting in a graph (Figure 64).

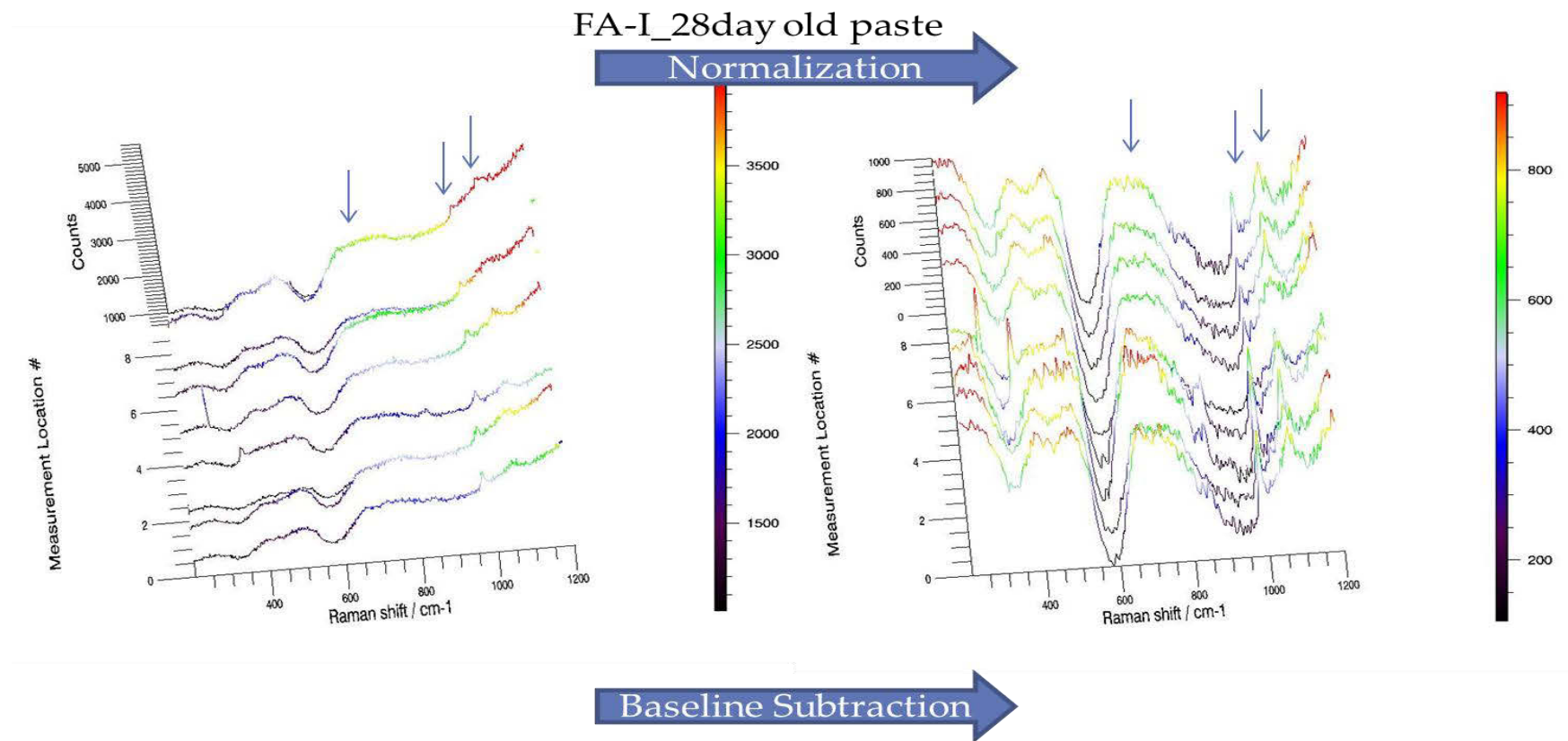


Figure 64: Effect of Normalization followed by baseline subtraction

4.2.5 Plotting Methods (Conversion of Data to Images)

4.2.5.1 Evolution of sulfates

Figure 65 shows the conversion of 3-d data of sulfate evolution study to a 2d image. The conversion process can be understood as looking at the initial 3-d data from the top. Red means high intensity and violet-blue means low intensity.

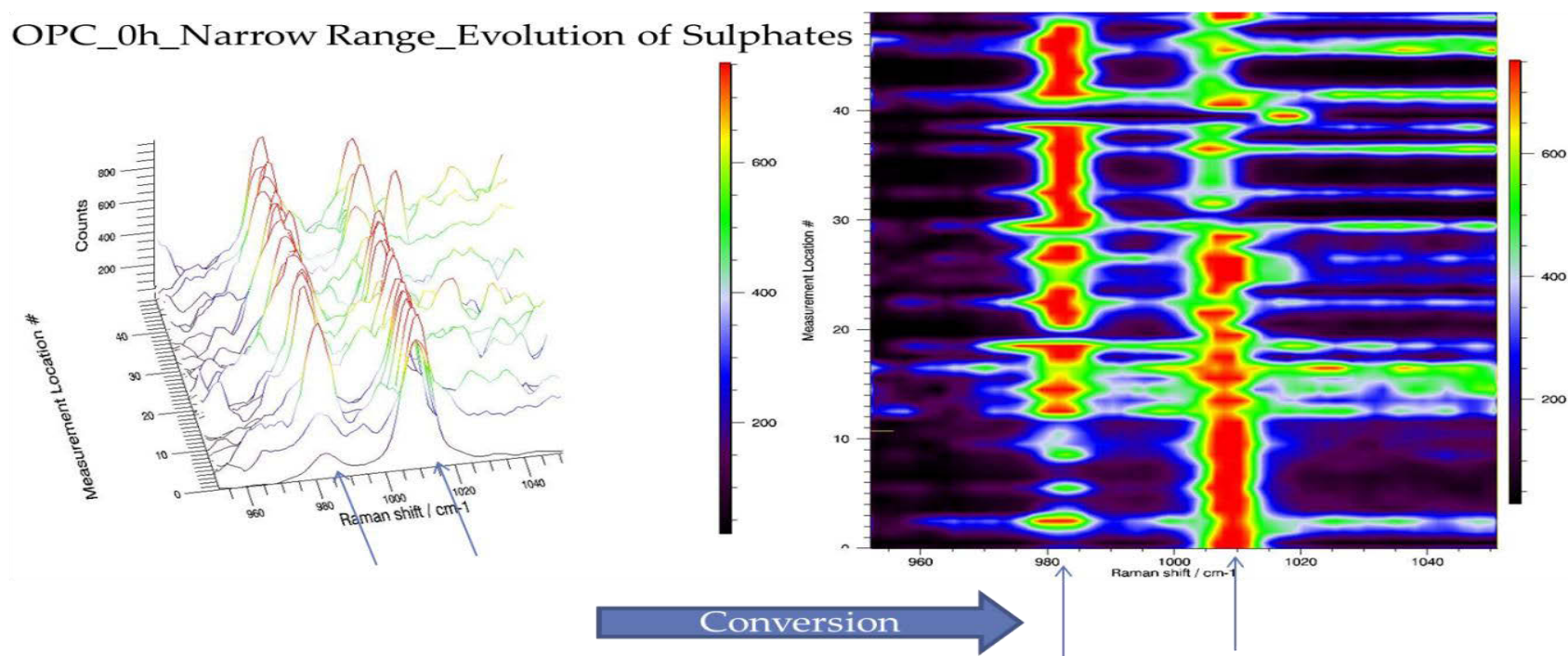


Figure 65: Presentation of evolution of sulfates data

4.2.5.2 Evolution of hydroxides

Figure 66 shows process the mapping the intensity distribution of hydroxides detected in the higher wavenumber region. Once the mapping based on the co-ordinates of the locations studied in the sample is done, the 3-d surface graph is converted to a 2-d representational image. It is to be noted that 2-d image gives an overall distribution of the concentration of analyte under study. Singular bright spots do not suggest higher concentration as they may be outliers. As the images get filled with brighter spots, we can infer that the given area under study is being populated by high intensity calcium hydroxide.

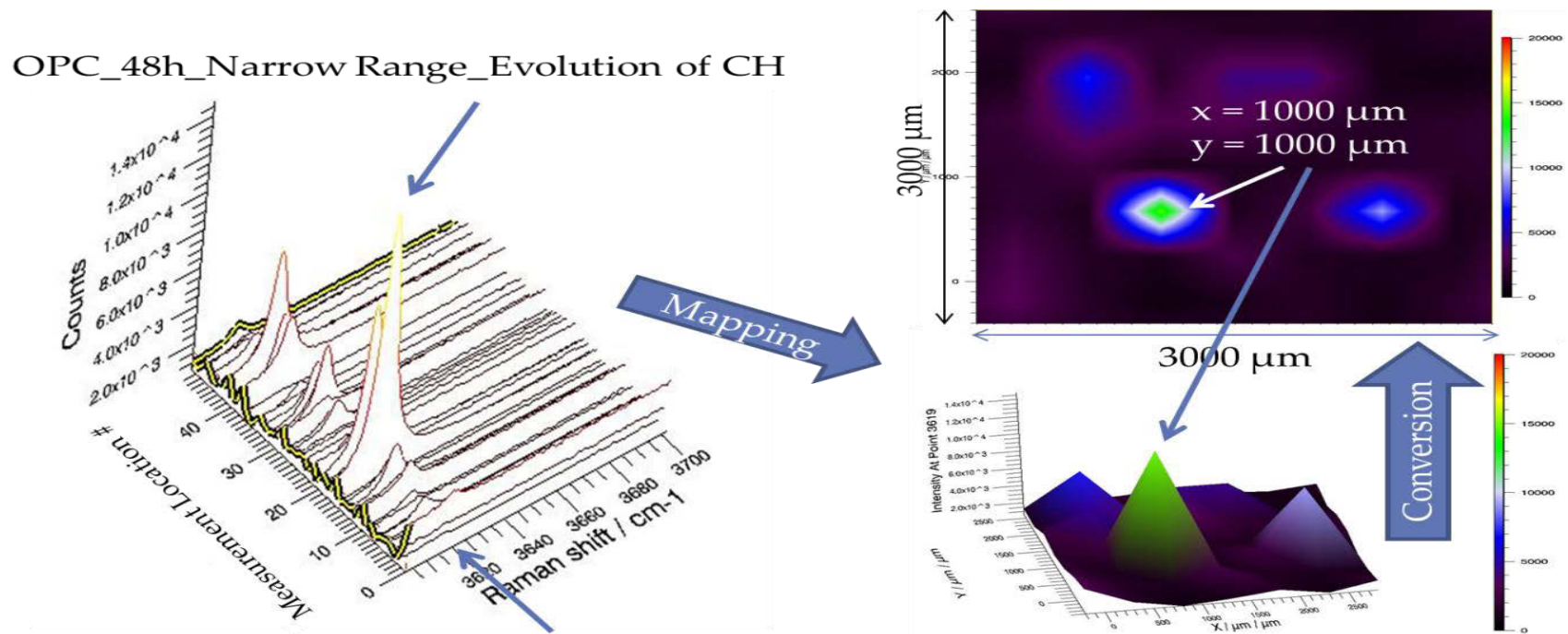


Figure 66: Presentation of evolution of hydroxides data

4.3 Dry analysis

Figure 67 shows the Raman spectra collected for the synthetic clinker phases. It can be seen that Raman spectroscopy is easily able to distinguish between the major phases of ordinary Portland cement. However, the analysis becomes complex when all these phases are intermingled with each other and are relatively impure.

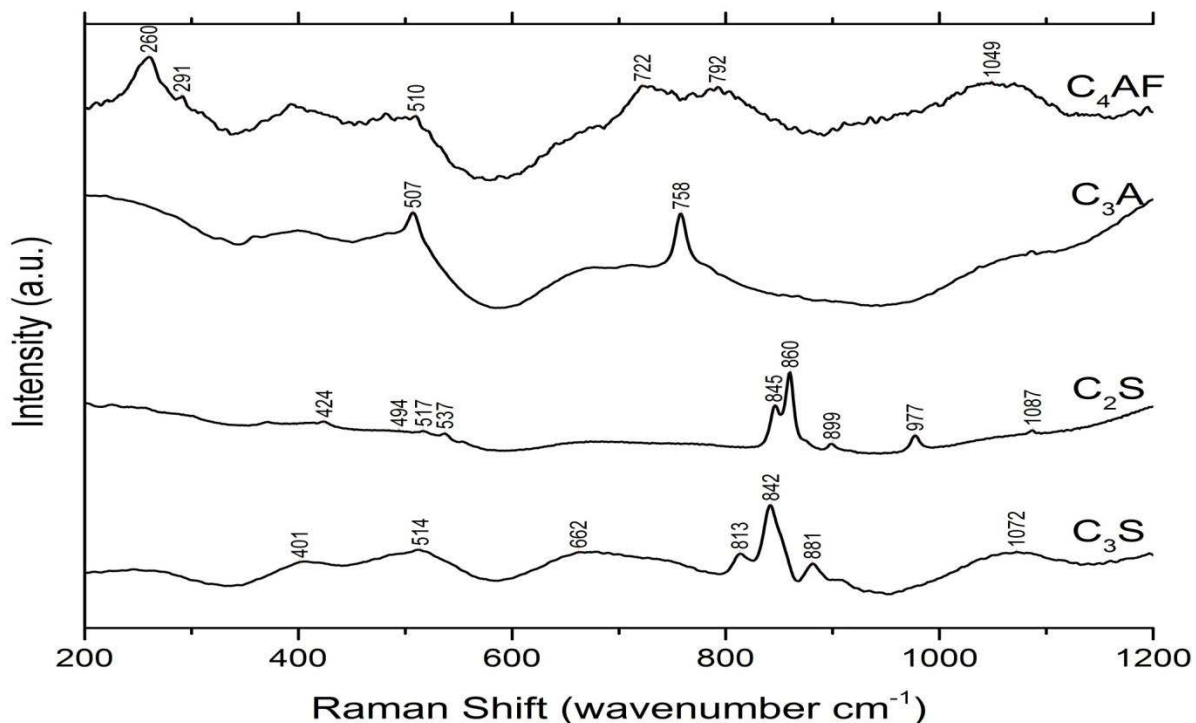


Figure 67: Raman spectra of synthetic clinker phases

4.3.1 Ordinary Portland Cement

Figure 68 shows the average of 25 spectra taken at 25 different locations on the cement dry powder samples. A square grid of five by five points was drawn on the sample, making the dimensions of the representative square area studied to be $2000 \times 2000 \mu\text{m}$ with each point spaced $500 \mu\text{m}$ apart horizontally and vertically.

It can be seen from Figure 68 that all major phases of a commercial clinker, Alite, Belite, Aluminate and Ferrite can be detected. However, there is significant overlap between the phases and possibly some fluorescence between 600-1000 wavenumber region as suggested by Newman et al. [46]. The figure is also marked by the principal vibrational modes for the molecules responsible for detection of various phases. The medium broad hump peaking at 842 cm^{-1} can be due to the overlap of peaks of both alite and belite as both have their sharpest peaks in that region [34, 38] (Also see Table 4 & 5). The stretching bands of aluminum-oxygen tetrahedral at ~ 500 and ~ 700 wavenumber are assigned to the calcium aluminate phase in the clinker (see Table 6).

The assignment of the Ferrite phase at 264 cm^{-1} is tentative as the small hump in ~ 250 region might be just a random spectral feature. The reason behind that is that the quantity of Ferrite present in OPC is much less and hence its detection is not straightforward.

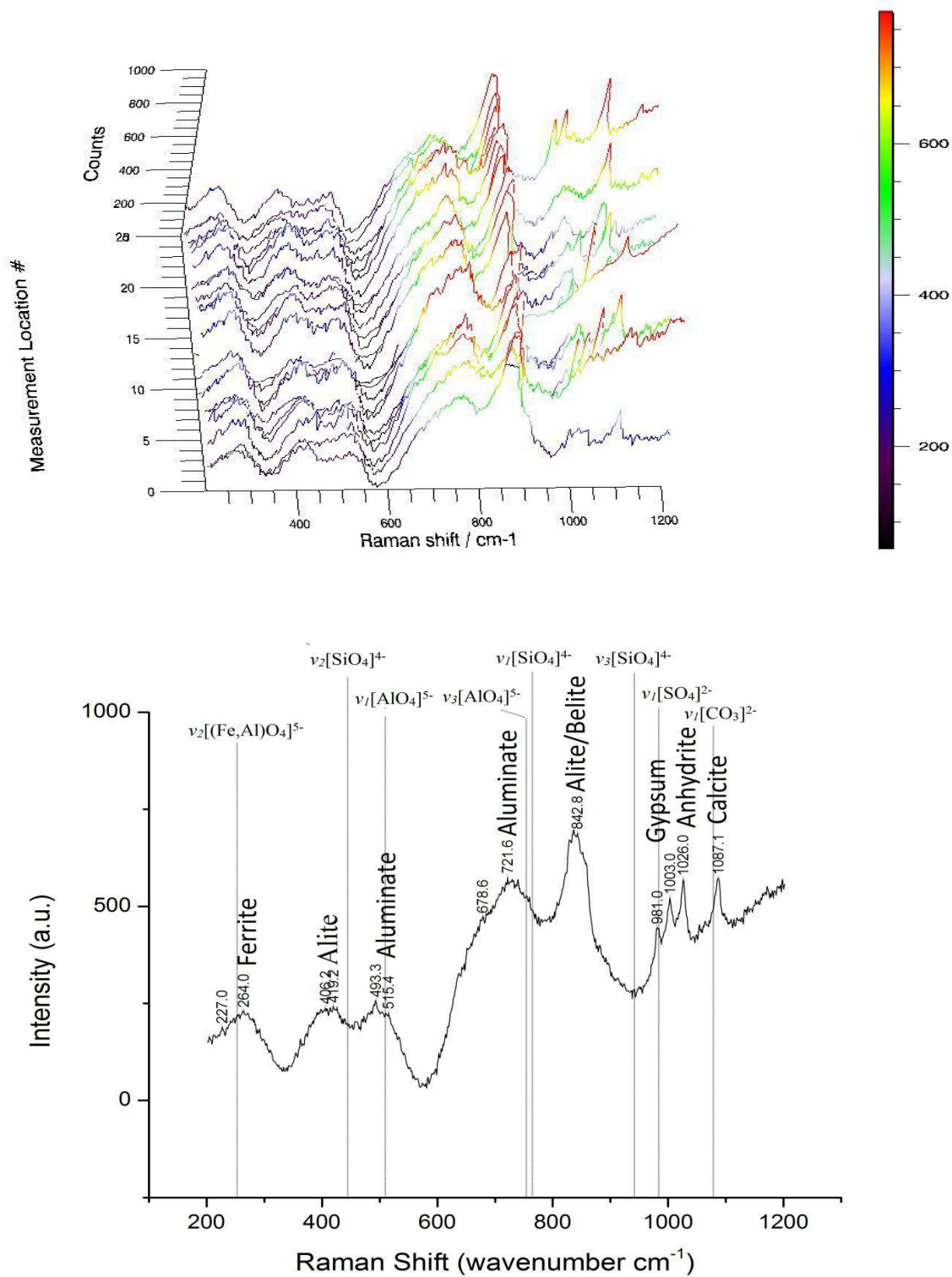


Figure 68: Raman spectrum for ordinary Portland Cement (Average of 25 spectra)

4.3.2 Fly Ashes

Figure 69, Figure 70, and Figure 71 show the Raman spectra of the three fly ashes FA1, FA2, and FA3, respectively. The average is taken of 25 different spectra at 25 different locations on the dry powder sample for each fly ash in the manner similar to the analysis method of OPC as described in 4.3.1. The resultant average is shown below the collection of 25 spectra to illustrate the comparison between real data and the average final graph. It is easy to see that by averaging a large number of spectra, not many of the features are lost and all important peaks (other than occasional outliers) are captured in the final average. Thus the average can be considered as the representative spectrum of a given fly ash. The first three figures do not include any assignment of phases and only the typical vibrational modes are marked in the spectra. The purpose behind this is to just show the possible data since accurate assignment of phases requires more literature.

However, in Figure 72 all of the spectra are shrunk down to a smaller scale and typical phases are assigned based on (Table 12) vibrations based on previous literature.

It is interesting to note when the average spectra of the three fly ashes are compared together on the same scale, there are significant differences between the calcium based phases. While the Quartz phase more or less appear consistently in the fly ashes, the anhydrite and calcite phases are most dominant in FA1, followed by FA2 and the least dominant in FA3. A somewhat similar trend for the glassy phases is also observed. This linear trend of decreasing calcium content or calcium based mineralogical phases agrees very well with the XRD (Figure 35, Figure 36, & Figure 37) and XRF (Figure 38) data discussed earlier in section 4.1. This suggests that Raman spectroscopy can serve as a complementary technique for characterizing dry fly ashes.

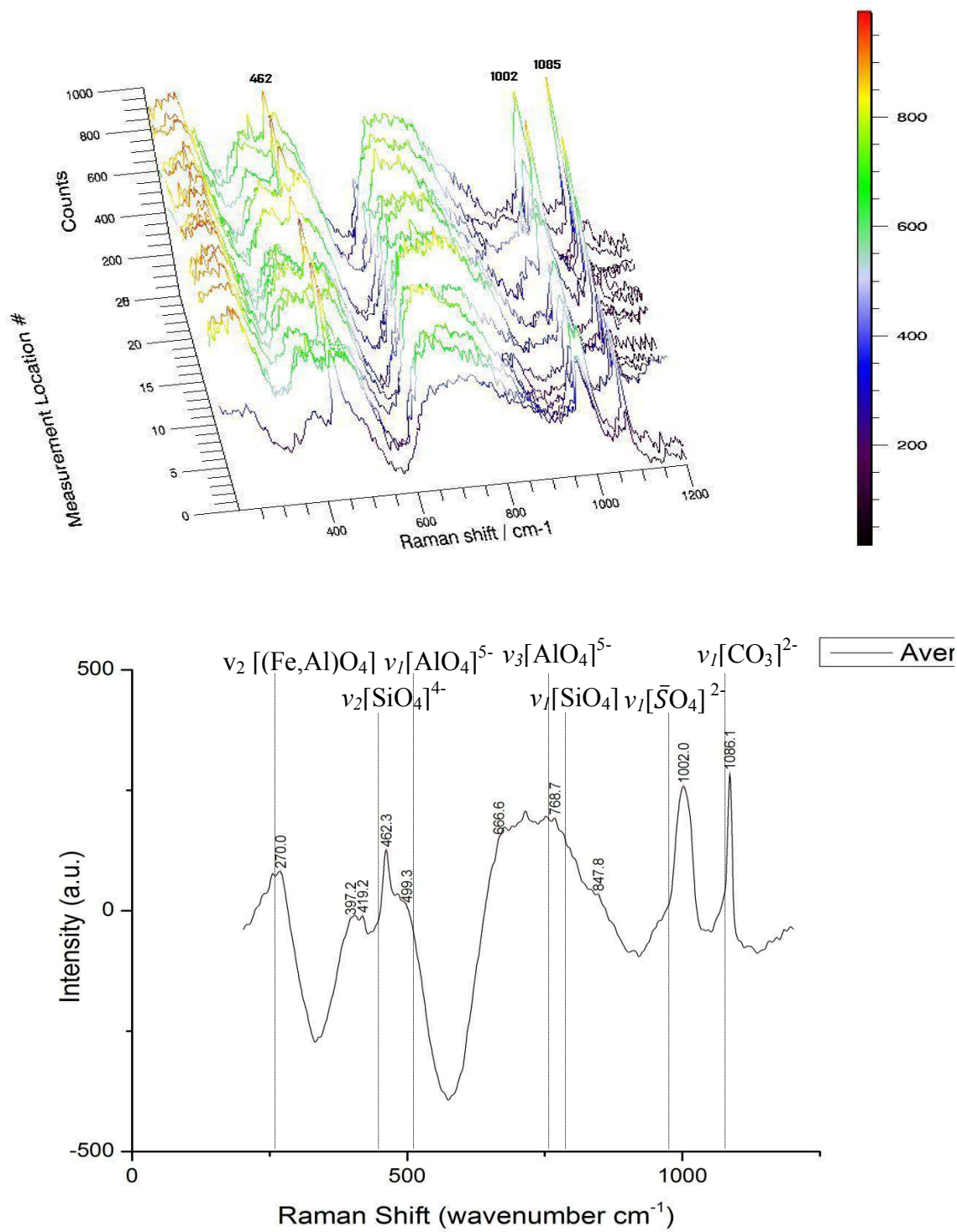


Figure 69: Raman spectrum for FA1 (Average of 25 spectra)

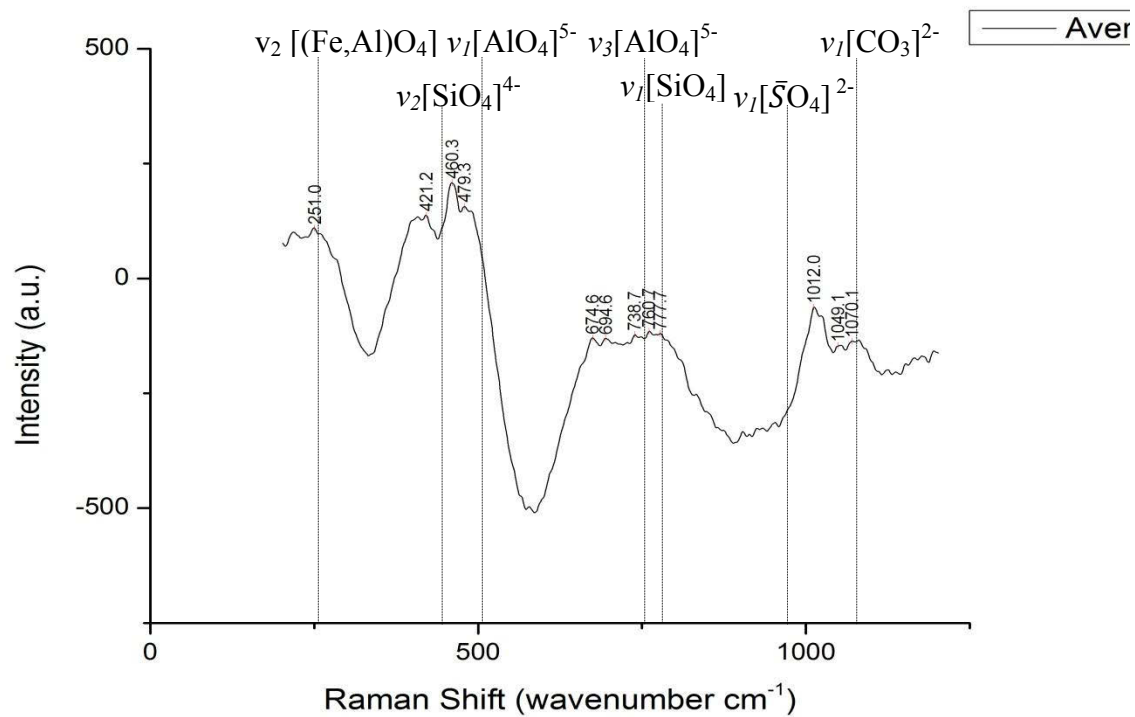
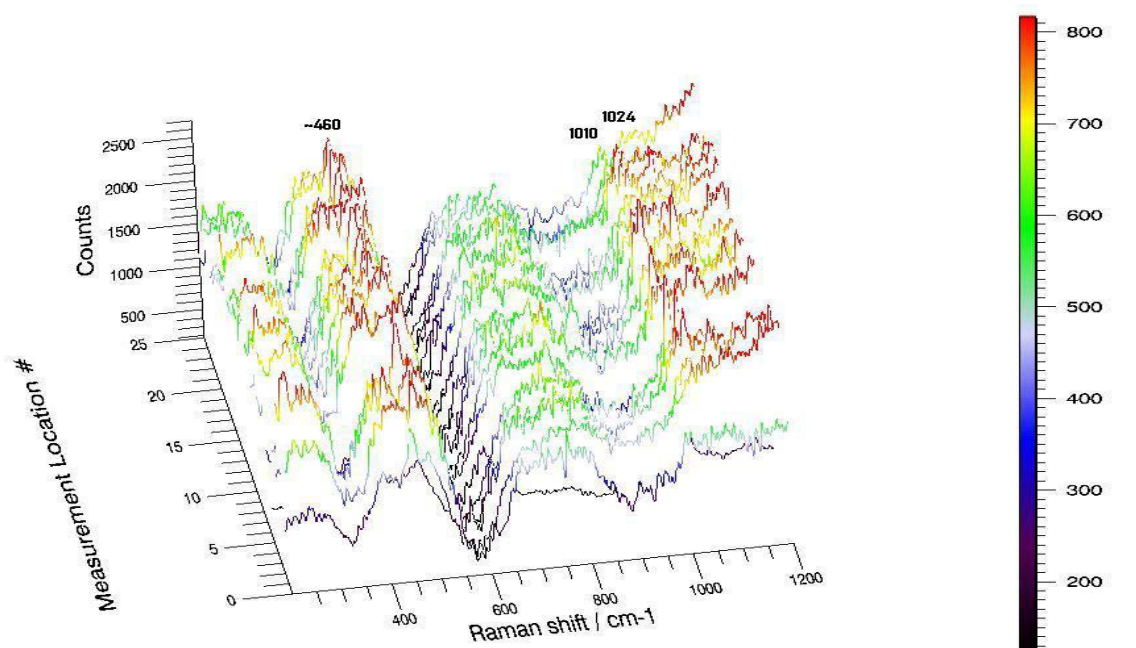


Figure 70: Raman spectrum for FA2 (Average of 25 spectra)

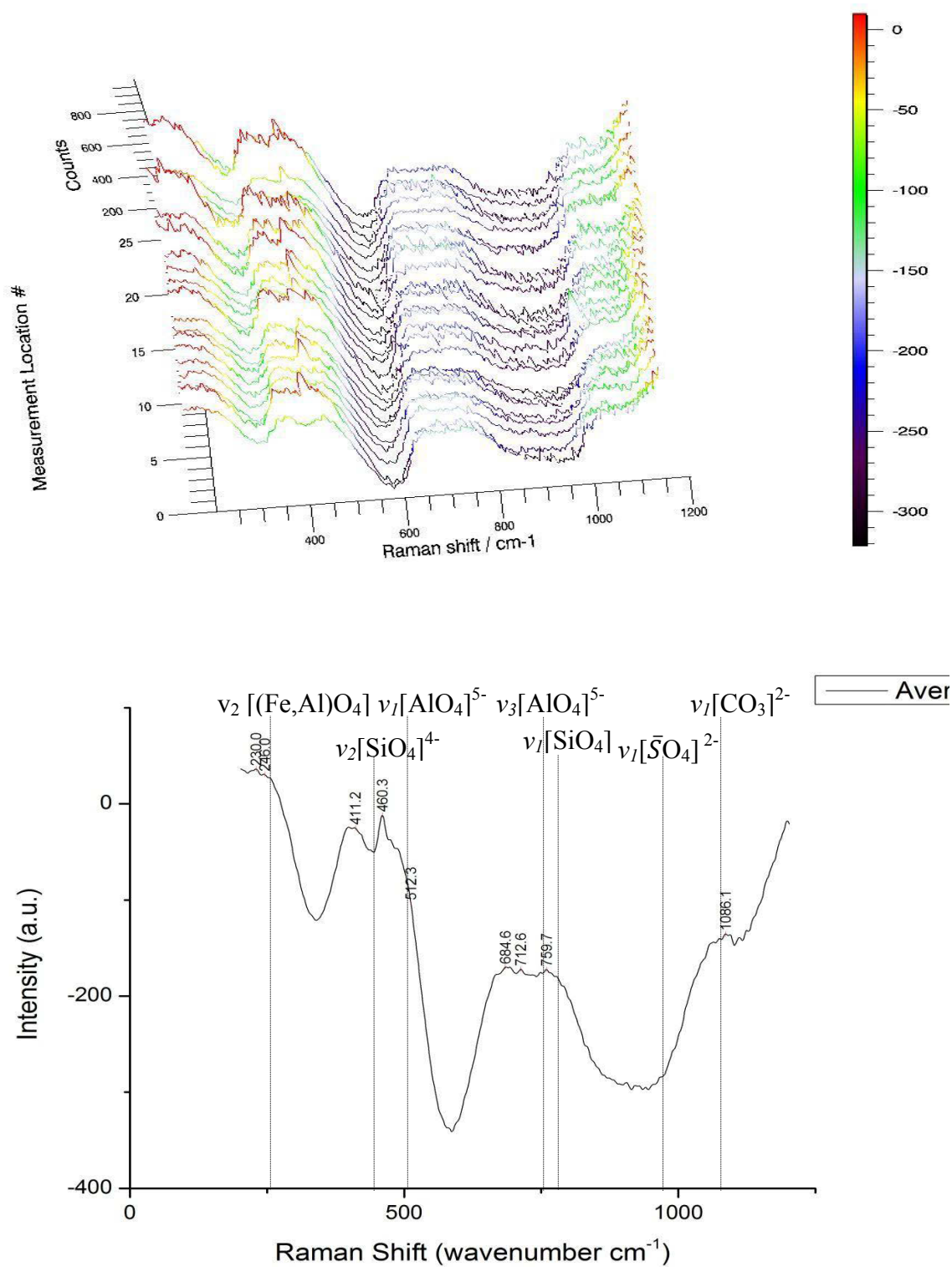
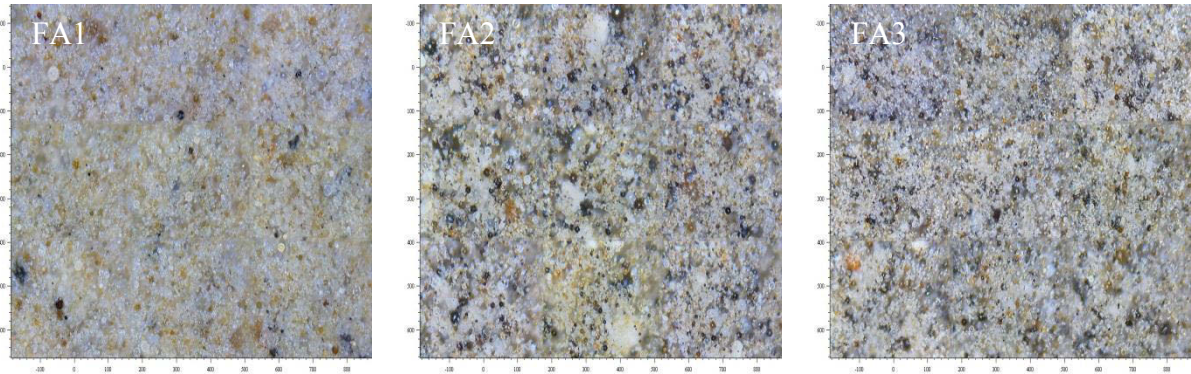
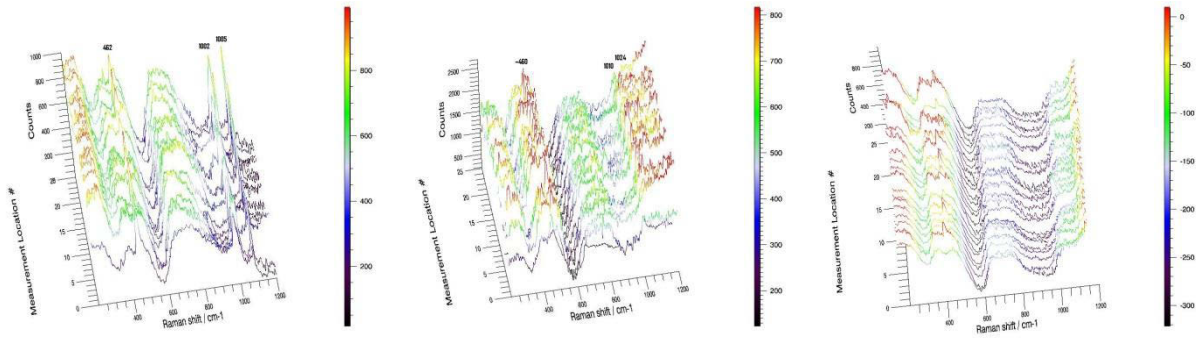


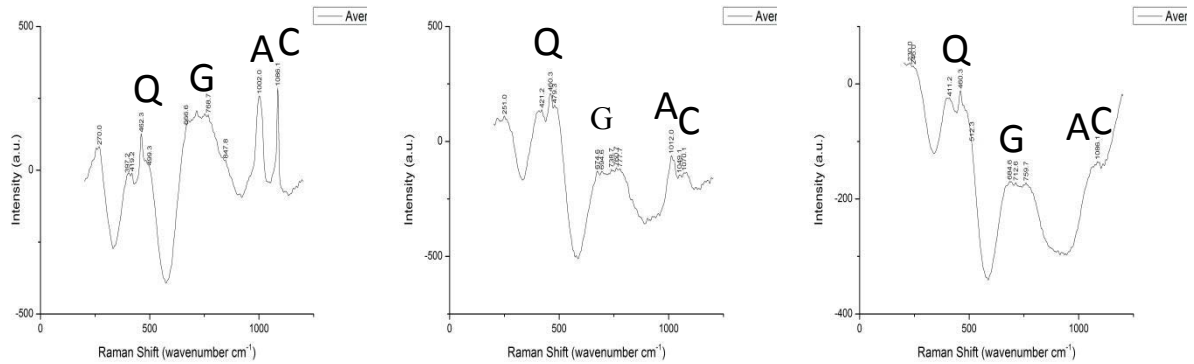
Figure 71: Raman spectrum for FA3 (Average of 25 spectra)



1) Montaged optical images taken at 20x magnification



2) Raman spectra at 25 different locations on fly ash dry powder samples



3) Average of 25 spectra (Q = Quartz, A = Anhydrite, G = Alumino-silicate type glassy phase)

a) FA1 (Class C)

b) FA2 (CFP)

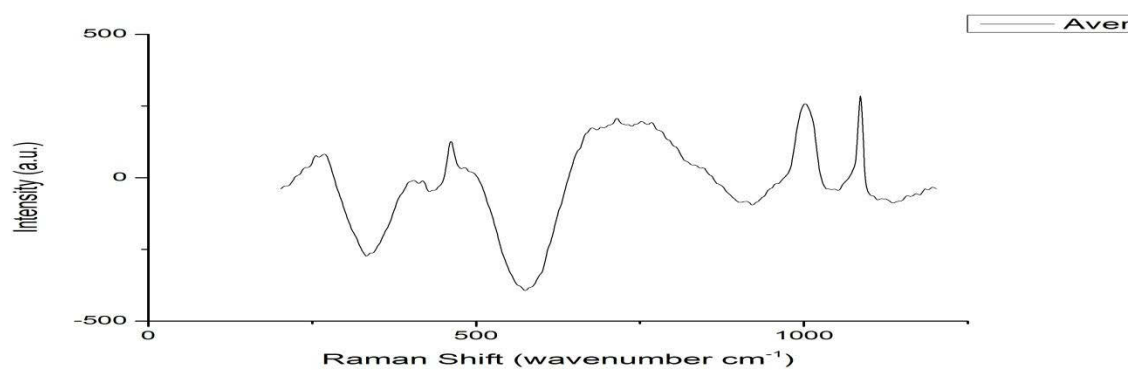
c) FA3 (JSF)

Figure 72: Comparison of three fly ashes based on their optical images and spectra.

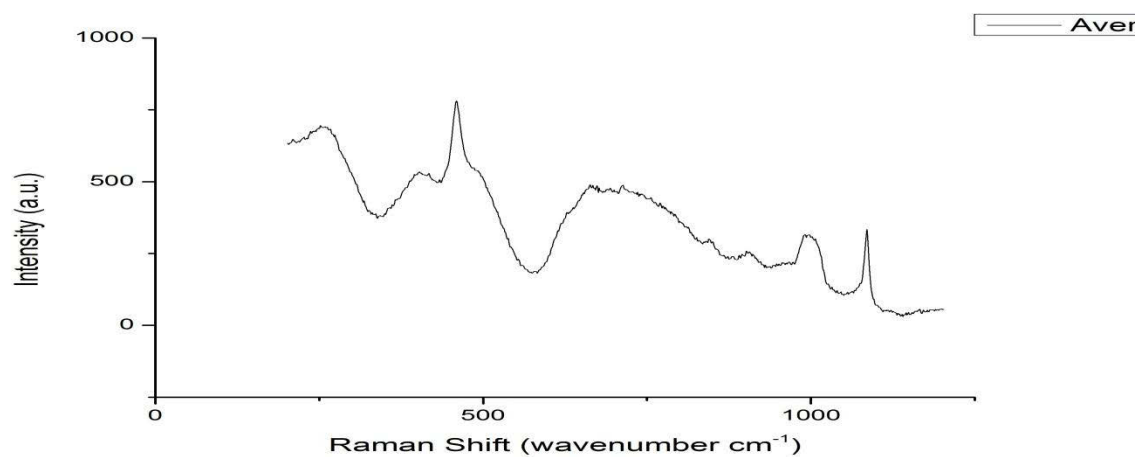
Although the characterization of fly ash phases is not as detailed as the one done by XRD, the writer hopes that as more literature will be available on Raman of fly ashes, the characterization detail can improve. Moreover, the strongest advantage for Raman is the quick analysis time (not more than 10 minutes on each fly ash).

Figure 73 shows the comparison of different magnification levels on the Raman spectra of FA1. Since we know that different magnification levels result in a laser incident spot size of a different area (resulting in a different representative area studied), its effect was checked systematically on one of the fly ashes (FA1).

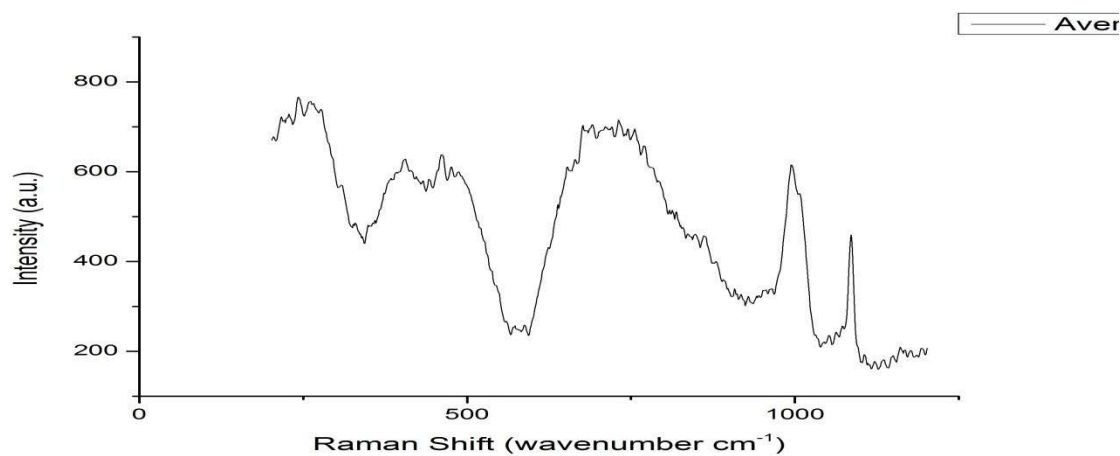
While initially, in the beginning of establishing the Raman testing parameters it was thought that magnification level did not have any significant effect and hence 5x was chosen as the standard testing level, now it does seem to make a slight difference (at least in this case). It can be seen that with increasing magnification level, the spectral resolution is increasing with more peaks visible at each broad hump. While at lower magnifications like 5x, rather smooth humps are obtained which can be useful for overall representation of phases. But for qualitative and detailed characterization, perhaps 50x is better. But then again, it depends on the particle size distribution of the fly ash under study. For a coarser fly ash, one may like to select lower magnification so as to obtain the bulk characterization of a variety of grains.



a) 5x ($\sim 100 \mu\text{m}$ spot size)



b) 20x ($\sim 25 \mu\text{m}$ spot size)



c) 50x ($\sim 10 \mu\text{m}$ spot size)

Figure 73: Comparison of different magnification levels/spot size on Raman spectrum of FA1

4.4 Wet Analysis

4.4.1 All Hydration Products

Figure 74 to Figure 78 show the evolution of hydration products at low wavenumber range for five different mixes (one control of 100% OPC, rest four 50% replacement by SiO₂, FA1-3). Since these spectra at each age are only the average of 9 different locations, they may not be very representative of the exact hydration process and that is why the trends of various species in the sample are not consistent. For a better study, more locations on the samples should be selected. But selecting more locations meant more analysis time and more analysis time means more exposure of the sample to the environmental CO₂. Hence, the locations were limited to 9 with a thirty second exposure to keep the total analysis time for a given sample at a given age to not more than 20 minutes.

As an overall analysis, it can be seen that slight carbonation still was measurable in the samples even though a fresh sealed sample was used at each age (with previous ones discarded after analysis). This slight carbonation may be due to the vibrational modes of calcite already present in the dry powders of cement and fly ashes. In Figure 74 the peak near ~ 460 due to bending mode of O-Si-O molecule assigned to the crystalline silica present in the internal standard silicon dioxide which was used to replace OPC. A consistent peak at all ages shows its role as an inert filler which does not react or interfere with the cement hydration process. However, it is not understood why the C-S-H hump is weak and C₃S/C₂S peaks are almost missing from the spectra. There is some activity going on the sulfates and CH region but again it is not very consistent.

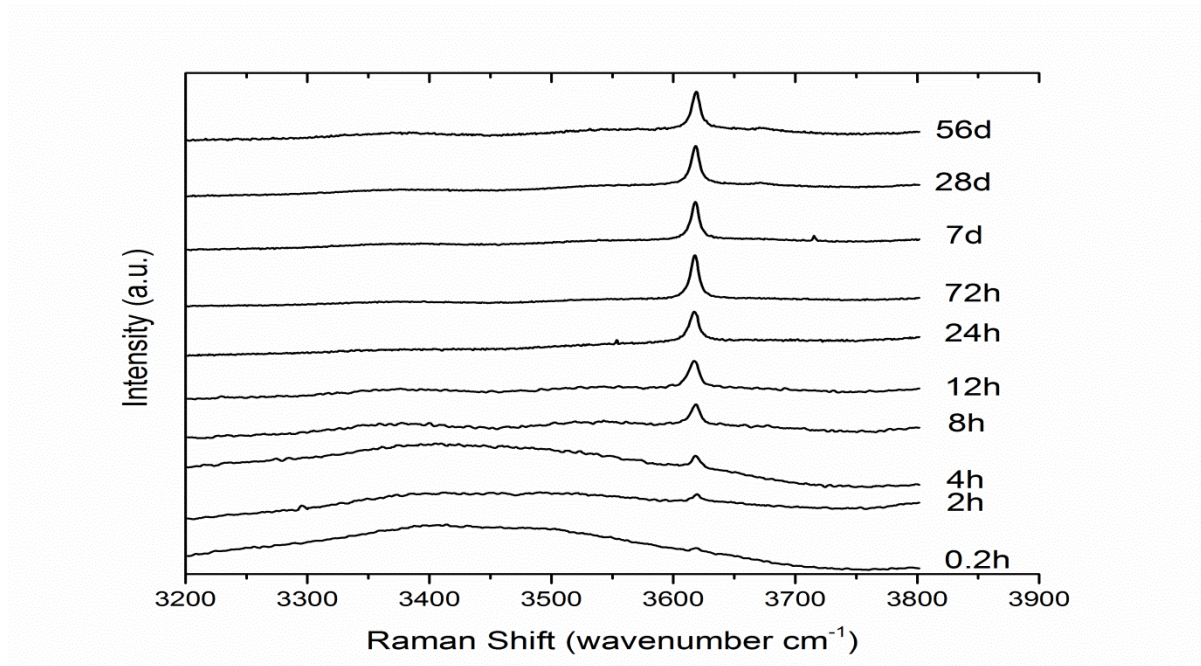


Figure 75 shows the hydration process of 100%OPC paste. Ideally, the C_3S/C_2S peaks should decline with time, CH peak should increase, and the C-S-H polymerization should occur with an increasing curing age [43]. CH is consistently present in all mixtures but it should be kept in mind since all these figures are normalized, a quantitative evaluation of CH can not be made in this manner.

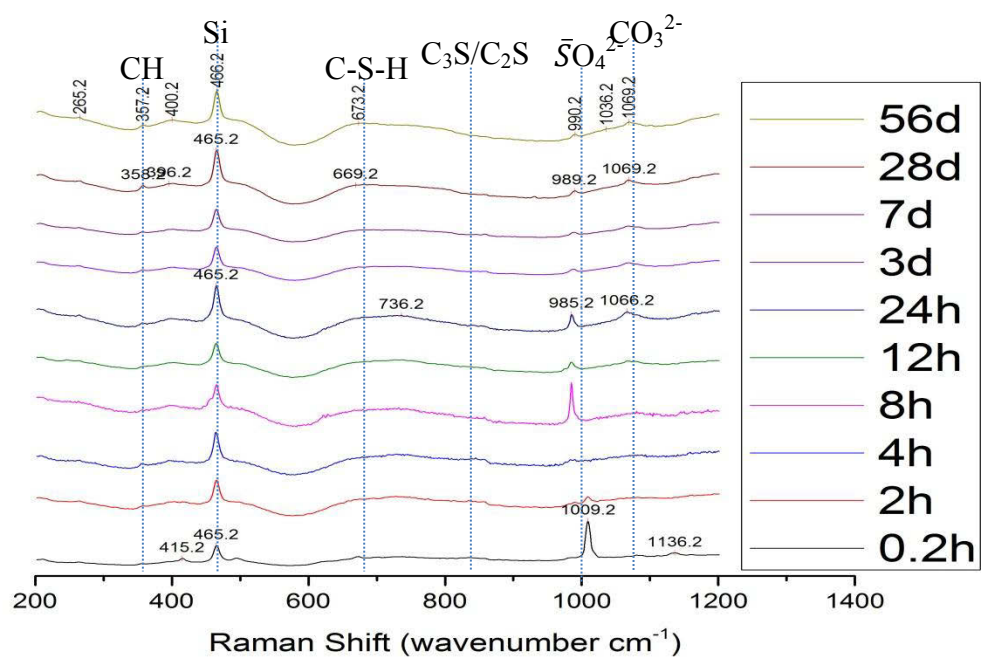
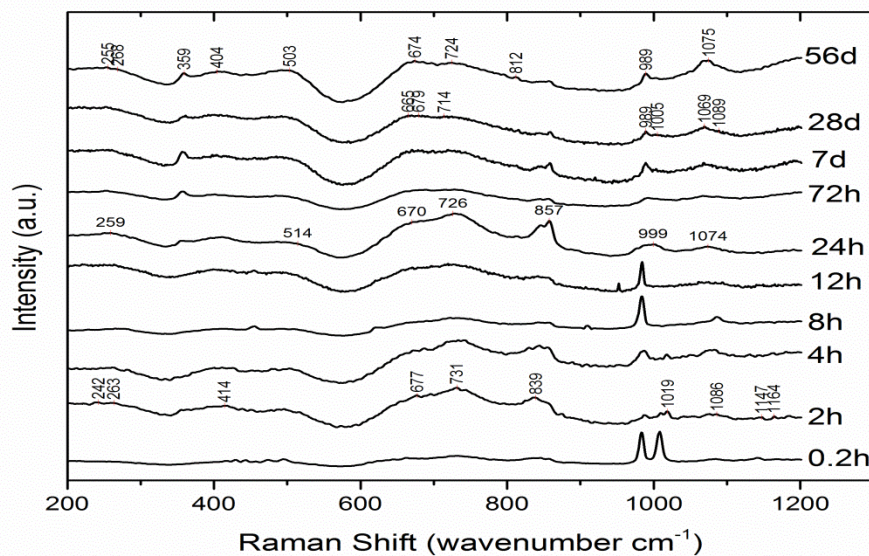


Figure 74: Raman spectra following the hydration process of 50%SiO₂+50%OPC



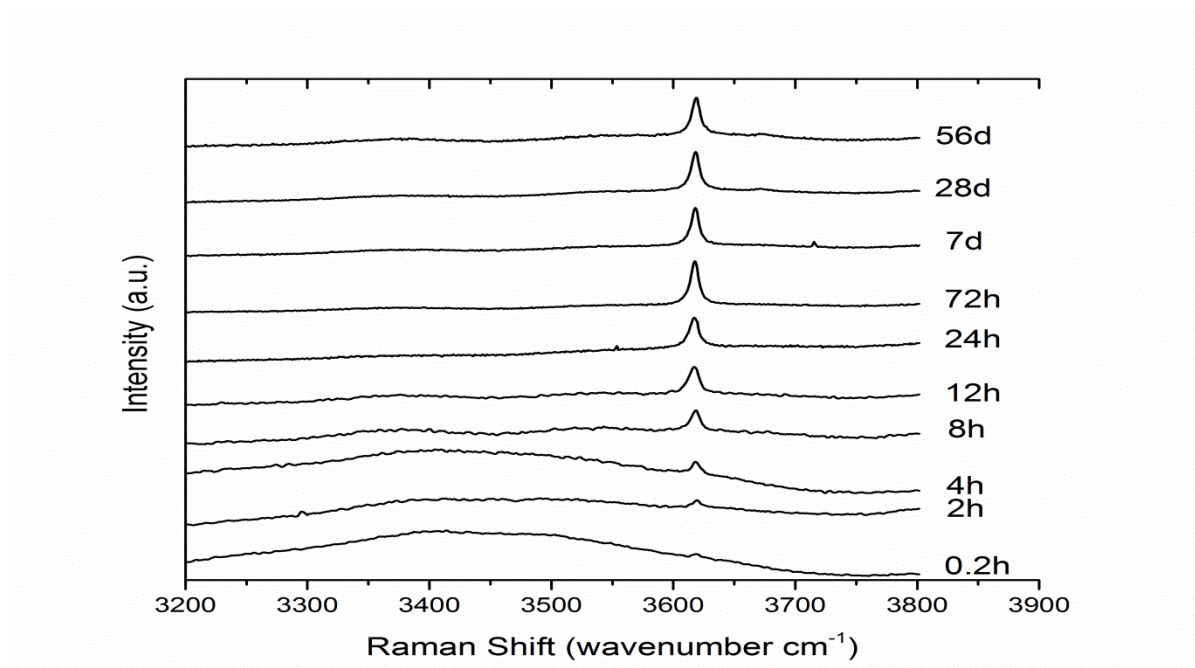


Figure 75: Raman spectra following the hydration process of 100%OPC

Although such a linear trend was not observed (due to reasons explained above), but it can be seen that at 56 days of age the C_3S/C_2S have somewhat disappeared and CH peaks have grown in intensity. The silicate polymerization of C-S-H would be very hard to see in amorphous, commercial materials selected here and hence cannot be resolved in this case (unless it is specifically focused upon). It should also be noted that region near 1000 wavenumber where sulfates are evolving seems to be the best Raman scatterer at low range and that is why it was chosen for further study. This thesis work focused on evolution of sulfates and hydroxides and better results are obtained in those areas due to large number of locations studied per sample (49) and they are discussed in detail in section 4.4.2.

On comparing the low range hydration products of the three fly ashes, the only visible difference is the amount of peaks present. While in FA1 it seems the reaction is ongoing at all ages with hydration products appearing at all ages, in FA3 there is hardly any low range hydration product present. This may indicate that perhaps FA3 is only acting as a filler in the paste matrix or its large, coarse grains have coated the reacting clinker grains whose hydration products are hidden beneath the surface formed by the amorphous fly ash grains.

However, interestingly, it will be seen later that FA3 paste is resulting in huge formation of CH at the higher wavenumber region.

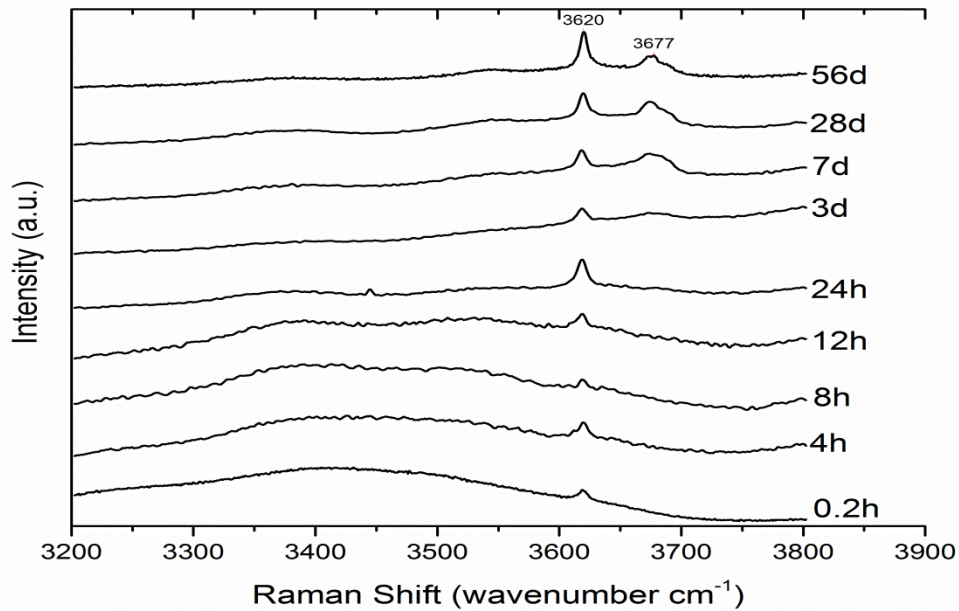
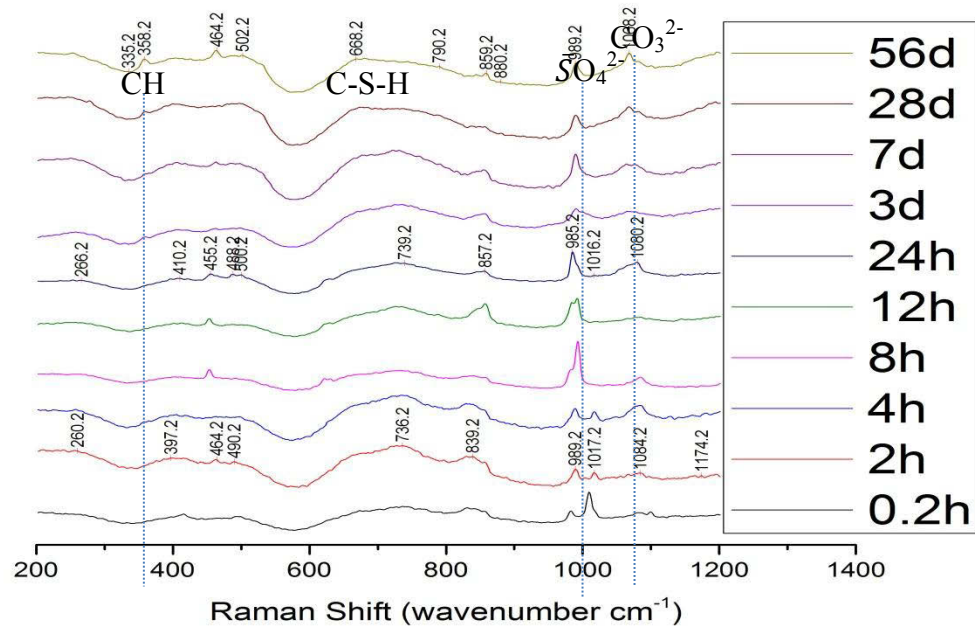


Figure 76: Raman spectra following the hydration process of 50%FA1+50%OPC

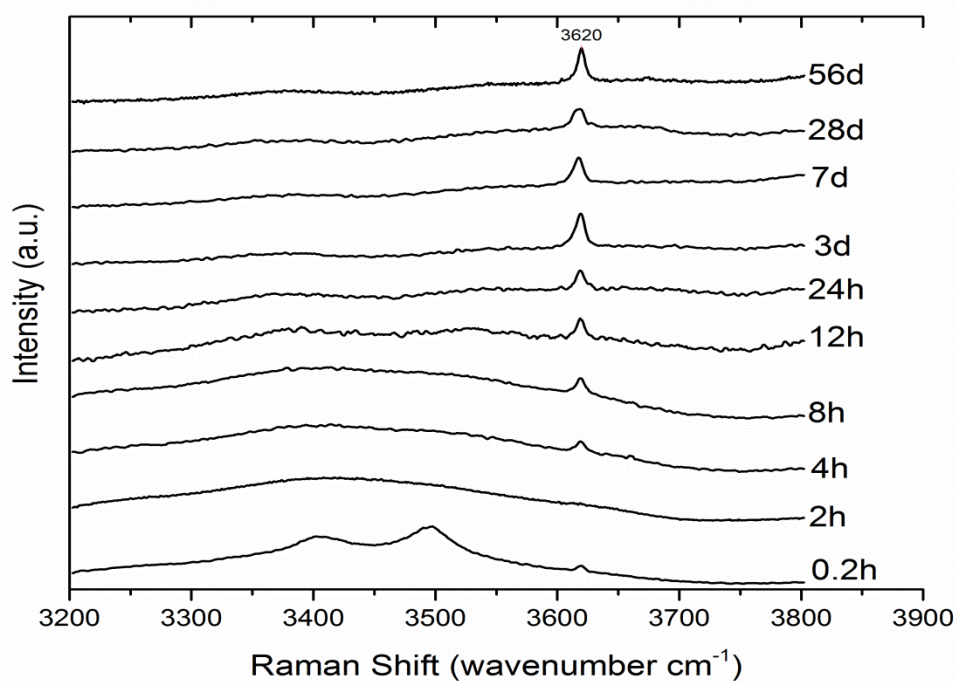
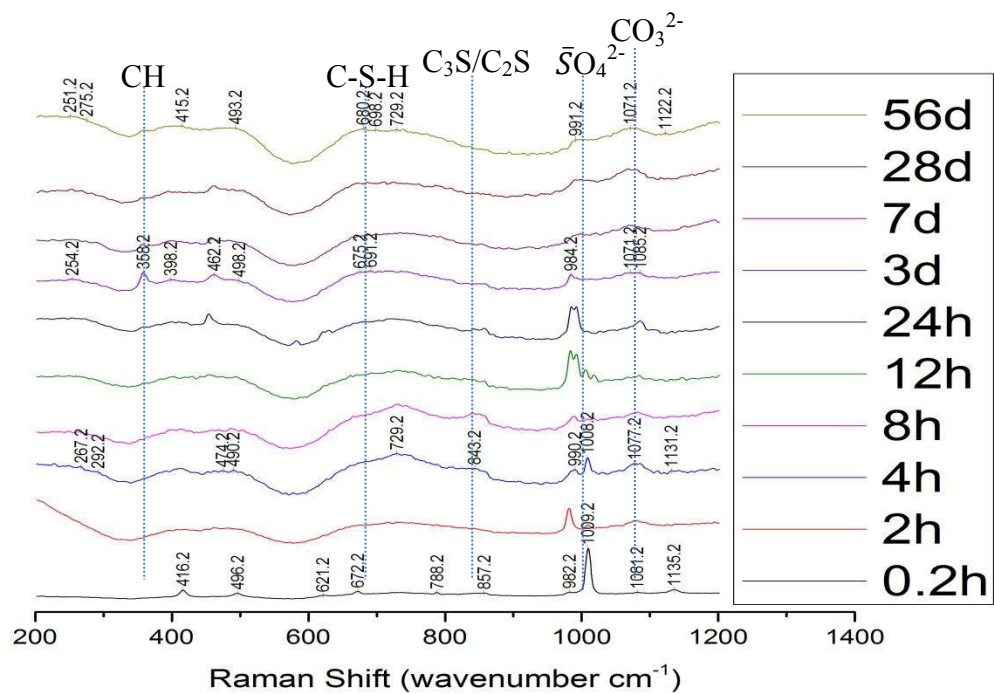


Figure 77: Raman spectra following the hydration process of 50%FA2+50%OPC

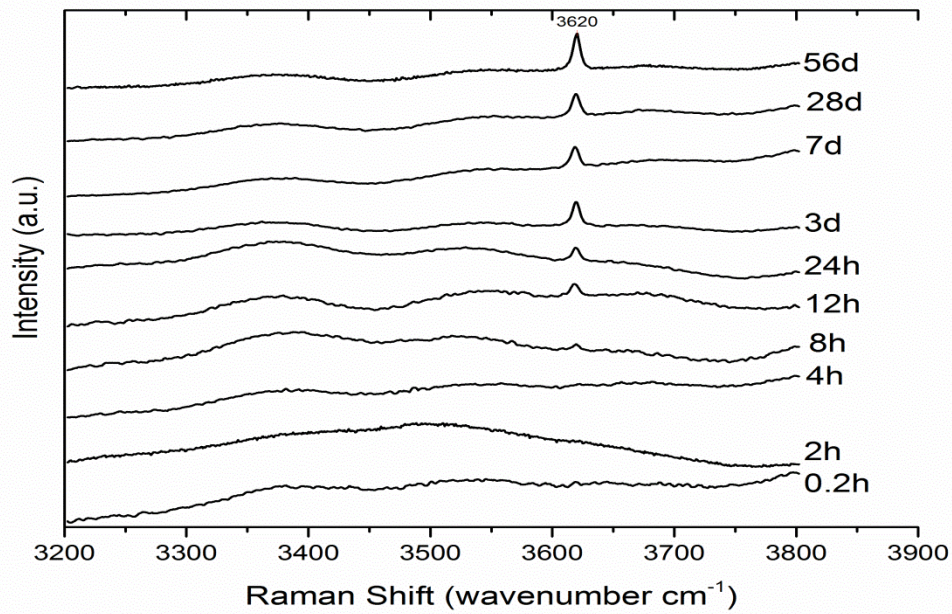
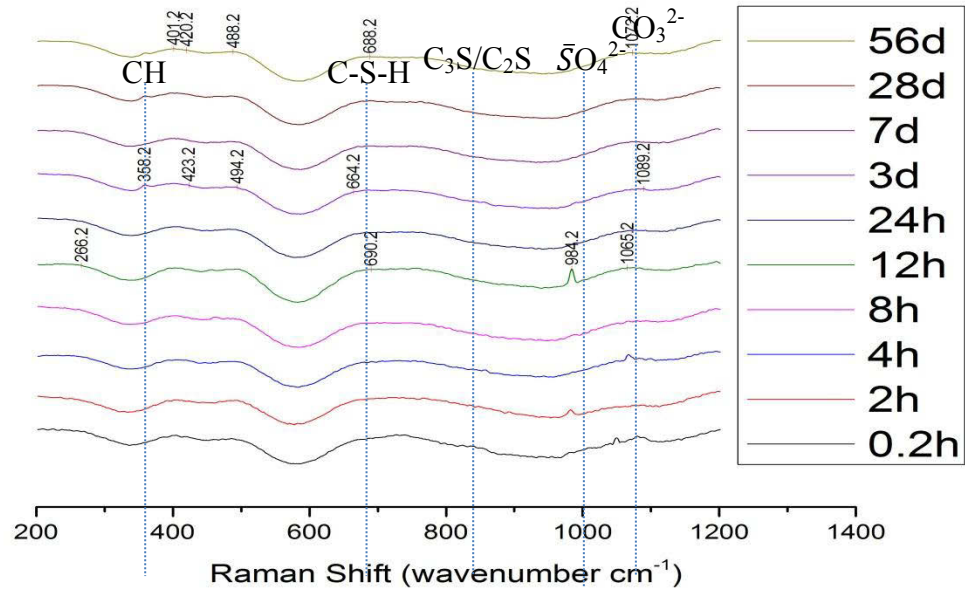


Figure 78: Raman spectra following the hydration process of 50%FA3+50%OPC

4.4.2 Evolution of sulfates

Figure 79 shows the spectra for pure gypsum and ettringite measured to verify the peak positions assigned in the commercial cementitious systems. It is to be noted that both the

peak location and intensity is quite uniform in such synthetic phases which is not necessarily the case in commercial systems discussed later.

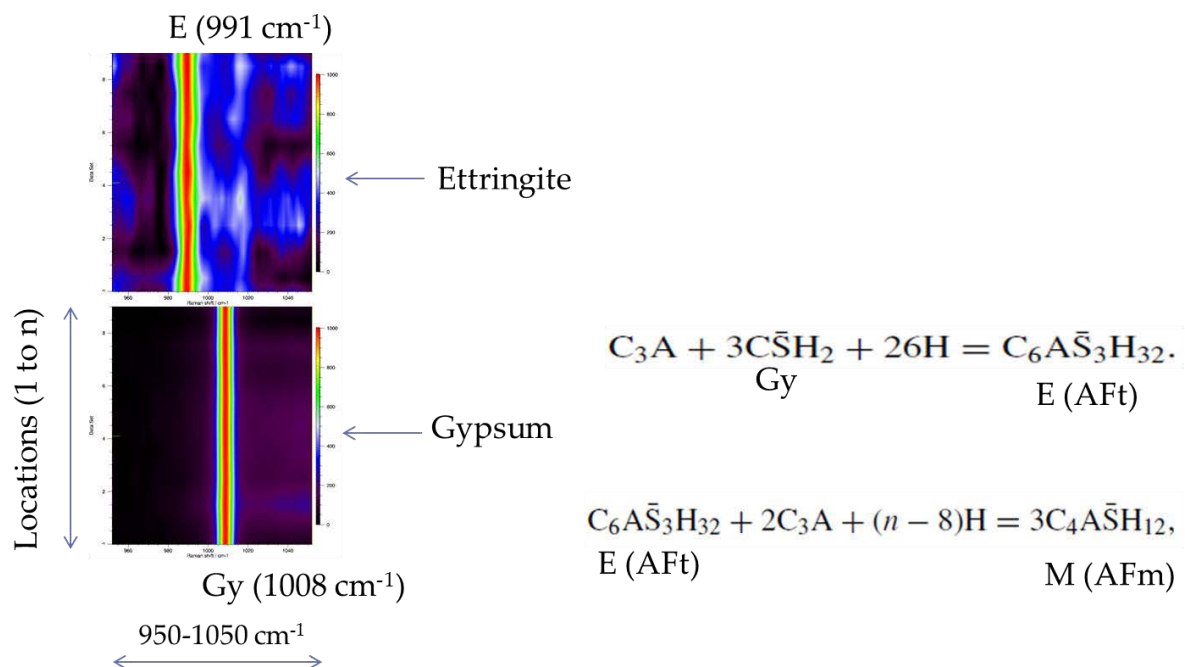


Figure 79: Crystalline and pure sulfates

4.4.2.1 OPC

Figure 80 shows the evolution of sulfates in 100% OPC paste. The initial peak at 1007 cm^{-1} is assigned to gypsum due to $\nu_1[\bar{5}\text{O}_4]^{2-}$ symmetric stretching mode. The second peak at 982 cm^{-1} is tentatively assigned to ettringite or AFt type phase. The assignment is tentative because based on the literature pure ettringite appears at 989 cm^{-1} and the band appearing at 982 or 983 is usually assigned to AFm type phase [69]. Moving forward in time, this peak due to symmetric stretching of sulfate molecule appears to be transitioning from 982 cm^{-1} to 987 cm^{-1} between the ages of 24 hours and 48 hours. So it can be safely said that after 48 hours, a pure form of ettringite has crystallized in the system. However, prior to 48 hours the band at 982 is some form of AFt phase and possibly not AFm. As it is known already that AFt should convert to AFm not vice versa [80].

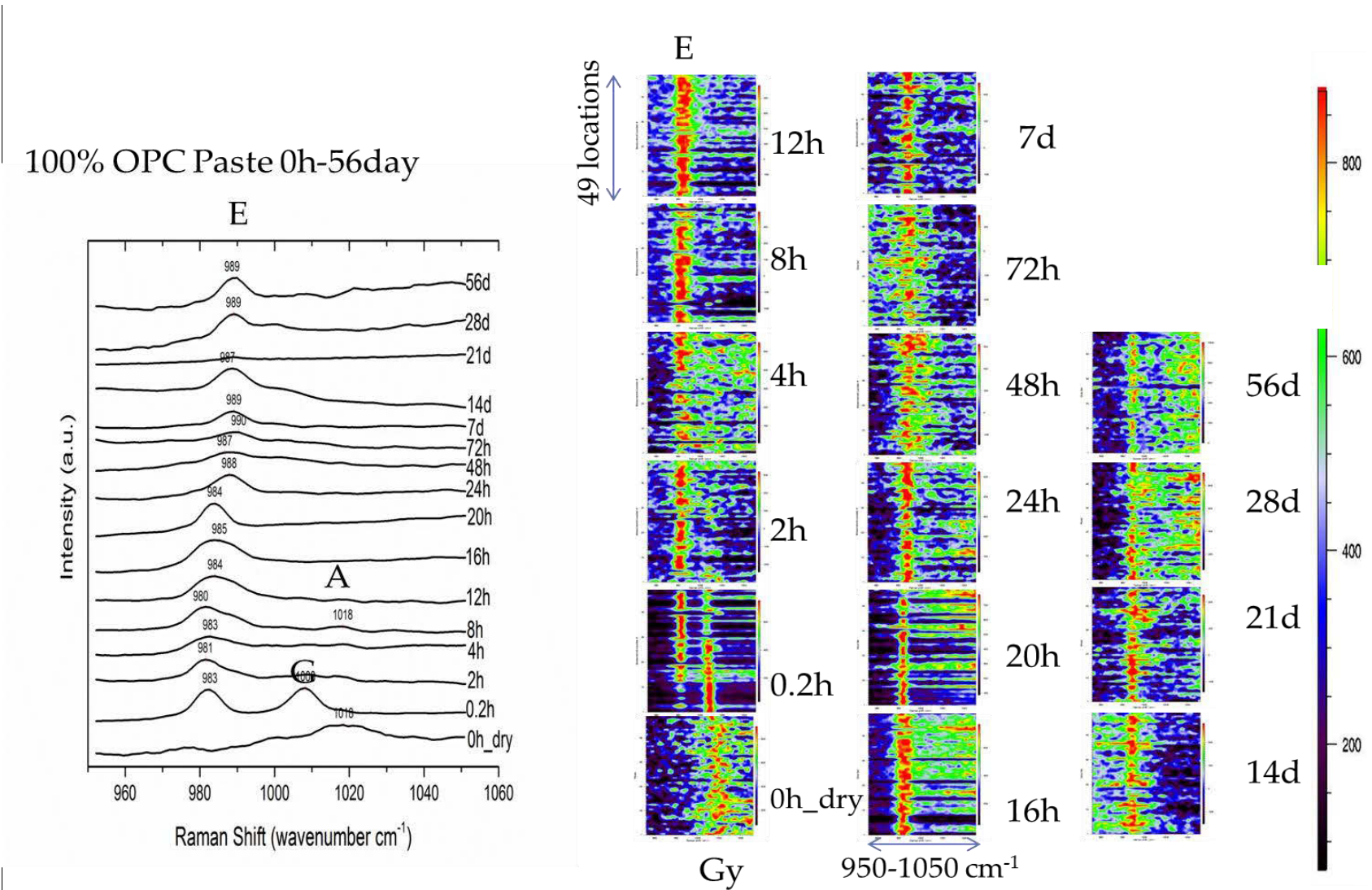


Figure 80: Evolution of sulfates in 100%OPC paste. E = Ettringite; G = Gypsum; A = Anhydrite

To further resolve this issue, a figure from the extensive study on sulfates by Renaudin et al. [69] can be referred. As seen from Figure 26, pure forms of Ettringite and Monosulfoaluminate can be easily distinguished from each other by Raman spectroscopy. At low range wavenumbers, according to the study of Renaudin et al., the Ettringite principle band occurs between $989\text{--}991\text{ cm}^{-1}$ and for AFm the principal peak occurs at 982 cm^{-1} (see Table 11). However, interestingly, there is shoulder peak of AFm at 992 which may overlap with AFt phase. Also, while most of the previous work may agree with this, Frias and Ramirez [51] assigned bands at 986 and 991 to AFm which suggests some difficulty in distinguishing both these phases due to a narrow difference between their strongest peaks. However, the hydroxyl peak of AFm at 3675 cm^{-1} is suggested by several authors (Table 11) and is a characteristic mode of AFm which can greatly help in distinguishing it from AFt. Lastly, it must be kept in mind that most of the assignments in the literature were done on pure, synthetic or lab prepared crystals while the current study is dealing with rather impure hydration products from commercial binders. Thus, distinguishing AFt from AFm might not be as straightforward as it seems in such systems.

4.4.2.2 Fly Ashes

Figure 81 and Figure 82 show the evolution of sulfates in three pastes prepared from the 50% replacement of cement by three different fly ashes.

For the case of FA1, the one which seems to be most reactive, is the most interesting one. At the beginning hours both Gypsum and Anhydrite is detected, suggesting strong presence of sulfates in the system. This agrees well with the presence of the Anhydrite phase detected strongly in the dry data of FA1 (see Figure 72) This means that an AFt type phase should be favored, and within the time frame of 2 to 8 hours peaks nearing 989 cm^{-1} are detected. There is a sudden shift of these peaks to 991 cm^{-1} which could mean two things: either the ettringite is recrystallizing between 12 to 24 hours or this is the shoulder peak of AFm as suggested by Renaudin et al. After 24 hours, beginning from 28 hours up to 28 days the peaks fall back to 989 cm^{-1} region which are tentatively assigned to AFm type phase. The reason behind that assignment will be more clear after looking at the evolution of hydroxyls data for this fly ash

where at 7 days the characteristic 3675 cm^{-1} mode appears. The appearance of the secondary mode supports this assignment, even though 989 cm^{-1} is not historically related to AFm type phase. Again, it can be said that perhaps a mixed form of AFt and AFm type phase exist in the system and a clear distinction is difficult to achieve in such a complex and heterogeneous system.

Lastly, it is quite interesting to compare the images in Figure 80 with the calorimetric data of FA1 in Figure 39. On careful observation it is easy to see that at around 20 hours when the peak of the sulfoaluminate phase is strongest at 991 cm^{-1} , the calorimetric data also shows the secondary peak in the hydration process of FA1. This secondary peak is often related to recrystallization or intense reaction of the aluminate phase in a fly ash [80].

In case of FA2, the ettringite formation is seemingly slower than FA1 as up to 8 hours no clear peaks are seen which can be assigned to a sulfo-aluminate phase. The gypsum and anhydrite phase are readily available in perhaps dry form since the early reaction hours and eventually begin to disappear. There is a slight evidence of parallel existence of AFt and AFm at 12 hours due to dual peaks of 980 and 991 cm^{-1} and at 20h and 48 hours dual peaks are seen again. But eventually after 7 days, consistent peaks near the 989 region are seen which can either be AFt or AFm. But since no secondary hydroxyl peak is seen for AFm, this peak is tentatively assigned to AFt. One thing which is clear in this case is that there is a consistent oscillation between AFt and AFm phases as seen by the dual peaks at several ages. The high amount of Iron present in this fly ash may also be responsible in increasing the complexity in interpretation of results due to the iron ion inclusion in such phases.

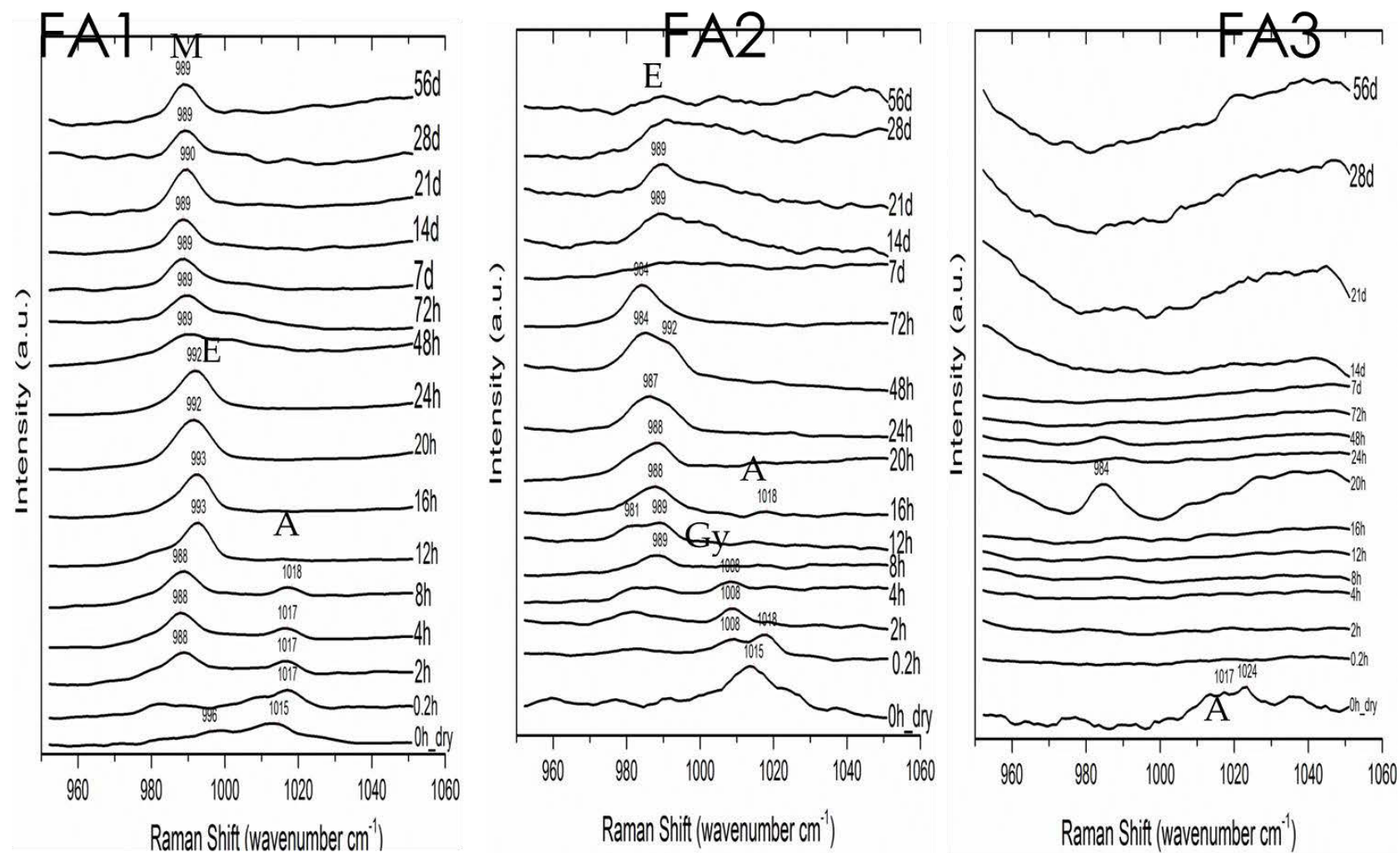
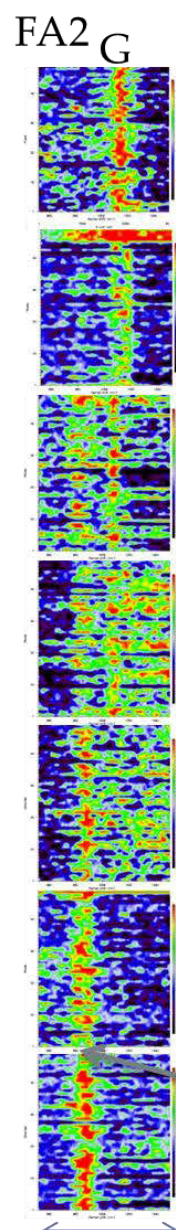
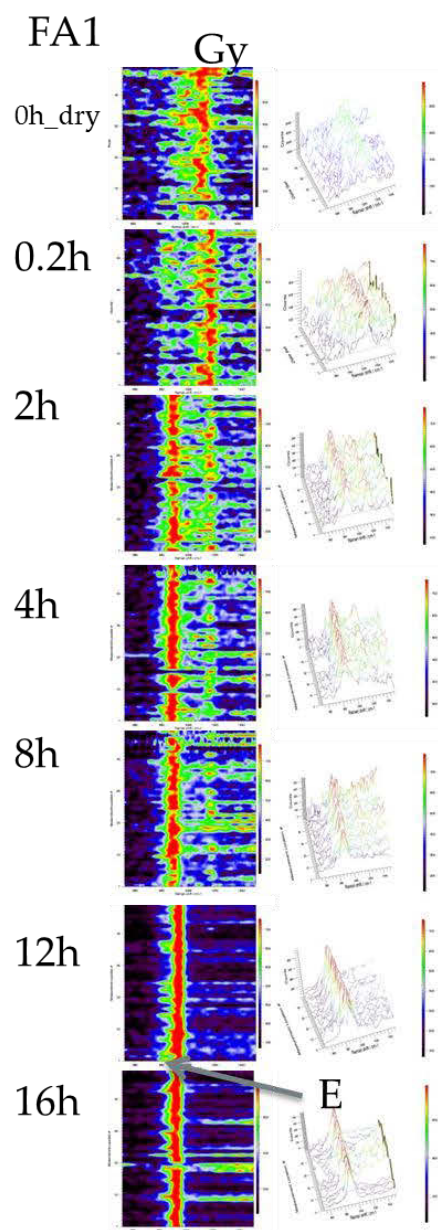
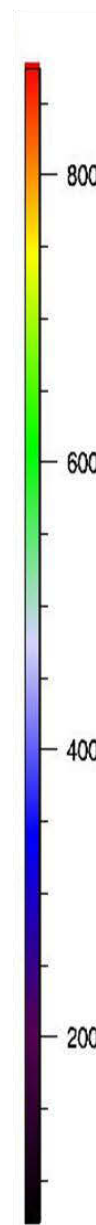
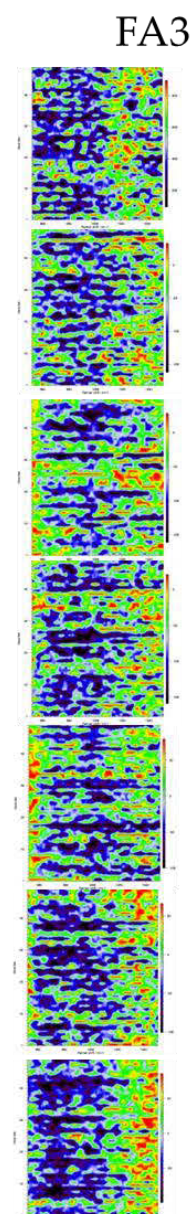


Figure 81: Evolution of sulfates in 50%FA+50%OPC pastes. E = Ettringite; G = Gypsum; A = Anhydrite; M = Monosulfoaluminate



950-1050 cm^{-1}



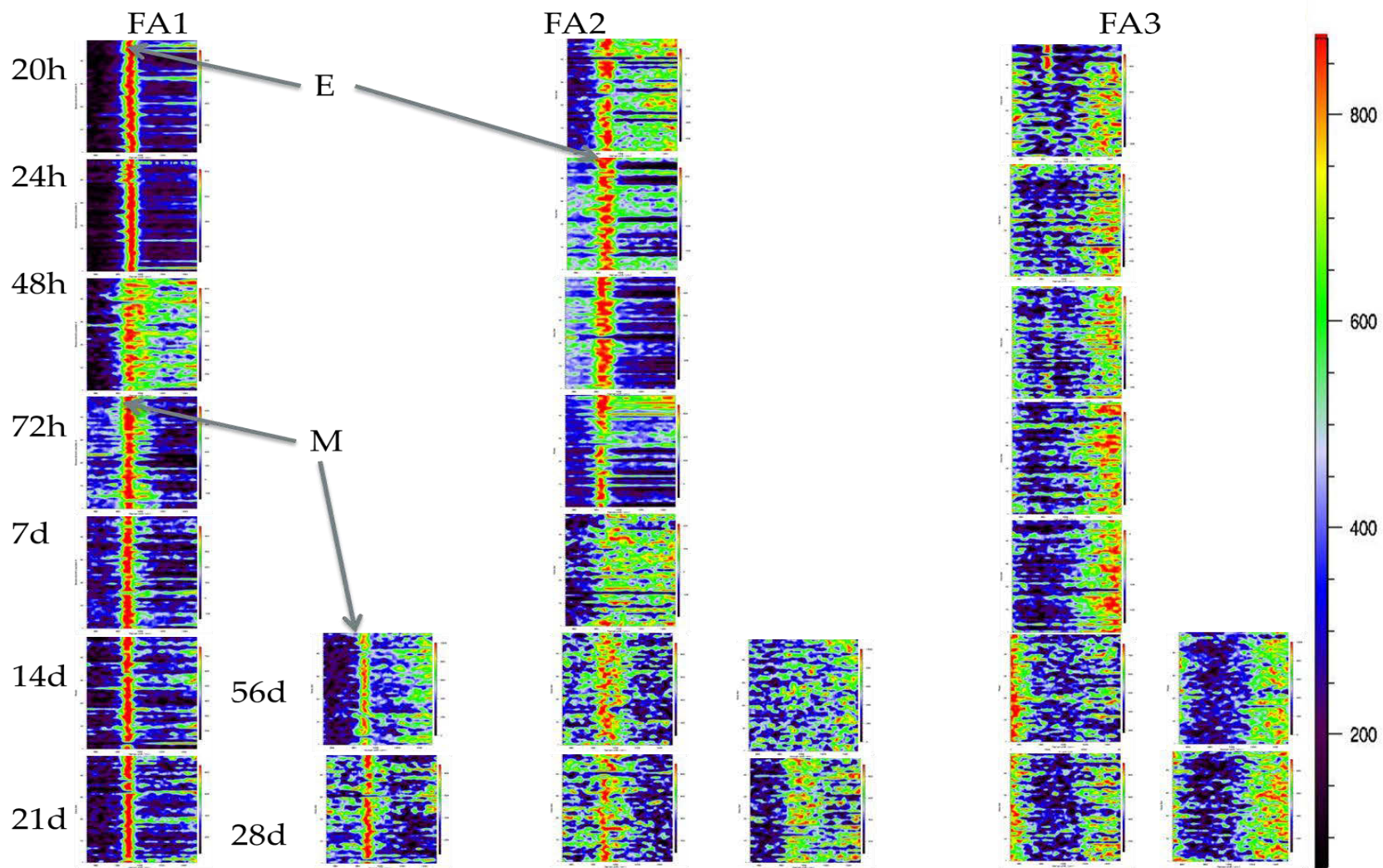


Figure 82: Images representing the evolution of sulfates in 50%FA+50%OPC pastes.

For FA3, the spectra obtained does not provide much information about the ongoing hydration process in this paste. For some reason there were no peaks obtained at any age (even after repeated testing on different samples). Looking at the image representing the growth of phases in this 950-1050 wavenumber region, there is slight evidence of formation of AFt type phase at 20 hours but beyond that the region is mostly covered with surrounding noise. But considering that there is 50% OPC present in the system, the hydration process must go on, even though it is not fully detected. There could be two reasons behind this phenomenon: a) That the products formed in this mix are highly amorphous and disordered in nature and not crystalline enough to be detected by Raman b) That this fly ash is merely acting as a filler in the mix and has no contribution to the pore solution chemistry, which is resulting in the coarse grains of the fly ash coating the top surface of the studied samples, resulting in little or no detection of the sulfo-aluminate phases hydrating beneath the surface.

Also, the results obtained from the evolution of hydroxides are equally strange, in which highly intense peaks for portlandite are found to be dominant in FA3. This also suggests that perhaps portlandite has crystallized strongly on the surface of FA3 samples inhibiting detection of any other phases.

4.4.2 Evolution of hydroxides

Figure 83 shows the calibration curve constructed for a pure CH sample. It is to be noted that the intensity varies exponentially with increasing concentration, hence a big difference in intensity doesn't reflect a big difference in concentration of a given species.

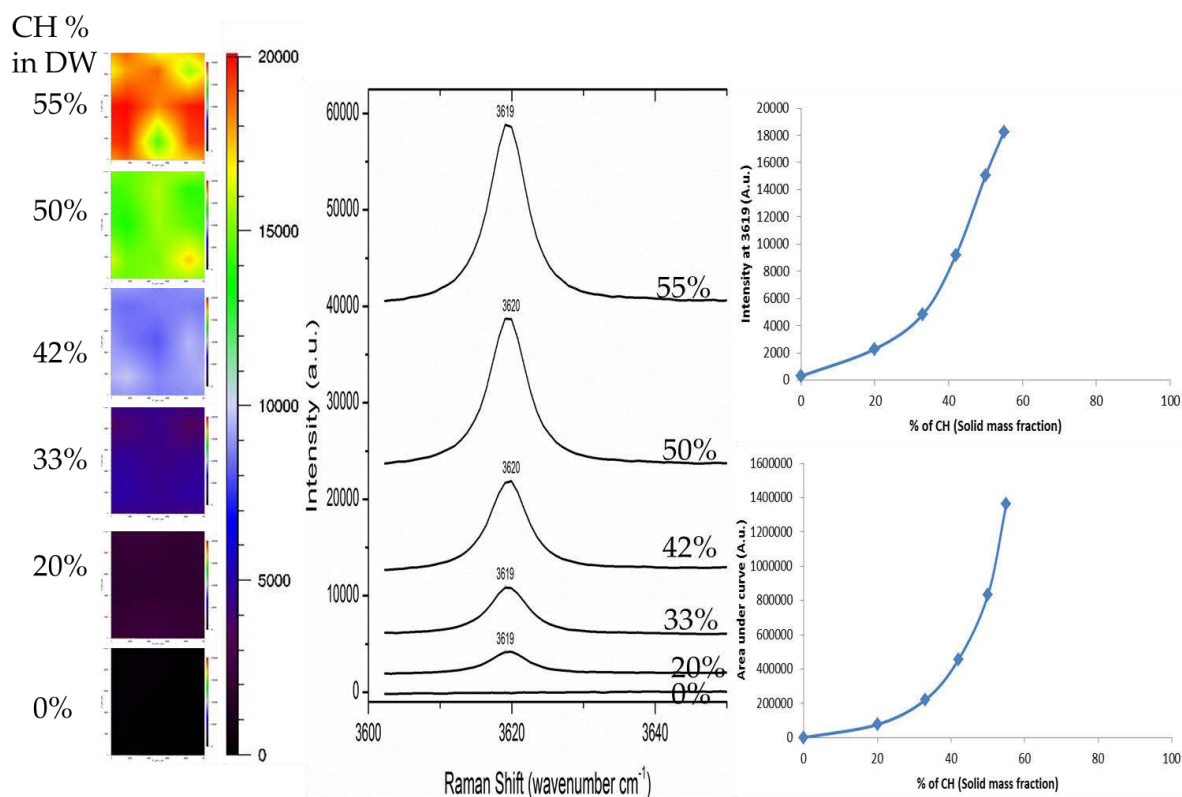


Figure 83: Calibration of Intensity with CH concentration

4.4.2.1 OPC

Figure 84 shows the evolution of calcium hydroxide (CH/portlandite) in the 100% OPC paste. The most intense peak of CH crystal was established at 3620 ± 5 by Padanayi [62] based on his theoretical calculations. Several authors (see Table 9) reported their observed peaks in the range suggested by Padanyi. This work, employing commercial clinkers and fly ashes, agreed well with the peaks observed in the past and a consistent peak at 3619 cm^{-1} was observed in all of the pastes. There were slight drifts in the peak position but not more than ± 1 as can be seen in the following figures. Since the data from evolution of hydroxides was not normalized, the intensities of these peaks at 3619 cm^{-1} were used to map the distribution of concentration of CH on a given surface of $3 \times 3 \text{ mm}^2$.

A consistent trend of growing CH was obtained in the OPC paste which shows the progress of reaction of the calcium silicates resulting in the production of calcium hydroxide as the by product – which is the long established, basic mechanism of cement hydration [81].

Figure 85 shows the mapped distribution of CH in the OPC paste. As expected, the CH concentration increases spatially as a function of time.

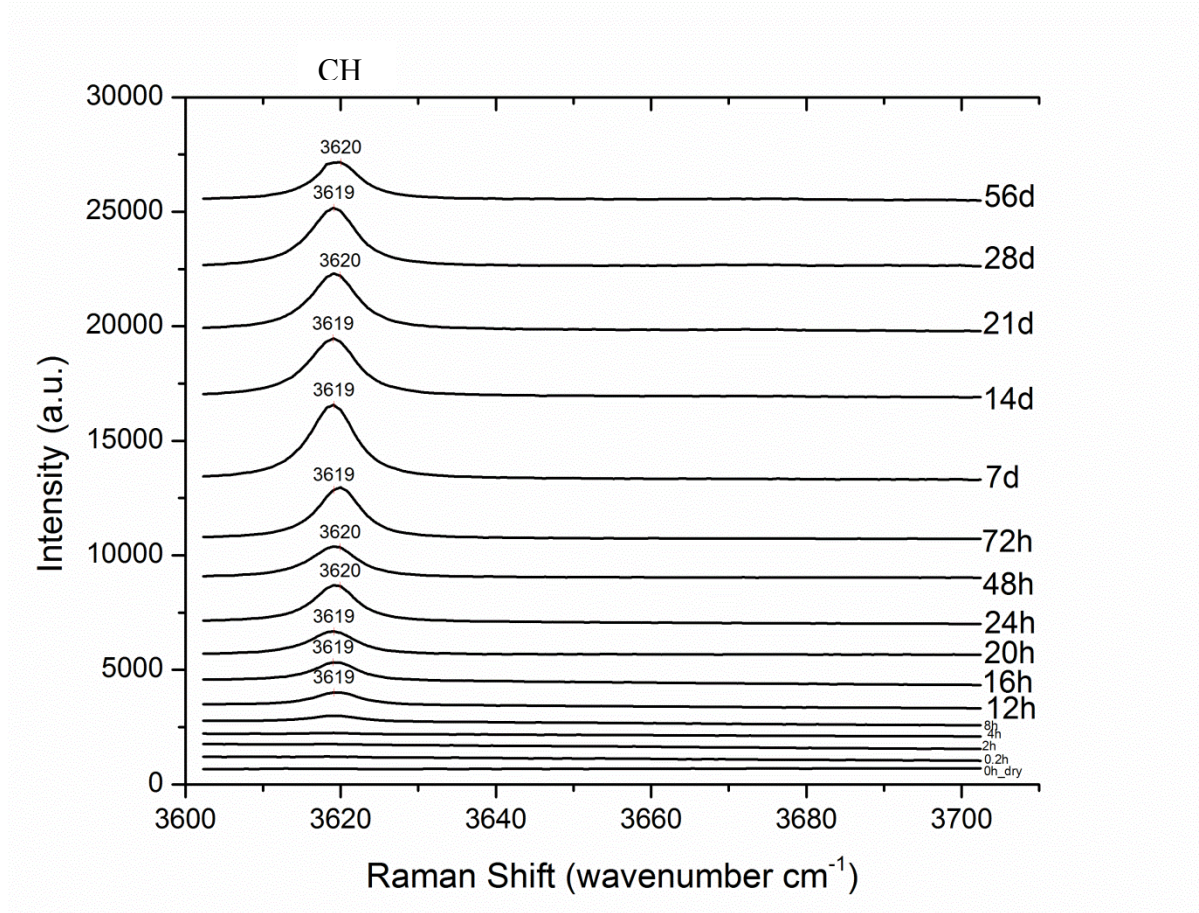


Figure 84: Evolution of hydroxides in 100%OPC paste.

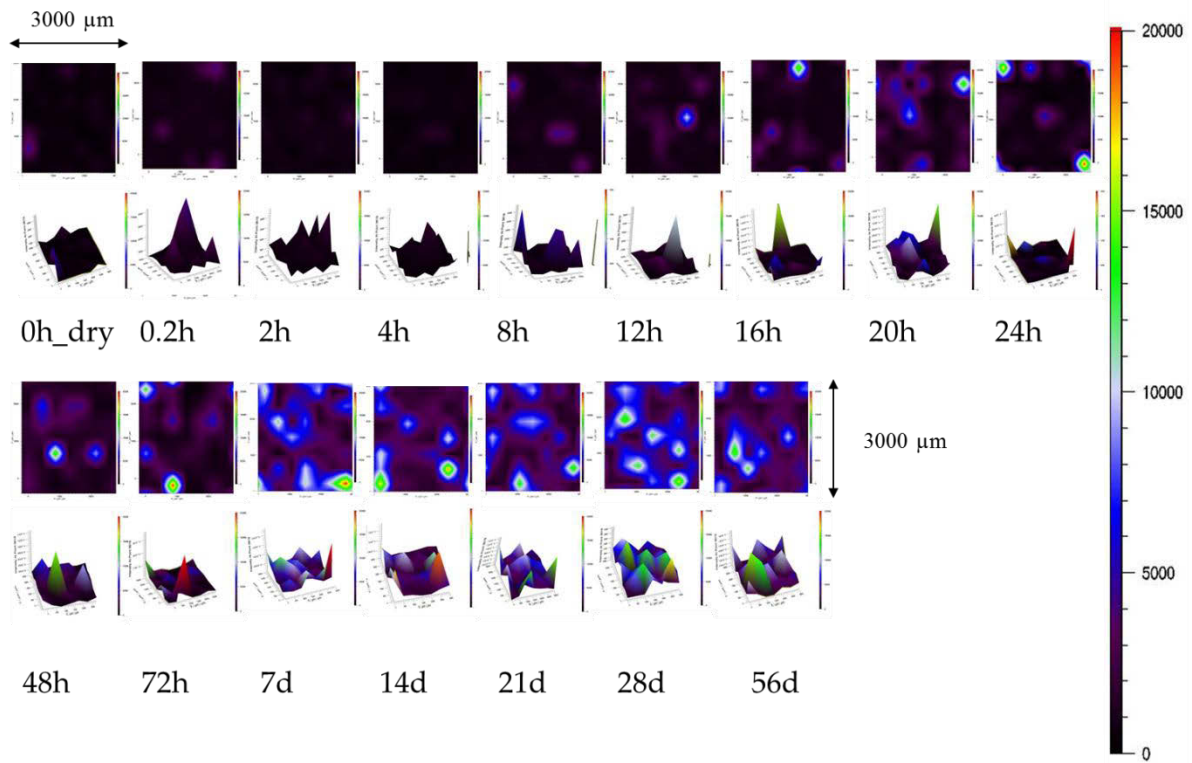


Figure 85: Mapping the distribution of CH in 100% OPC paste

4.4.2.2 Fly Ashes

Figure 86 shows the evolution of hydroxides in pastes modified by three different types of fly ashes and a comparison between the CH overall peak intensities is visible.

In the case of FA1, the CH begins to be detected as early as 4 hours indicating its' early nucleation is possibly due to high Ca^{2+} ion concentration in the mix. This agrees well with the AAS results shown earlier in Figure 38. The CH intensity and spatial distribution continues to grow up to 72 hours but the next measurement at 7 day shows a change in the expected growth behavior of CH. The CH intensity has now declined, suggesting that it has begun to be consumed by the reactive silicate/aluminate phases present in this fly ash while a secondary hydroxyl phase at 3675 cm^{-1} appears to originate. This can be a AFm type phase

based on the assignments by Renaudin et al. [69], Black et al. [63], and Frias and Ramirez [51] all of whom assigned the 3675 cm^{-1} mode to AFm.

However, Frias and Ramirez assigned a vibration at 3692 to C_2ASH_8 which suggests that this mode may also be due to calcium-alumino-silicate-hydrate type phase (which could also be belonging to the AFm family of phases). Due to high complexity of possible phases the assignment is hence tentative but overall suggests that in FA1, at later ages, CH is being consumed by the pozzolanic reaction and secondary hydration products are being formed.

In the case of FA2, a normal trend of growing CH akin to the OPC paste is observed. The CH intensities continue to grow up to about 7 days after which the growth has more or less stabilized. Moreover, the spatial distribution has also reached equilibrium where it is no more increasing in the given area studied.

The case of FA3 is the most extreme, and also perhaps appears maybe a bit exaggerated from reality. The concentration of CH in the given area is on an upward trend once the crystallization begins from 8-12 hours. At 28 days the concentration of CH is even higher than the 100% OPC paste, indicating a high amount of calcium hydroxide present in this mix.

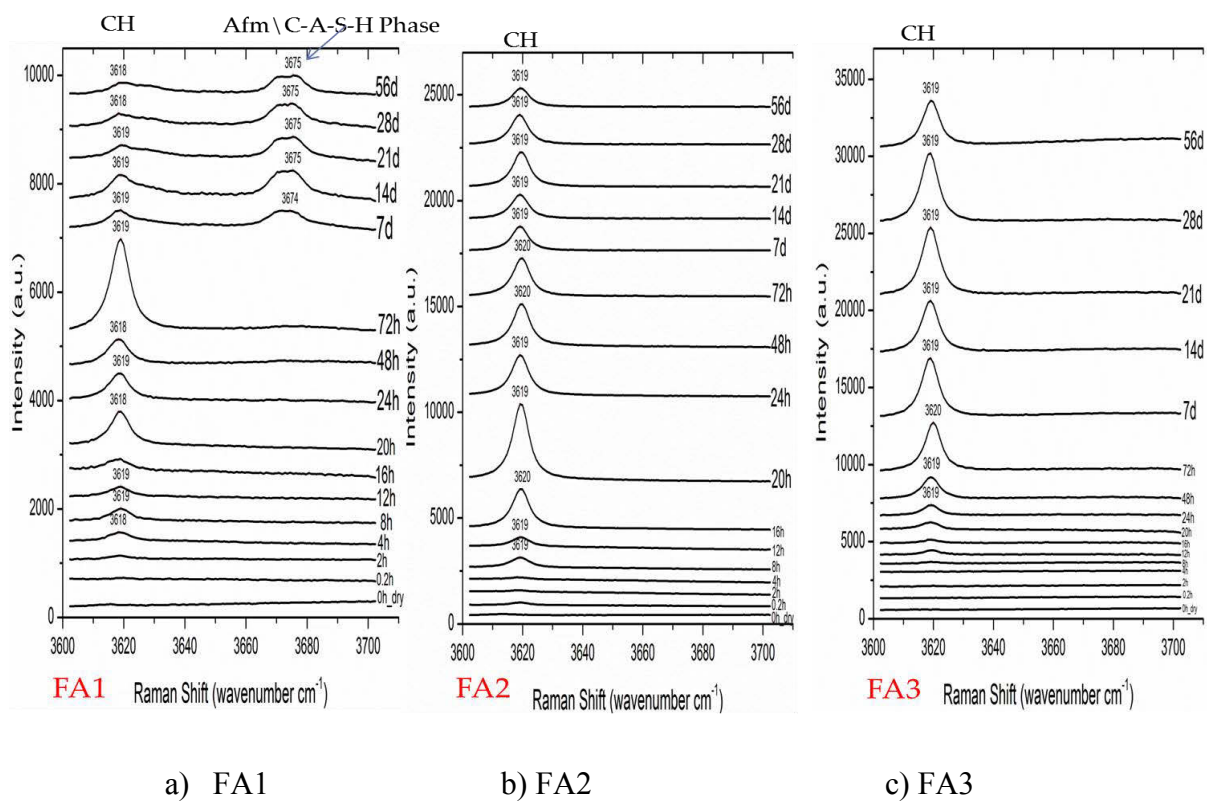


Figure 86: Evolution of hydroxides in 50%FA+50%OPC pastes.

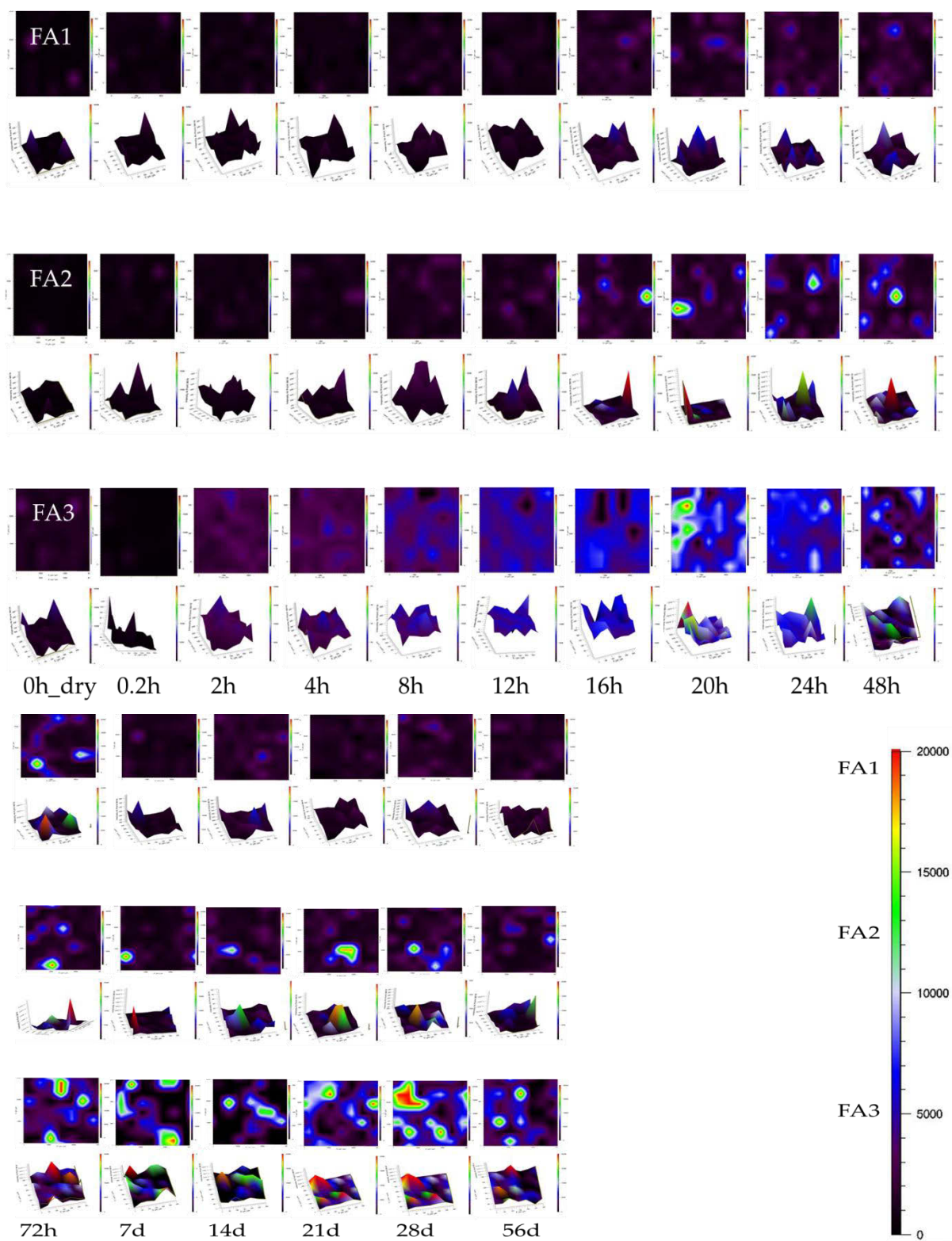


Figure 87: Mapping the distribution of CH in 50%FA+50%OPC pastes

Another reason to consider is the presence of the glassy phases in the fly ashes. Based on the dry Raman data, FA1 has a comparatively dominant hump near the 600 wavenumber region followed by FA2 and FA3. This suggests that FA1 has a reactive, amorphous glass phases which may also be enhancing its reactivity by consuming the portlandite to form calcium aluminate silicate hydrates or more C-S-H.

However this may not be the truth but the reason high intensities are being detected can be linked to several other causes. It may be possible that the crystals are nucleating on the inert particles of the FA3 which is merely serving as a filler and perhaps promoting nucleation by not interfering in the hydration reaction. Also the silicate and aluminate phases in this fly ash are not reactive and hence not contributing to any pozzolanic reaction which may reduce the concentration of CH in the mix. Another thing to consider is that the particle size of this fly ash is the coarsest among all fly ashes, there is more air voids in the system which is promoting the free growth of portlandite hexagonal crystals. During mix preparations it was found that there was plenty of bleed water on the surface of this particular fly ash (other finer mixes absorbed the water reducing the w/b ratio while this coarse mix had more bleeding). This bleed water on the top may have resulted in nucleation and dominance of CH crystals on the surface of the mix samples. This explains why the CH intensities are so strong in this mix and it also explains why no sulfate evolution is detected in this mix (because whatever sulfate evolution is going on is hidden under the surface of the CH crystalline layer).

Moreover, it must be remembered that every time at every curing age a new sample cup was analyzed which further supports that these results are not just due to a singular specimen but instead are representative of the entire parent population.

The initial objective of this study was to link the macro scale behavior of these fly ashes to the reactivity observed through Raman spectroscopy. While this has not been achieved completely, it can be said that the initial trend of reactivity in mixes in decreasing order $FA1 > FA2 > FA3$ matches somewhat well with trend of increasing CH content $FA1 < FA2 < FA3$. This is justified by the fact that the high presence of calcium hydroxide in the system induces more cleavage planes in the matrix which favors a fracture and hence lower strength. But again there are and maybe several more factors behind the behavior

which has been witnessed in this study and future work will involve in-depth study of the same.

CHAPTER 5: CONCLUSIONS, RECOMMENDATIONS AND FUTURE WORK

Based on the studies and experiments conducted in this Master's thesis work, following conclusions, recommendations, and ideas for future work are presented in the ensuing sections:

5.1 Conclusions

- 1) Raman spectroscopy serves as an effective tool for fingerprinting a variety of inorganic cementitious materials employed currently in the construction industry. However, due to variations in instrumental configurations across various research institutions as well as the variation in compositional chemistry of such materials, standard and verified libraries need to be established before a quantitative phase analysis (like Rietveld XRD) can be accurately performed.
- 2) Raman spectroscopy served effective in characterizing the dry binders and qualitative determination of commonly found phases in cements and fly ashes was possible. While the phase determination was not as detailed as provided by XRD, the results agreed well with the XRD and other supplementary data.
- 3) Raman spectroscopy was also successful in following the hydration process of complex, commercial, and extremely heterogeneous mixes containing ordinary Portland cement replaced by fly ashes of varying reactivities. In particular the focused studies on evolution of sulfates and hydroxides were able to provide some meaningful results.
- 4) Disappearance of Gypsum and formation of Ettringite as a function of time in young pastes was clearly recorded by Raman spectroscopy. FA1 containing highest amount of sulfates resulted in dominance of the AFt phase for a longer duration as compared to mixes with lower amount of sulfate type phases. The first 24 hours of hydration process followed by Raman microprobe matched well with the calorimetric data obtained separately. The conversion of Aft to Afm type phase was not very obvious

- and needs further research. It is possible that such a conversion may be very hard to observe in real, multi-phase samples (as opposed to synthetic or Aluminate pastes).
- 5) In case of evolution of hydroxides, Raman's unique ability to map the concentration of portlandite in an representative surface area of 9 mm^2 was found powerful in recording its evolution and distribution as a function of time. The reactivities of various mixes were correlated with the amount of CH formed in the system. Due to varying particle size, the effective w/b ratio changed in the systems and FA3 mix had bleeding on the surface of all the samples which could have promoted the growth of excessive CH crystals on the surface. While a direct correlation may be a matter of dispute, several observations were made based on the results.
 - 6) On its comparison with other techniques, Raman was found to be completely non-destructive and it requires virtually no sample preparation. Moreover the analysis times were quick and an area of 9 mm^2 with ~ 50 different locations can be mapped within 20 minutes. Also, while modern Raman microprobes are costlier than IR instruments, they are less expensive than standard XRD devices. Lastly, the unique mapping capabilities offered by this spectroscopy sets it apart from NMR in the sense that while NMR can only probe the local structure around a specific nuclei, Raman can provide the characteristic information at the bulk level.

5.2 Recommendations

- 1) In terms of configuration and instrument parameters, it is recommended that high frequency, low wavelength lasers should be employed as this study found application of 488 nm useful to study of cements and fly ashes and good S/N were obtained. A low magnification is desirable if an analysis spot of larger area is required (for heterogeneous materials). A 100% incident power of 25 mW was found to provide good S/N; lowering the incident power percentage is not recommended as it reduced the S/N greatly and resulted in omission of weak bands. Also, 25 mW seems not to

cause any physical damage to these samples other than temporary drying of the bleed water on the surface of fresh, very early age cement pastes. Mapping an area of not less than $3000 \times 3000 \mu\text{m}$ (9 mm^2) with at least 50 or more spatially distributed points is recommended if representative measurements are to be recorded. Overall analysis time should not increase more than 20 minutes for a hydrating sample as carbonation occurs readily once that timeframe ends.

- 2) Sample preparation and storage should ensure that the pastes are not attacked by carbonation or contaminated by the sealing films (if attached to the surface). Number of accumulations can be reduced and number of locations studied can be increased to obtain representative spectra.
- 3) Live, in-situ analysis of commercial clinkers using several experimental setups should be pursued with caution as often the results obtained might not be truly representative of the hydration reaction going on inside a real system. Several problems like the wall effect, contamination due to thin film sealing, decreasing S/N when passing laser through transparent mediums, interfering peaks were experienced by the author during this study in an attempt to try several methods used by previous researchers studying synthetic, pure samples. Finally, it was decided to use different samples of the same mix set at each age which were discarded after the measurement, and a new sample cup was opened fresh for the next age. This method induced additional randomness in the analysis which was both good and bad for this study. Bad in the sense of increasing non linearity of results and good in the sense of higher representativeness and higher reproducibility.
- 4) Again, more literature and a set of standards need to be established if quantitative phase analysis has to advance in the field of Raman application on such systems.
- 5) It is crucial that the interpretation of the results is done with caution. While, by no doubt, Raman is a powerful technique for qualitative purposes and for fingerprinting a variety of materials, Raman's application as a quantitative tool in commercial, cementitious systems needs further detailed research. It must be remembered that Raman scattered intensity is not just a function of the concentration of the analyte but

also depends on the polarizability of the active mode as well as the size of the scattering molecule or the particle itself.

5.3 Future work

Some of the future work that maybe followed in this field is recommended below:

- The instrument employed for study should first be used to test on synthetic standards to verify the standard peak locations observed for various phases. This can be very helpful in peak assignment in complex mixtures and can add more accuracy to the analysis part.
- Calibration curves for concentration are also recommended if a fully quantitative analysis is to be performed.
- Parallel studies with XRD or Reitveld XRD, thermogravimetry are highly recommended for future work in order to verify and establish the results obtained from Raman spectroscopy.
- If possible, future researchers are recommended to employ recent Raman instruments often combined with SEM, AFM or at least a high resolution microscope to gain better understanding of ongoing hydration processes.
- Extreme care should be taken while sample preparation. Even though consistent w/b of 0.45 was chosen for all the mixes, the fresh state and the subsequent bleeding brought an unwanted variation in the testing.

5.4 Final words

Overall, this study showed the scope of Raman spectroscopy in the field of real, commercial cementitious systems. “How wide is the scope?” is dependent on a researcher’s expectations from this analytical tool. As stated earlier, in the author’s opinion, qualitative analysis has plenty of possibilities and as more literature becomes available in the next few years, the

applicability and potential of Raman spectroscopy in detailed phase analysis and comparison of commercial clinkers and supplementary cementitious materials will improve. The quantitative analysis is likely to remain difficult unless several obstacles faced in this study are overcome. That being said, Raman is still an effective characterization tool for cement science and hopefully will continue to grow as an aid to the relevant scientific community. But it will be very unlikely that it will become a standalone technique to provide all the answers that we seek when characterizing cementitious materials. This is so, because, to fully understand the cement-fly ash hydration process, a variety of techniques need to be at one's disposal, leading to an accurate, precise and confident characterization.

To sum it all, a sentence from Richardson et al. [27] lays down the essence of the author's message as follows, "...no single technique is a panacea and multi-instrument approaches will be necessary."

References

1. Foundation, A.C.A.A.E. *Production and Use Statistics '07*. 2007.
2. *Coal Statistics*. World Coal Institute December, 2011.
3. William Watson, et al., *U.S. Coal Supply and Demand: 2010 Year in Review*, U.S.E.I. Administration, Editor. 2011.
4. Edwards, P. and McCaffrey, in R. *Global Cement Directory 2010*: Epsom, UK.
5. Scrivener, K. *Introduction: basic concepts. 1st training course*. in *NANOCEM RTN*. 2006. Aalborg, Denmark.
6. Ahmaruzzaman, M., *A review on the utilization of fly ash*. Progress in Energy and Combustion Science, 2010. **36**(3): p. 327-363.
7. Siddique, R., *Performance characteristics of high-volume Class F fly ash concrete*. . Cement and Concrete Research, 2004. **34**(3): p. 487-493.
8. Thomas, M.D.A., et al., *Use of ternary cementitious systems containing silica fume and fly ash in concrete*. Cement and Concrete Research, 1999. **29**(8): p. 1207-1214.
9. *What are Coal Combustion By-Products (CCBs)?* 2007
10. Hemmings, R.T., and Berry, E. E., *On the Glass in Coal Fly Ashes: Recent Advances*. Materials Research Society Symposium Proceedings, 1988. **113**: p. 3-38.
11. Siddique, R., *Performance characteristics of high-volume Class F fly ash concrete*. Cement and Concrete Research, 2004. **34**(3): p. 487-493.
12. Collepardi, M., Baldini, G., Pauri, M. , *The effect of pozzolans on the tricalcium aluminate hydration*. Cement and Concrete Research, 1978. **8**(6): p. 741-751.
13. Ogawa K, U.H., Takemoto K., *The mechanism of the hydration in the system C3S-pozzolan*. . Cement and Concrete Research, 1980. **10**(5): p. 683-96.
14. Materials, A.S.f.T.a., *Standard Test Methods for Sampling and Testing Fly Ash or Natural Pozzolans for Use as a Mineral Admixture in Portland-Cement Concrete (ASTM C 311)*, in *American Society for Testing and Materials*. 1998: United States.
15. Ranganath RV, S.R., Krishnamoorthy S. *Influence of fineness and soluble silica content of fly ash on their strength development with respect to age*. in *Proceedings of the fifth international conference on fly ash, silica fume, slag, and natural pozzolans in concrete*. 1995.
16. Monzo J, P.J., Peris-Mora E., *A preliminary study of fly ash granulometric influence on mortar strength*. . Cement and Concrete Research, 1994. **24**(4): p. 791-796.
17. Tangpagasit, J., Cheerarot, R., Jaturapitakkul, C., Kiattikomol, K. , *Packing effect and pozzolanic reaction of fly ash in mortar*. Cement and Concrete Research, 2005. **35**(6): p. 1145-1151.
18. Mora, E.P., Paya, J., Monzo, J. , *Influence of different sized fractions of a fly ash on workability of mortars*. Cement and Concrete Research, 1993. **23**(4): p. 917-924.
19. Kiattikomol, K., Jaturapitakkul, C., Songpiriyakij, S., Chutubtim, S. , *A study of ground coarse fly ashes with different finenesses from various sources as pozzolanic materials*. . Cement and Concrete Composites, 2001. **23**(4-5): p. 335-343.
20. Yamamoto, T., et al., *Pozzolanic reactivity of fly ash – API method and K-value*. Fuel, 2006. **85**(16): p. 2345-2351.

21. Paya J, M.J., Peris-Mora E, Borrachero MV, Tercero R, Pinillos C. , *Early-strength development of Portland cement mortars containing air classified fly ash*. Cement and Concrete Research, 1995. **25**(2): p. 449-456.
22. Hubbard FH, D.R., Ellis MS., *Pulverized-fuel ash for concrete compositional characterization of United Kingdom PFA*. Cement and Concrete Research, 1985. **15**(1): p. 185-198.
23. Ramezaniapour A, C.J., *The measurement of lime reactivity of natural and artificial pozzolans*. . Second Int Sem Cem Build Mater, 1989. **4**: p. 81-88.
24. Suppachai Sinthaworn, P.N., Vol. 29, 2009, pp. 1526–1531. , *Quick monitoring of pozzolanic reactivity of waste ashes*. . Waste Management, 2009. **29**: p. 1526-1531.
25. Lea, F.M., *The Chemistry of Cement and Concrete 3rd ed*. 1971, New York,: Chemical Publishing Co.
26. Neville, A.M., *Properties of Concrete, 2nd ed*. 1975, London: Pitman Publishing.
27. Nelson, E.B., *Well Cementing*. 1990, Houston, TX: Schlumberger Educational Services.
28. Taylor, H.F.W., *Cement chemistry*. 1990, London; San Diego: Academic Press.
29. Bentz, D.P., *CEMHYD3D: A Three-Dimensional Cement Hydration and Microstructure Development Modelling Package* 2000
30. Ingle, J.D. and S.R. Crouch, *Spectrochemical analysis*. 1988: Prentice Hall.
31. Dennis, A. *What is Raman Spectroscopy*. [cited 2012.
32. Min-Liang, W., *Polarizability and tensor ellipsoid in the Raman effect*. Vibrational Spectroscopy, 1994. **7**(2): p. 197-199.
33. Cotton, F.A., *Chemical applications of group theory*. 1963: Interscience Publishers.
34. Bensted, J., *Uses of Raman Spectroscopy in Cement Chemistry* Journal of the American Ceramic Society, 1976. **59**(3-4): p. 140-143.
35. Bensted, J., Rev. Mater. Constr., 1976. **73**(6).
36. Bensted, J., *Raman spectral studies of carbonation phenomena*. Cement and Concrete Research, 1977. **7**: p. 161-164.
37. Bensted, J., *A discussion of the paper "Some possibilities of Raman microprobe in cement chemistry" by M. Conjeaud and H. Boyer* Cement and Concrete Research, 1980. **10**: p. 715-716.
38. Conjeaud, M. and H. Boyer, *Some possibilities of Raman microprobe in Cement chemistry*. Cement and Concrete Research, 1980. **10**: p. 61-70.
39. Chris D. Dyer, P.J.H., *The Raman spectroscopy of cement minerals under 1064 nm excitation*. Spectrochimica Acta, 1993. **49A**(5-6): p. 715-722.
40. D. Bonen, T.J.J., S. L. Sarkar, *Characterization of principal clinker minerals by FT-Raman microspectroscopy*. Cement and Concrete Research, 1994. **24**(5): p. 959-965.
41. M. Tarrida, M.M., B. Le Rolland, P. Colombet, *An in-situ Raman spectroscopy study of the hydration of tricalcium silicate*. Advanced Cement Based Materials, 1995. **2**: p. 15-20.
42. Black, L., P. Purnell, and J. Hill, *Current themes in cement research*. Advances in Applied Ceramics, 2010. **1019**(5).
43. Richardson, I.G., et al., *Characterisation of cement hydrate phases by TEM, NMR and Raman spectroscopy*. Advances in Cement Research, 2010. **22**(4): p. 233-248.

44. Martinez-Ramirez, S. and L. Fernandez-Carrasco, *Raman Spectroscopy: Application to Cementitious Systems*, in *Construction and Building: Design, Materials, and Techniques*, S.G. Doyle, Editor. 2011, Nova Science Publishers.
45. Deng, C.S., et al., *Ageing of oilfield cement at high humidity: a combined FEG-ESEM and Raman microscopic investigation*. Journal of Materials Chemistry, 2002. **12**(10).
46. Newman, S.P., et al., *Anomalous fluorescence in near-infrared Raman spectroscopy of cementitious materials*. Cement and Concrete Research, 2005. **35**(8): p. 1620-1628.
47. Martinez-Ramirez, S., M. Frías, and C. Domingo, *Micro-Raman spectroscopy in white portland cement hydration: long-term study at room temperature*. Journal of Raman Spectroscopy, 2006. **37**(5): p. 555-561.
48. Martinez-Ramirez, S., et al., *Evolution of ordinary Portland cement hydration with admixtures by spectroscopic techniques*. Advances in Cement Research, 2006. **18**(3): p. 111-117.
49. Ibáñez, J., et al., *Hydration and carbonation of monoclinic C_2S and C_3S studied by Raman spectroscopy*. Journal of Raman Spectroscopy, 2007. **38**(1): p. 61-67.
50. Black, L., et al., *Structural Features of C-S-H(I) and Its Carbonation in Air: A Raman Spectroscopic Study. Part II: Carbonated Phases*. Journal of the American Ceramic Society, 2007. **90**(3): p. 908-917.
51. Frias, M. and S. Martinez-Ramirez, *Use of micro-Raman spectroscopy to study reaction kinetics in blended white cement pastes containing metakaolin*. Journal of Raman Spectroscopy, 2009. **40**: p. 2063-2068.
52. Chollet, M. and M. Horgnies, *Analyses of the surfaces of concrete by Raman and FT-IR spectroscopies: comparative study of hardened samples after demoulding and after organic post-treatment*. Surface and Interface Analysis, 2011. **43**(3): p. 714-725.
53. Remy, C., B. Reynard, and M. Madon, *Raman Spectroscopic Investigations of Dicalcium Silicate: Polymorphs and High-Temperature Phase Transformations*. Journal of the American Ceramic Society, 1997. **80**(2): p. 413-423.
54. Gastaldi, D., et al., *The use of Raman spectroscopy as a versatile characterization tool for calcium sulphoaluminate cements: a compositional and hydration study*. Journal of Materials Science, 2007. **42**(20): p. 8426-8432.
55. Black, L., et al., *In situ Raman analysis of hydrating C_3A and C_4AF pastes in presence and absence of sulphate*. Advances in Applied Ceramics, 2006. **105**(4): p. 209-216.
56. Potgietervermaak, S., et al., *The application of Raman spectrometry to the investigation of cement Part II: A micro-Raman study of OPC, slag and fly ash*. Cement and Concrete Research, 2006. **36**(4): p. 663-670.
57. Gastaldi, D., E. Boccaleri, and F. Canonico, *In situ Raman study of mineral phases formed as by-products in a rotary kiln for clinker production*. Journal of Raman Spectroscopy, 2008. **39**(7): p. 806-812.
58. Black, L., *Raman Spectroscopy for the Analysis of Cements - Past, Present and Future*.
59. R. James Kirkpatrick, J.L.Y., Paul F. McMillan, Ping Yu, Xiandong Cong, *Raman spectroscopy of C-S-H, Tobermorite, and Jennite*. Advanced Cement Based Materials, 1997. **5**: p. 93-99.

60. Black, L. and C. Breen. *Characterization of Fresh and Aged Nanocrystalline C-S-H Phases by Raman Spectroscopy*. in *24th Cement and Concrete Science*. 2004. Coventry.
61. Garbev, K., et al., *Structural Features of C-S-H(I) and Its Carbonation in Air- A Raman Spectroscopic Study. Part I: Fresh Phases*. Journal of the American Ceramic Society, 2007. **90**(3): p. 900-907.
62. Padanyi, Z.V., *The Raman Spectrum of Ca(OH)₂*. Solid State Communications, 1970. **8**: p. 541-543.
63. Black, L., et al., *Hydration of tricalcium aluminate (C₃A) in the presence and absence of gypsum—studied by Raman spectroscopy and X-ray diffraction*. Journal of Materials Chemistry, 2006. **16**(13): p. 1263.
64. Renaudin, G., et al., *A Raman Study of the Sulfated Cement Hydrates: Ettringite and Monosulfoaluminate*. Journal of Advanced Concrete Technology, 2007. **5**(3).
65. Bensted, J., *Cement and Concrete Research*, 1978. **8**.
66. Hua Chang, P.J.H., S.C. Hou, *Application of thermo-Raman spectroscopy to study dehydration of CaSO₄·2H₂O and CaSO₄·0.5H₂O*. Materials Chemistry and Physics, 1999. **58**: p. 12-19.
67. Prasad, P.S.R., A. Pradhan, and T.N. Gowd, *Current Science*, 2001. **80**(9).
68. Sahu, S., D.L. Exline, and M.P. Nelson, *Identification of thaumasite in concrete by Raman chemical imaging*. Cement and Concrete Composites, 2002. **24**(3–4): p. 347-350.
69. Renaudin, G., et al., *A Raman study of the Sulfated Cement Hydrates: Ettringite and Monosulfoaluminate*. Journal of Advanced Concrete Technology, 2007. **5**(3): p. 299-312.
70. Livingston, R.A., et al., *Raman scattering and X-ray diffraction study of the thermal decomposition of an ettringite-group crystal*. Physics and Chemistry of Minerals, 2003. **30**(1): p. 31-38.
71. Brough, A.R. and A. Atkinson, *Micro-Raman spectroscopy of thaumasite*. Cement and Concrete Research, 2001. **31**(3): p. 421-424.
72. Jallada, K.N., et al., *Chemical mapping of thaumasite formed in sulfate-attacked cement mortar using near-infrared Raman imaging microscopy*. Cement and Concrete Research, 2001. **31**(6): p. 953-958.
73. Martinez-Ramirez, S., et al., *Micro-Raman spectroscopy applied to depth profiles of carbonates formed in lime mortar*. Cement and Concrete Research, 2003. **33**(12): p. 2063-2068.
74. Tlili, M.M., et al., *Characterization of CaCO₃ hydrates by micro-Raman spectroscopy*. Journal of Raman Spectroscopy, 2002. **33**(1): p. 10-16.
75. Gabrielli, C., et al., *In situ Raman spectroscopy applied to electrochemical scaling. Determination of the structure of vaterite*. Journal of Raman Spectroscopy, 2000. **31**(6): p. 497-501.
76. Vangrieken, R. and C. Xhoffer, *Microanalysis of individual environmental particles*. Journal of Analytical Atomic Spectrometry, 1992. **7**(2): p. 81-88.
77. Scheetz, B.E. and W.B. White, *Characterization of crystalline phases in fly ash by microfocus Raman spectroscopy*. Proceedings of MRS conference on: Fly Ash and Coal Conversion By-Products Characterization, Utilization and Disposal I, 1985. **43**.

- 78. Guedes, A., et al., *Characterization of fly ash from a power plant and surroundings by micro-Raman spectroscopy*. International Journal of Coal Geology, 2008. **73**(3-4): p. 359-370.
- 79. Marshall, C.P. and A.O. Marshall, *Hematite and carbonaceous materials in geological samples: A cautionary tale*. Spectrochimica Acta Part A: Molecular and Biomolecular Spectroscopy, 2011. **80**(1): p. 133-137.
- 80. Taylor, H.F.W., *Cement chemistry*. 1997: T. Telford.
- 81. Bullard, J.W., et al., *Mechanisms of cement hydration*. Cement and Concrete Research, 2011. **41**(12): p. 1208-1223.

VITA

NAME OF AUTHOR: Nishant Garg

DATE AND PLACE OF BIRTH: March 28, 1989, Chandigarh, Punjab, India

DEGREES AWARDED:

Diploma in Civil Engineering, Chandigarh College of Engr. & Technology, 2007

B. E. in Civil Engineering, Thapar University, 2010

M. S. in Civil Engineering, Iowa State University, 2012

HONORS AND AWARDS:

David Dwight Eisenhower Fellowship, 2011

PROFESSIONAL EXPERIENCE:

Research Assistant, CCEE, Iowa State University, 2010-12

Teaching Assistant, CCEE, Iowa State University, 2011-12